

# Molecular hydrogen tweezers: Structure and mechanisms by neutron diffraction, NMR, and deuterium labeling studies in solid, and solution

Felix Schulz,<sup>a</sup> Victor Sumerin,<sup>b</sup> Sami Heikkinen,<sup>b</sup> Björn Pedersen,<sup>c</sup> Cong Wang,<sup>b</sup> Michiko Atsumi,<sup>d</sup> Markku Leskelä,<sup>b</sup> Timo Repo,<sup>b</sup> Pekka Pyykkö,<sup>b</sup> Winfried Petry<sup>c</sup> and Bernhard Rieger<sup>\*,a</sup>

<sup>a</sup> WACKER-Lehrstuhl für Makromolekulare Chemie, Technische Universität München, Germany

<sup>b</sup> Department of Chemistry, University of Helsinki, Finland

<sup>c</sup> Forschungs-Neutronenquelle Heinz Maier-Leibnitz (FRM II), Technische Universität München, Germany

<sup>d</sup> Department of Physical and Analytical Chemistry, Uppsala University, Sweden

## SUPPLEMENTARY INFORMATION

### Contents

Discussion of line broadening of the NH signal in NHHB in <sup>1</sup> H NMR spectra	S3
<sup>1</sup> H, <sup>2</sup> H, <sup>11</sup> B, <sup>13</sup> C and <sup>19</sup> F NMR spectra	S5
IR spectra	S15
HRESI-TOF mass spectra	S25
<sup>1</sup> H-T <sub>1</sub> relaxation measurement data	S26
Selective 1D NOE and 2D NOESY data for r <sub>H1-H8</sub> determination	S30
Neutron diffraction data	S33
TG-MS measurements	S39
Selected Zero-Point Energies (ZPEs) from CAM-B3LYP/6-31G** level calculations	S44
2D H,H NOESY NMR spectra	S45

<b>VT-NMR spectra</b>	<b>S51</b>
<b>Complete reference 71</b>	<b>S53</b>
<b>References</b>	<b>S53</b>

## Discussion of line broadening of the NH signal in NHHB in $^1\text{H}$ NMR spectra (see Figures S1-S4)

The fact that a  $^3J_{\text{HH}}$  coupling between NH and benzylic  $\text{CH}_2$  of NHHB is observable in the signal at 4.45 ppm (doublet) in the  $^1\text{H}$  NMR spectrum in  $\text{CD}_2\text{Cl}_2$  (see Figure S3), but is absent in the broad NH-signal, gives direct evidence that the large width of the ammonium proton signal can not originate from rapid proton exchange. Proton exchange giving rise to a line width of 165 Hz would translate into a proton lifetime in a particular position of a few milliseconds.<sup>1</sup> This high exchange rate would wash out the coupling interaction, and the benzylic proton signal would appear as a singlet. Therefore, the origin for a broad line is not exclusively proton exchange. Obviously, this still leaves room for such a slow exchange that allows coupling to be detected.

Dilution experiments were performed where the line widths of the NH peak were monitored at different NHHB concentrations in  $\text{CD}_2\text{Cl}_2$ . The results are presented in Figure S1a-c: All signals exhibit the same line width of approximately 165 Hz. The fact that the line width is independent of the concentration of NHHB shows that the effect of intermolecular proton exchange between two molecules of NHHB on the ammonium proton line width is negligible i.e. the exchange is slow. Otherwise the line width would decrease with lower concentrations of NHHB. Intermolecular exchange with residual water in the solvent was minimized by careful drying and handling of the solvent.

Possible mechanisms responsible for a broad ammonium proton line width, that still allow coupling (averaged) to be detected in the  $\text{CH}_2$  signal, include the existence of a dynamic equilibrium of conformational isomers and/or a dynamic equilibrium within the dihydrogen bond as depicted in Schemes 1 and 2 in the main article. They can both lead to different chemical shifts of the NH proton, which then appears as one coalesced, broad line due to an intermediate exchange rate at room temperature (RT).

Another mechanism, that preserves the doublet structure in the  $\text{CH}_2$ -resonance, due to the coupling between amino and benzylic protons, and still can result in extensively broadened NH-resonance, is the quadrupolar relaxation of  $^{14}\text{N}$  (spin = 1). That, depending on the relaxation rate, decouples  $^1J_{\text{NH}}$  wholly or partially. As an effect of this self-decoupling, the “expected” 1:1:1 triplet in the  $^1\text{H}$  spectrum due to the  $^1\text{H}$ - $^{14}\text{N}$  coupling appears as a single broad line (which is usually the case in organic molecules).<sup>1a</sup> Reduced rotational averaging makes the intramolecular electronic environment of  $^{14}\text{N}$  less symmetric. This will enhance self-decoupling via quadrupolar relaxation leading to further narrowing of the NH resonance line. An NMR measurement at low temperatures, or the use of a viscous solvent, slow down molecular motions, i.e. increase the molecular correlation time, and can thus be used to enhance the aforementioned effect.<sup>1a,2,3</sup>

Measurements in  $\text{DMSO-d}_6$  as well as VT experiments were used to evaluate the above mentioned mechanisms (Figures S1 and S2). The spectrum in  $\text{DMSO-d}_6$  showed a single NH resonance with a line width of only  $\Delta\nu_{1/2} = 12$  Hz (Figures S1d and S4) and the coupling to the benzylic  $\text{CH}_2$  group could still be observed in the doublet of  $\text{CH}_2$  ( $^3J_{\text{HH}} = 3.3$  Hz). In addition, no new NH signals corresponding to different NH chemical shifts of separate tautomers/conformers were observed at lower temperatures. Hence the conformational exchange between NHHB(1) and NHHB(2) can be ruled out as the major contributor to peak broadening. Most certainly strong hydrogen bonding with  $\text{DMSO-d}_6$  would have slowed down the reaction rates  $k_1$  and  $k_2$  for the different NH chemical shifts to be resolved. Instead, the relatively narrow line width in  $\text{DMSO-d}_6$  arises from enhanced  $^{14}\text{N}$  quadrupolar relaxation originating from slower rotations hindered in the more viscous  $\text{DMSO-d}_6$ . This leads to a more complete self-decoupling of  $^1J_{\text{NH}}$  and consequently a narrower line width. A similar behavior was also observed at low temperatures, where the NH line width decreased with decreasing temperature.

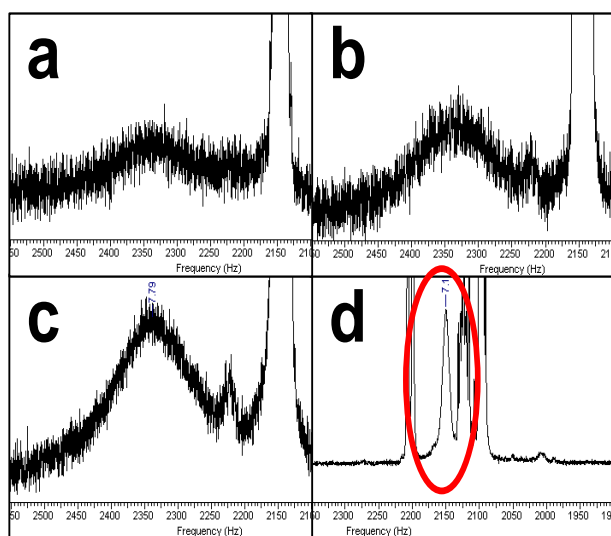


**Figure S1.** NH signal in  $^1\text{H}$  NMR spectra of NHHB recorded at RT with 128 scans each.<sup>4</sup> (a)  $c(\text{NHHB}) = 0.025$  mol/L in  $\text{CD}_2\text{Cl}_2$ ; (b)  $c(\text{NHHB}) = 0.050$  mol/L in  $\text{CD}_2\text{Cl}_2$ ; (c)  $c(\text{NHHB}) = 0.100$  mol/L in  $\text{CD}_2\text{Cl}_2$ ; (d)  $c(\text{NHHB}) = 0.100$  mol/L in  $\text{DMSO-d}_6$ , zoomed out to show the whole NH peak at 7.16 ppm.

To gain deeper insight into the *ansa*-ammonium-borate system, VT NMR studies of **NHHB** in  $\text{CD}_2\text{Cl}_2$  were performed in the range 213 – 293 K. Figure S2a clearly shows that the line width of the *NH* signal is decreasing at lower temperatures down to a value of  $\Delta\nu_{1/2} = 19$  Hz, indicating an increase of the  $^{14}\text{N}$  quadrupolar relaxation rate, leading to efficient elimination of residual  $^1J_{\text{NH}}$  as mentioned before. At low temperatures the signal does not split into new ones confirming the conclusions above that two conformers or tautomers are not causing the *NH* signal broadening at RT.

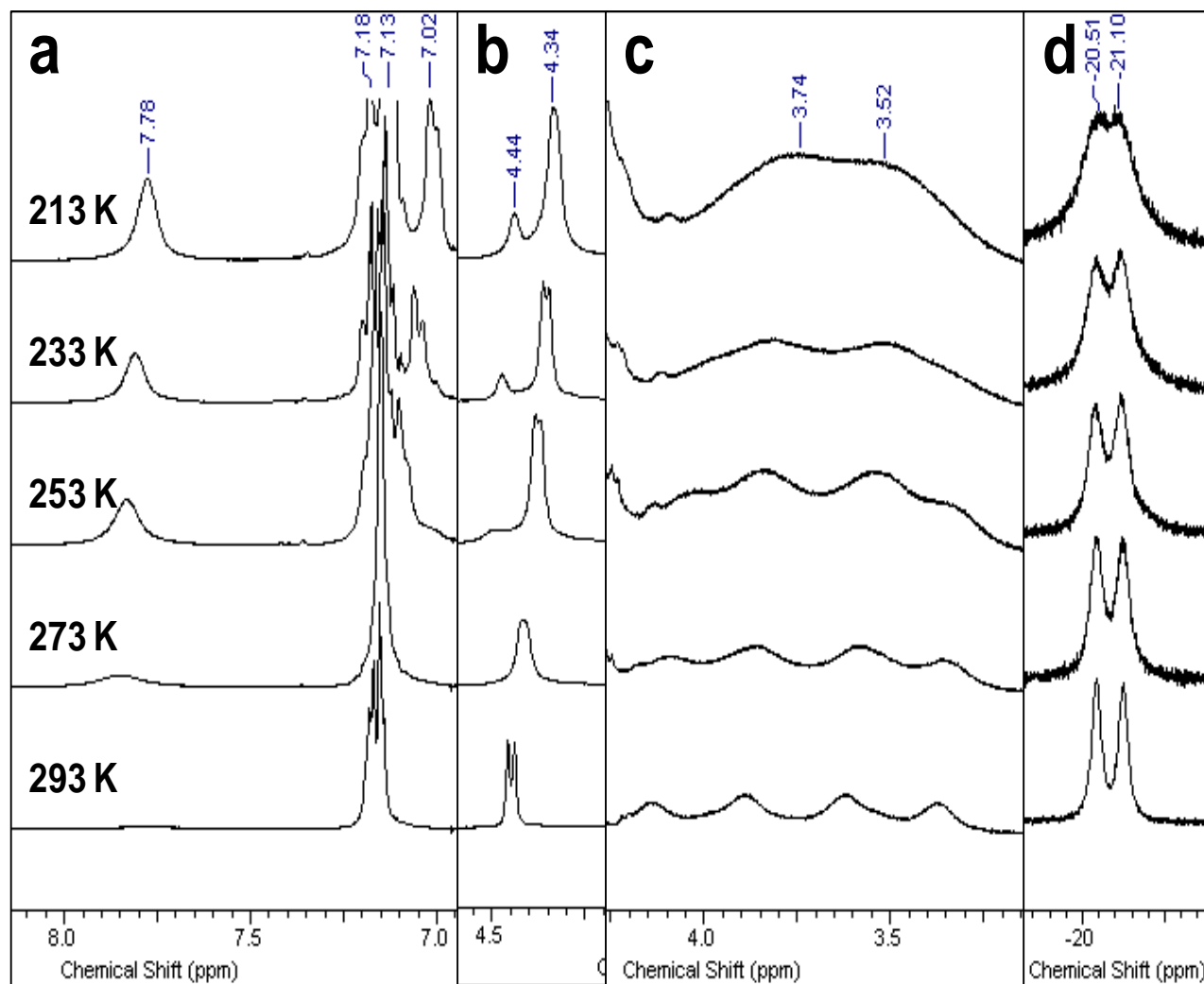


**Figure S2.** VT NMR spectra of **NHHB** in  $\text{CD}_2\text{Cl}_2$ . a) *NH* (around 7.8 ppm) and  $\text{C}_6\text{H}_4$  (around 7.1 ppm)  $^1\text{H}$  NMR signals; b)  $\text{CH}_2$   $^1\text{H}$  NMR signals; c) *BH*  $^1\text{H}$  NMR signals; d)  $^{11}\text{B}$  NMR signals.

Acquisition Time (sec) 6.0293

Frequency (MHz)	300.13	Nucleus	<sup>1</sup> H	Number of Transients	128	Origin	arx300
Original Points Count	32768	Owner	nmr3	Points Count	32768	Pulse Sequence	zg30
Receiver Gain	180.00	SW(cyclical) (Hz)	5434.78				
Spectrum Offset (Hz)	2089.3682	Sweep Width (Hz)	5434.62				

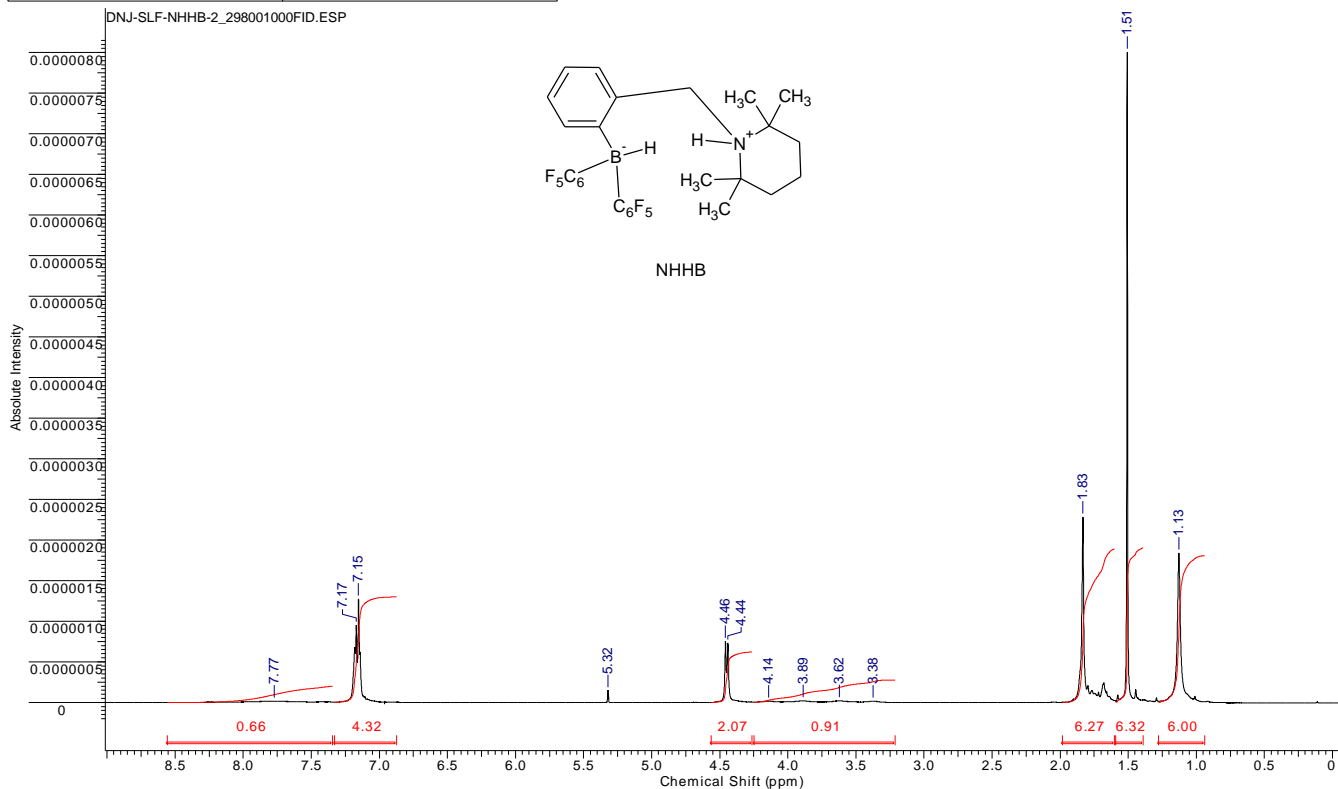


Figure S3. <sup>1</sup>H NMR spectrum of NHHB in CD<sub>2</sub>Cl<sub>2</sub> at RT.

Acquisition Time (sec) 6.0293 Comment 5 mm BBO BB-1H-19F-D-05

Frequency (MHz)	300.13	Nucleus	<sup>1</sup> H	Number of Transients	128	Origin	arx300	Original Points Count	32768
Owner	nmr3	Points Count	32768	Pulse Sequence	zg30	Receiver Gain	2860.00	SW(cyclical) (Hz)	5434.78
Solvent	DMSO-d6	Spectrum Offset (Hz)	2098.6548	Sweep Width (Hz)	5434.62	Temperature (degree C)	19.000		

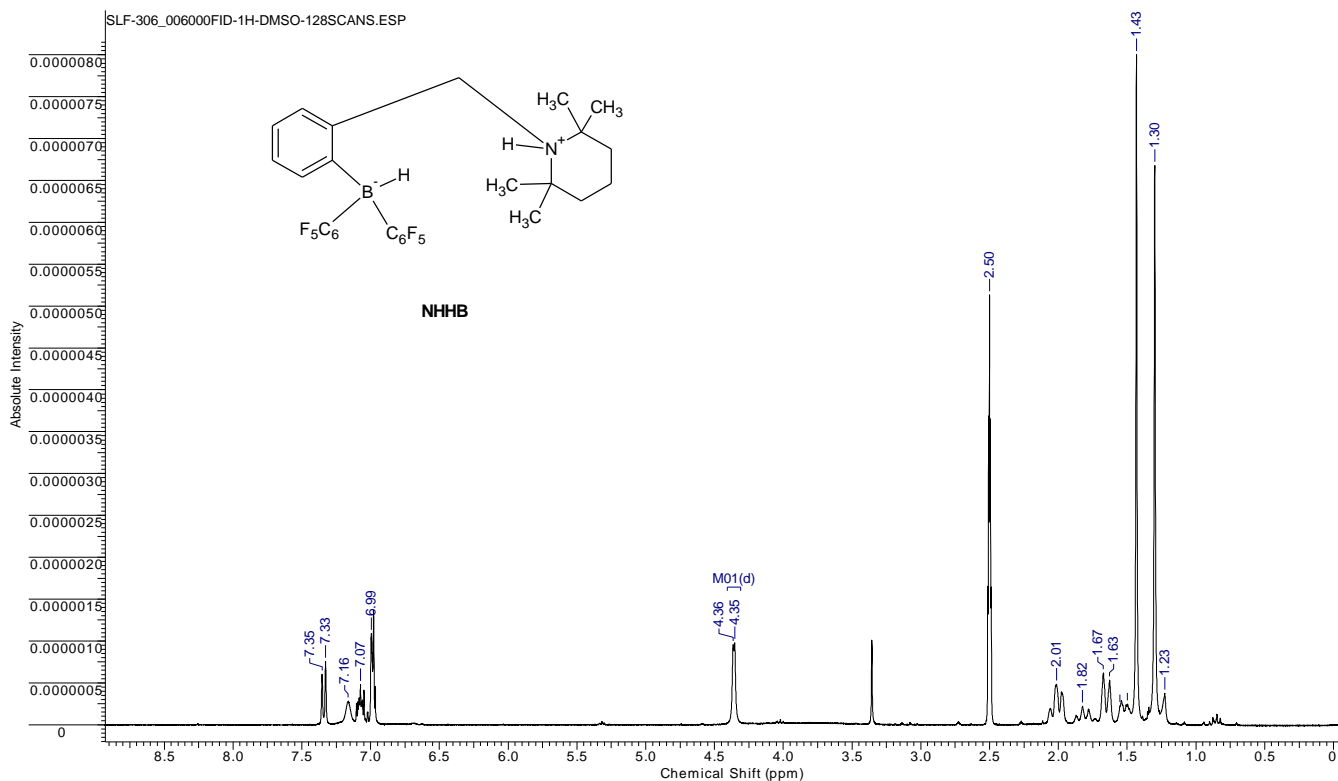


Figure S4. <sup>1</sup>H NMR spectrum of NHHB in DMSO-D<sub>6</sub> at RT.

Acquisition Time (sec)	1.6384	Comment	5 mm BBO BB-1H-19F-D-05		
Frequency (MHz)	96.29	Nucleus	11B	Number of Transients	64
Original Points Count	32768	Owner	root	Points Count	32768
Receiver Gain	5700.00	SW(cyclical) (Hz)	20000.00	Pulse Sequence	zg
Spectrum Offset (Hz)	-321.6909	Sweep Width (Hz)	19999.39	Temperature (degree C)	27.000

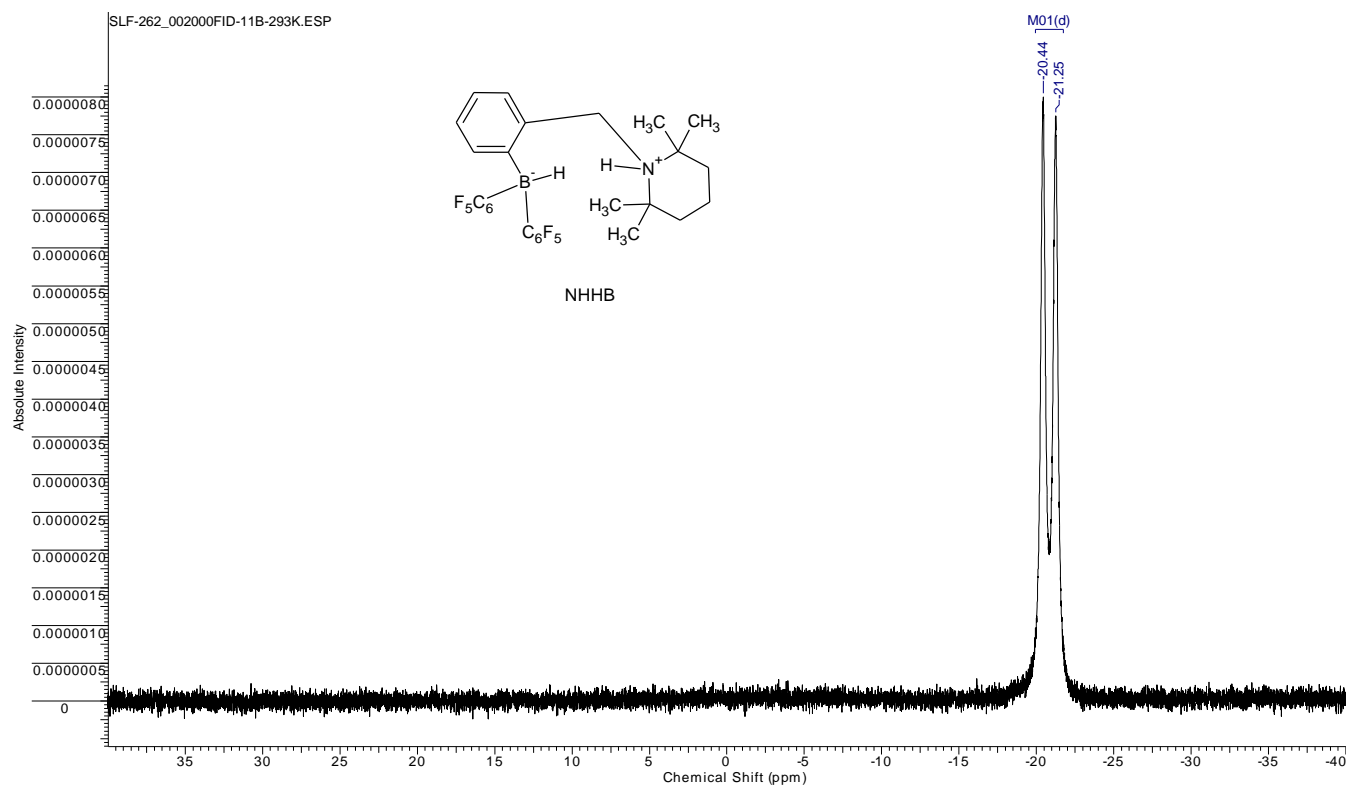


Figure S5.  $^{11}\text{B}$  NMR spectrum of NHHB in  $\text{CD}_2\text{Cl}_2$  at RT.

Acquisition Time (sec)	1.0486	Comment	5 mm BBO BB-1H-19F-D-05		
Frequency (MHz)	282.40	Nucleus	19F	Number of Transients	16
Original Points Count	65536	Owner	psm	Points Count	65536
Receiver Gain	64.00	SW(cyclical) (Hz)	62500.00	Solvent	DICHLOROMETHANE-d2
Spectrum Offset (Hz)	-22886.9141	Sweep Width (Hz)	62499.05	Temperature (degree C)	27.000

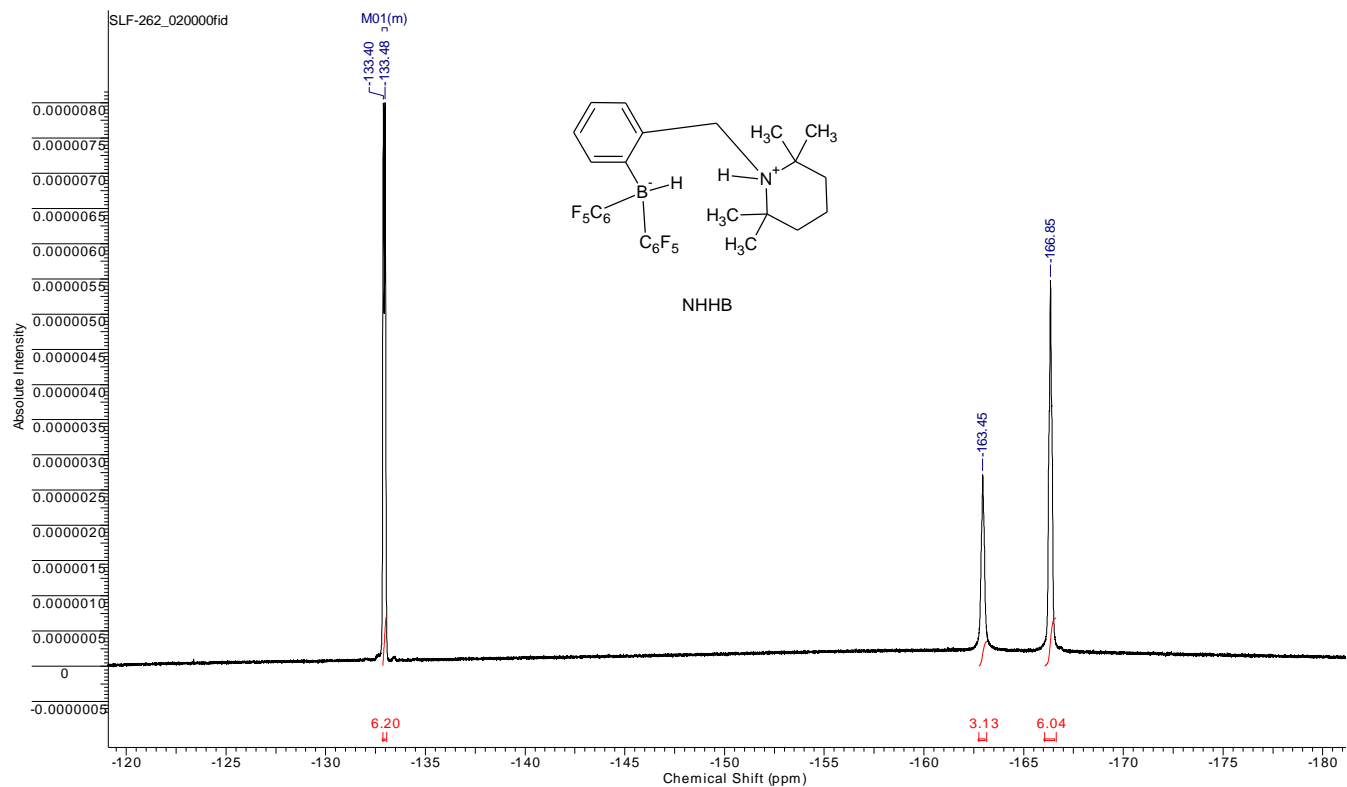
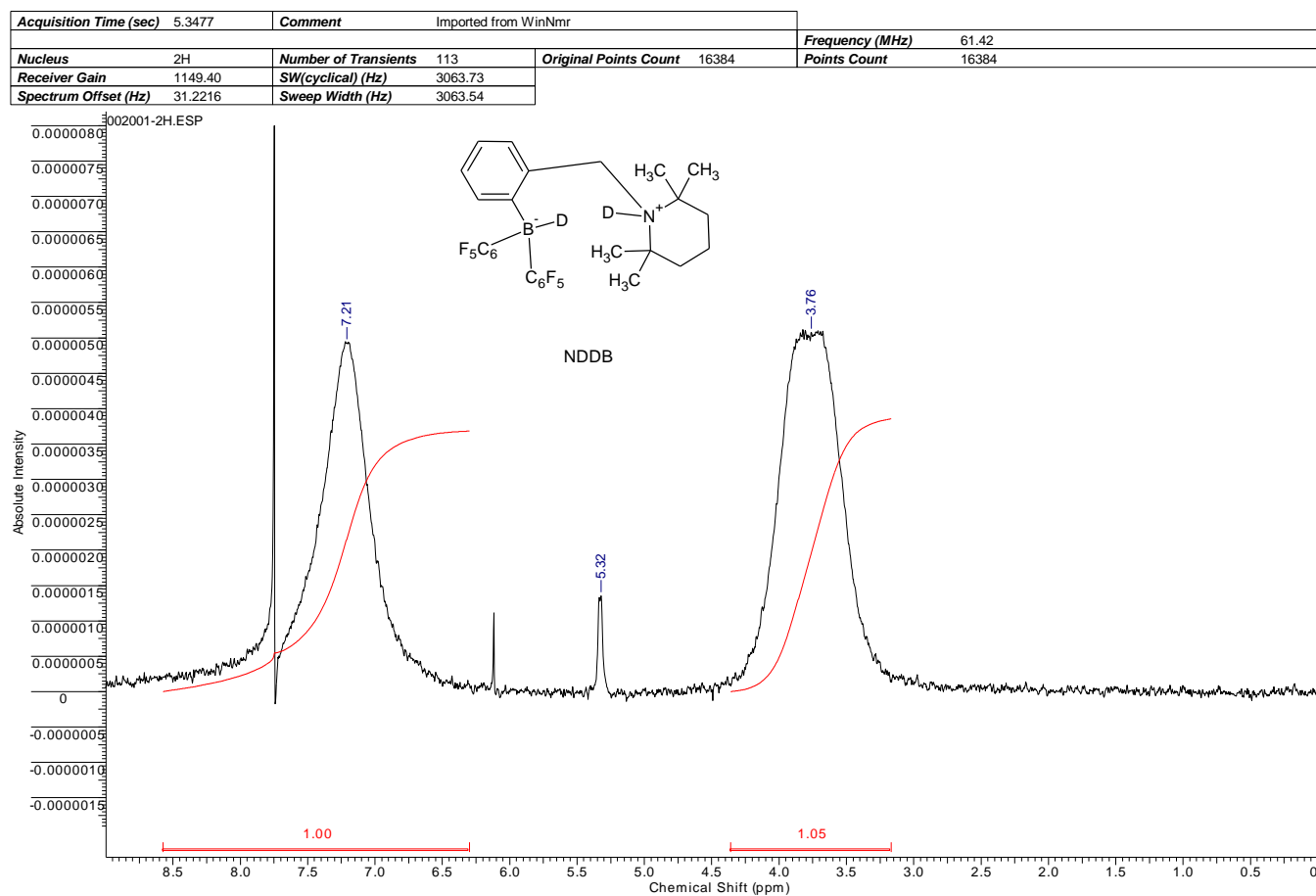
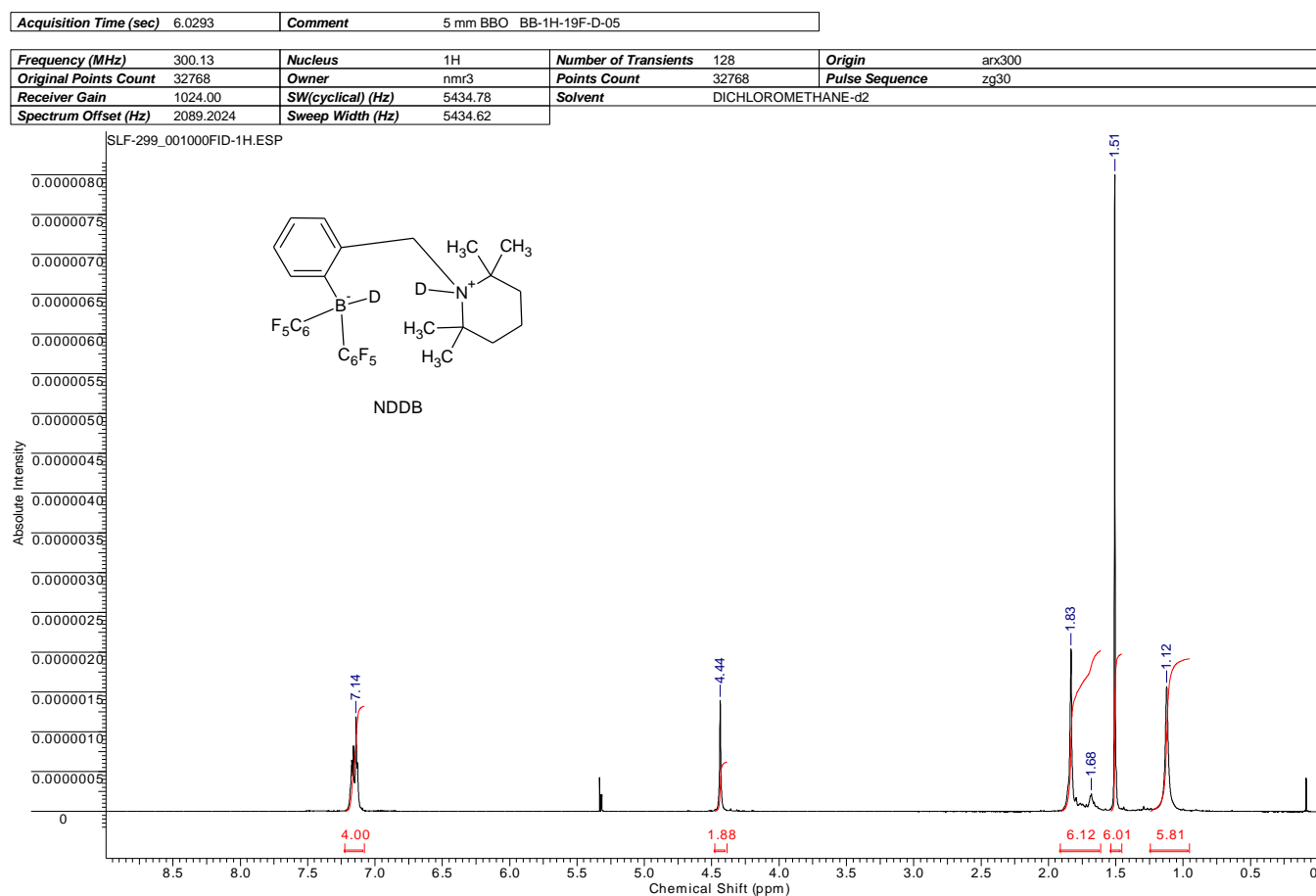


Figure S6.  $^{19}\text{F}$  NMR spectrum of NHHB in  $\text{CD}_2\text{Cl}_2$  at RT.



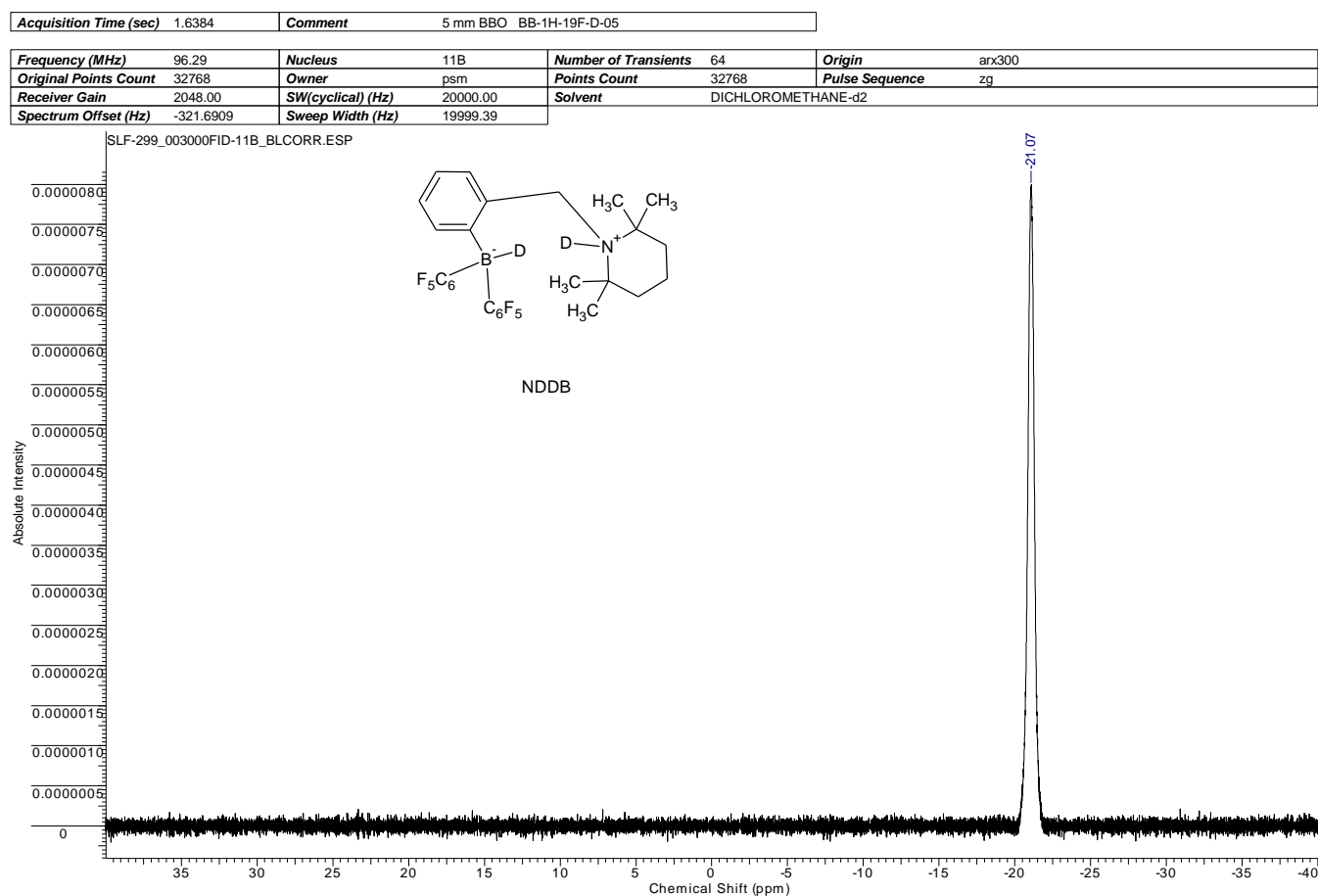


Figure S9.  $^{11}\text{B}$  NMR spectrum of NDDb in  $\text{CD}_2\text{Cl}_2$  at RT.

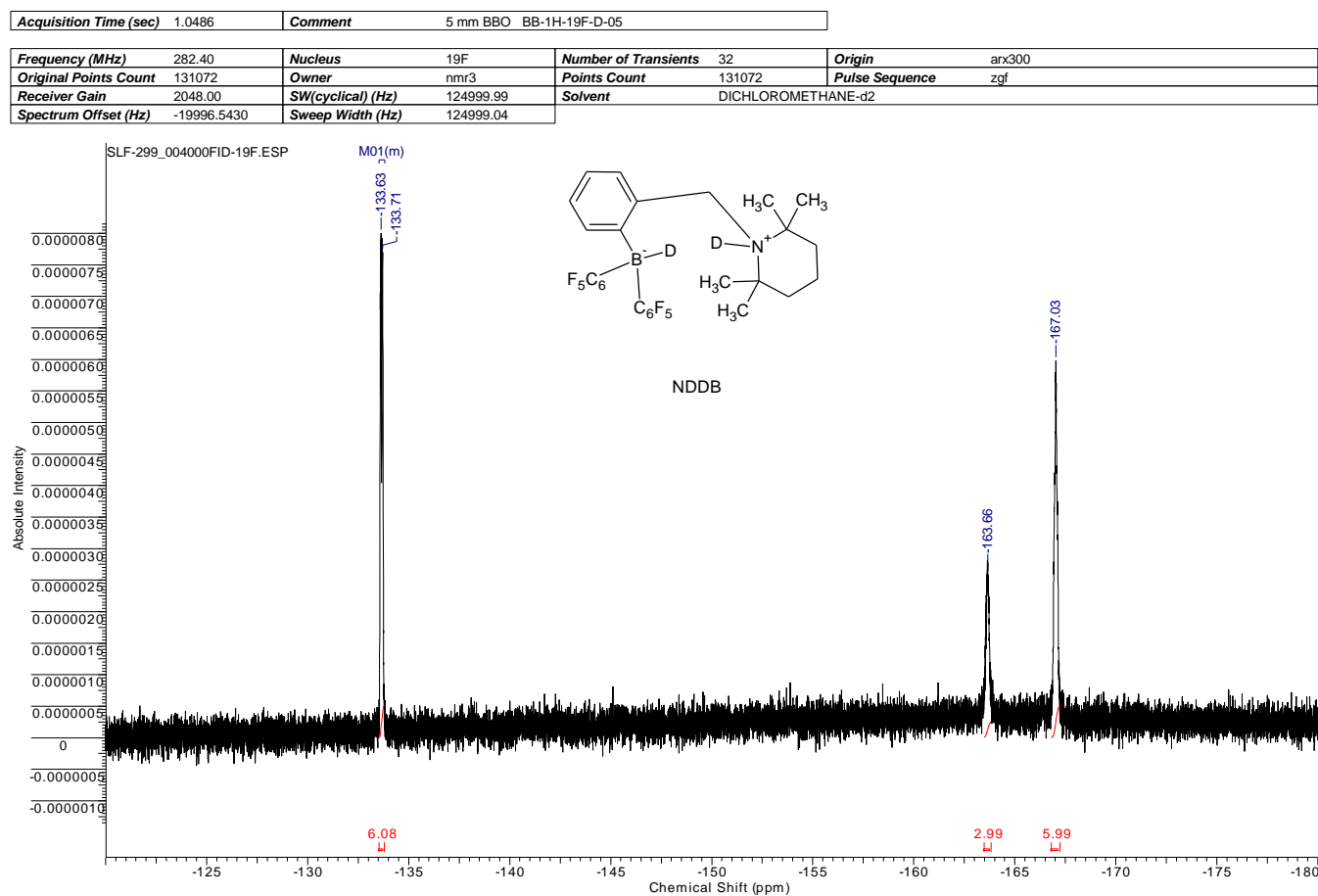
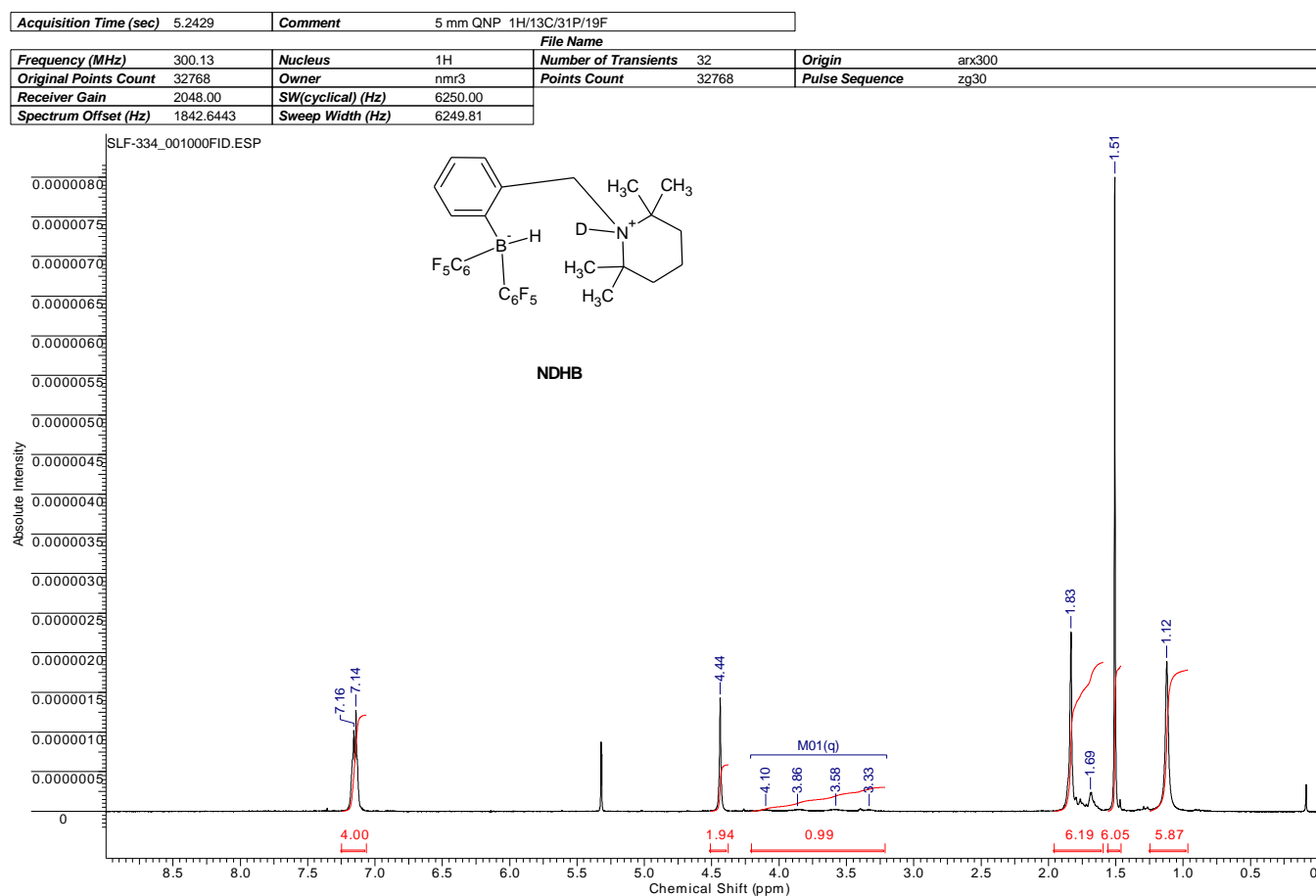
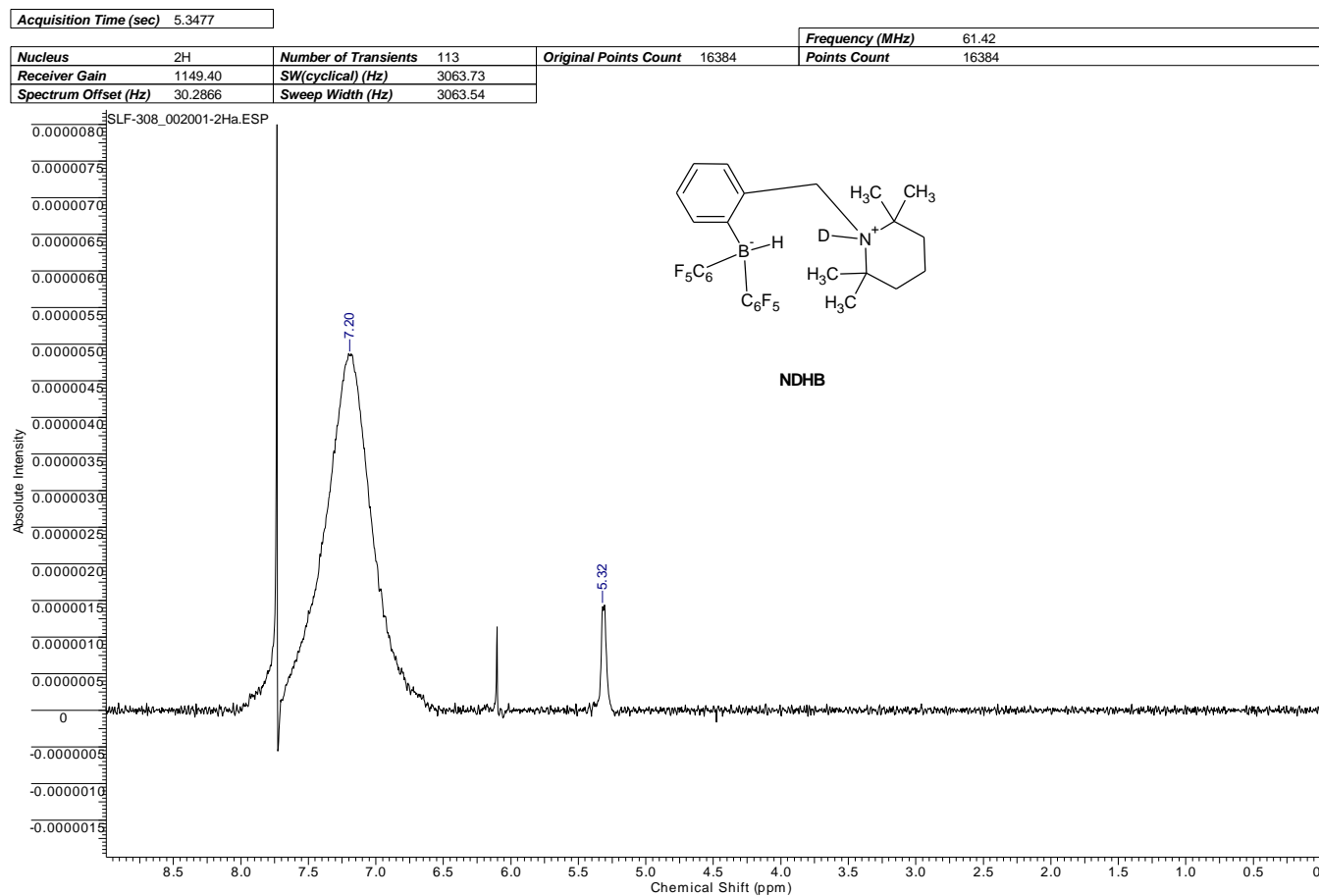


Figure S10.  $^{19}\text{F}$  NMR spectrum of NDDb in  $\text{CD}_2\text{Cl}_2$  at RT.





**Figure S11.**  $^1\text{H}$  NMR spectrum of **NDHB** in  $\text{CD}_2\text{Cl}_2$  at RT.



**Figure S12.**  $^2\text{H}$  NMR spectrum of **NDHB** in  $\text{CH}_2\text{Cl}_2$  at RT.

Acquisition Time (sec)	1.6384	Comment	5 mm BBO BB-1H-19F-D-05
------------------------	--------	---------	-------------------------

Frequency (MHz)	96.29	Nucleus	11B	Number of Transients	64	Origin	arx300
Original Points Count	32768	Owner	psm	Points Count	32768	Pulse Sequence	zg
Receiver Gain	2048.00	SW(cyclical) (Hz)	20000.00	Solvent	DICHLOROMETHANE-d2		
Spectrum Offset (Hz)	-321.6909	Sweep Width (Hz)	19999.39				

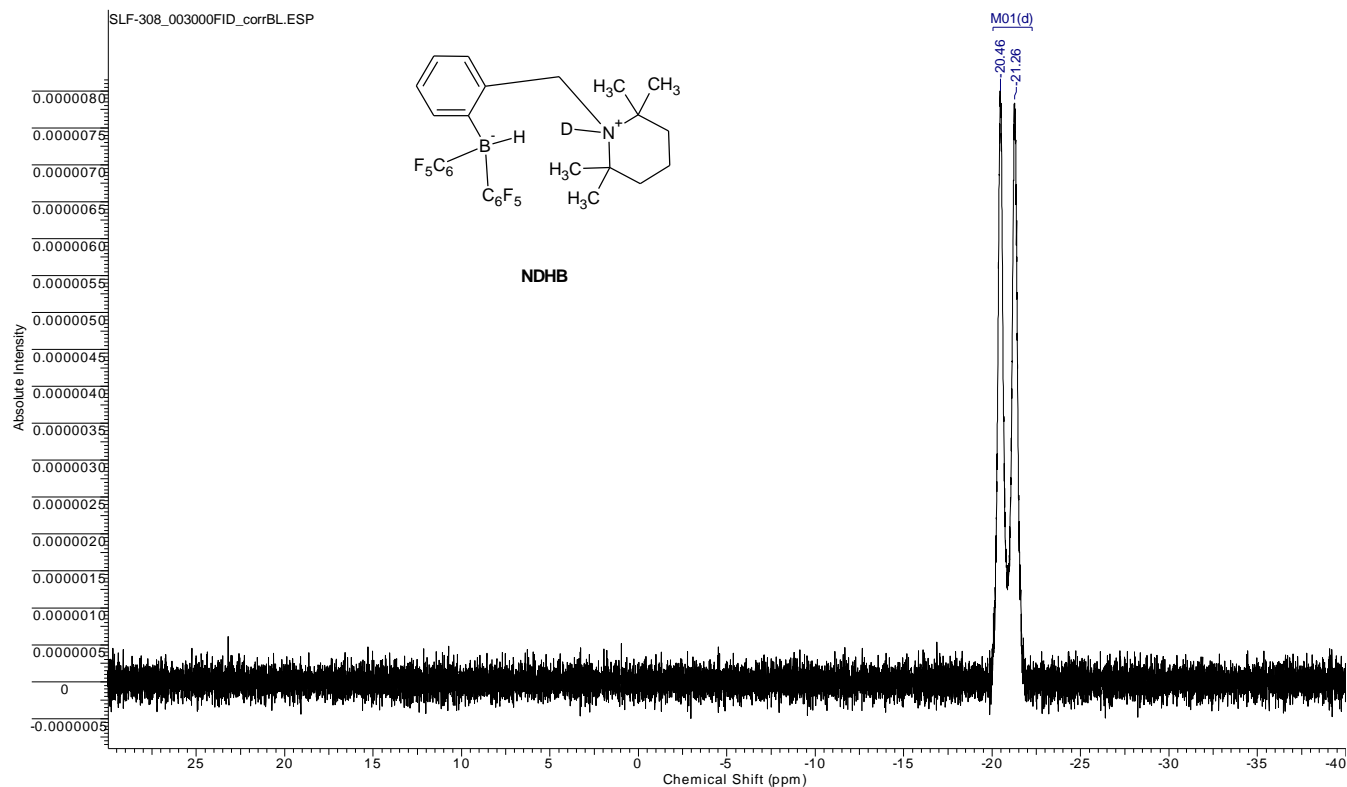


**Figure S13.** <sup>11</sup>B NMR spectrum of NDHB in CD<sub>2</sub>Cl<sub>2</sub> at RT.

Acquisition Time (sec)	1.0486	Comment	5 mm QNP 1H/13C/31P/19F
------------------------	--------	---------	-------------------------

Frequency (MHz)	282.40	Nucleus	<sup>19</sup> F	Number of Transients	128	Origin	arx300
Original Points Count	131072	Owner	nmr3	Points Count	131072	Pulse Sequence	zg
Receiver Gain	1430.00	SW(cyclical) (Hz)	124999.99	Solvent	DICHLOROMETHANE-d2		
Spectrum Offset (Hz)	-20003.2422	Sweep Width (Hz)	124999.04				

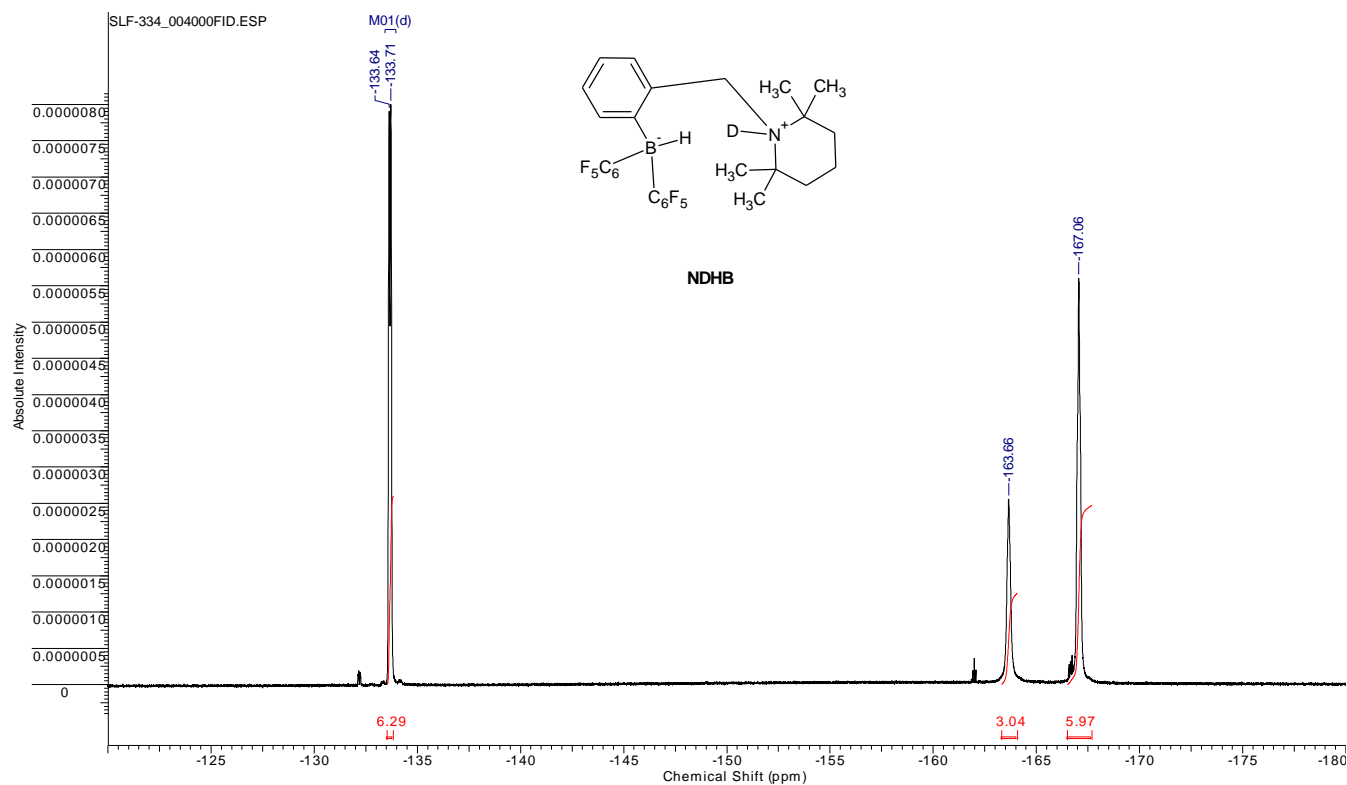


**Figure S14.** <sup>19</sup>F NMR spectrum of NDHB in CD<sub>2</sub>Cl<sub>2</sub> at RT.

Acquisition Time (sec)	5.2429	Comment	5 mm QNP 1H/13C/31P/19F
------------------------	--------	---------	-------------------------

Frequency (MHz)	300.13	Nucleus	1H	Number of Transients	128	Origin	arx300
Original Points Count	32768	Owner	nmr3	Points Count	32768	Pulse Sequence	zg30
Receiver Gain	1430.00	SW(cyclical) (Hz)	6250.00	Solvent	DICHLOROMETHANE-d2		
Spectrum Offset (Hz)	1842.6444	Sweep Width (Hz)	6249.81				

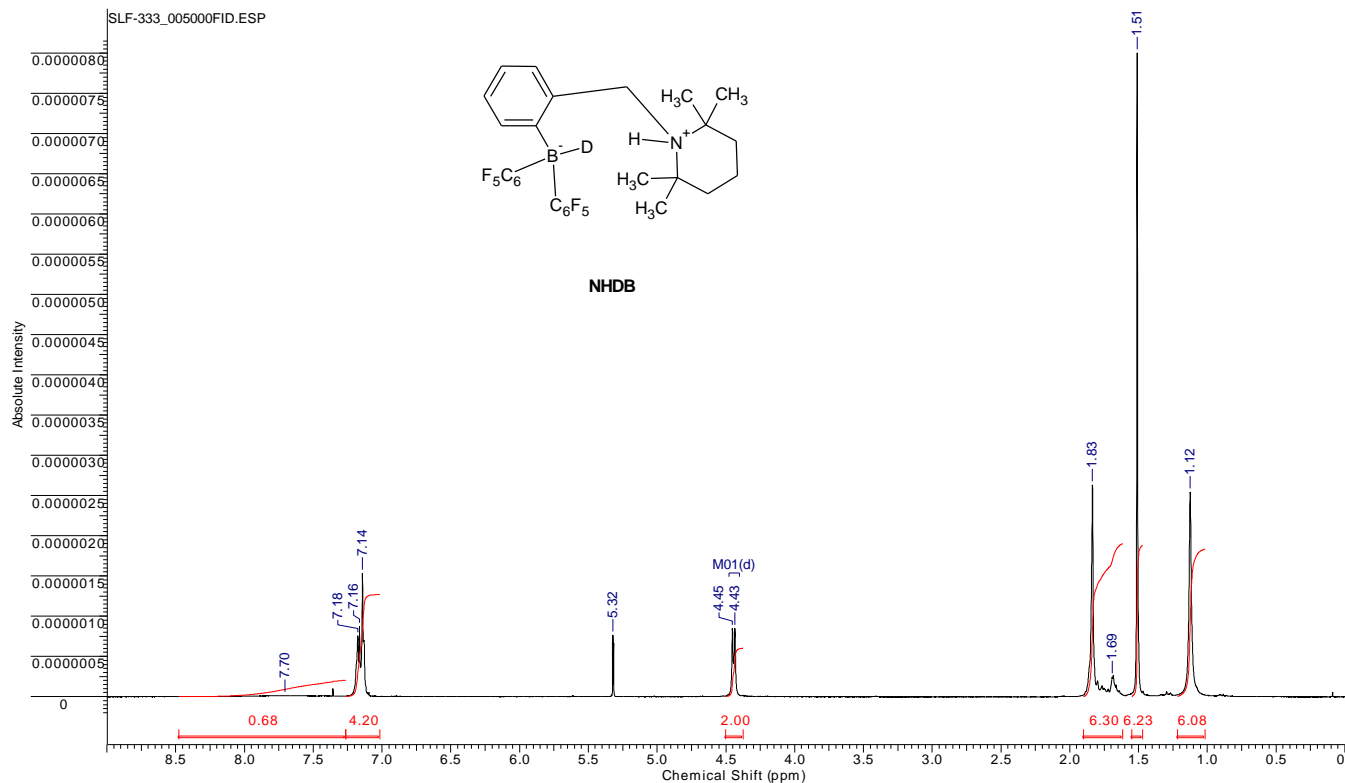


Figure S15.  $^1\text{H}$  NMR spectrum of NHDB in  $\text{CD}_2\text{Cl}_2$  at RT.

Acquisition Time (sec)	5.3477	Comment	Imported from WinNmr	Frequency (MHz)	61.42	Nucleus	$^2\text{H}$	Number of Transients	124
Original Points Count	16384	Points Count	16384	Receiver Gain	1024.00	SW(cyclical) (Hz)	3063.73		
				Spectrum Offset (Hz)	1.4894	Sweep Width (Hz)	3063.54		

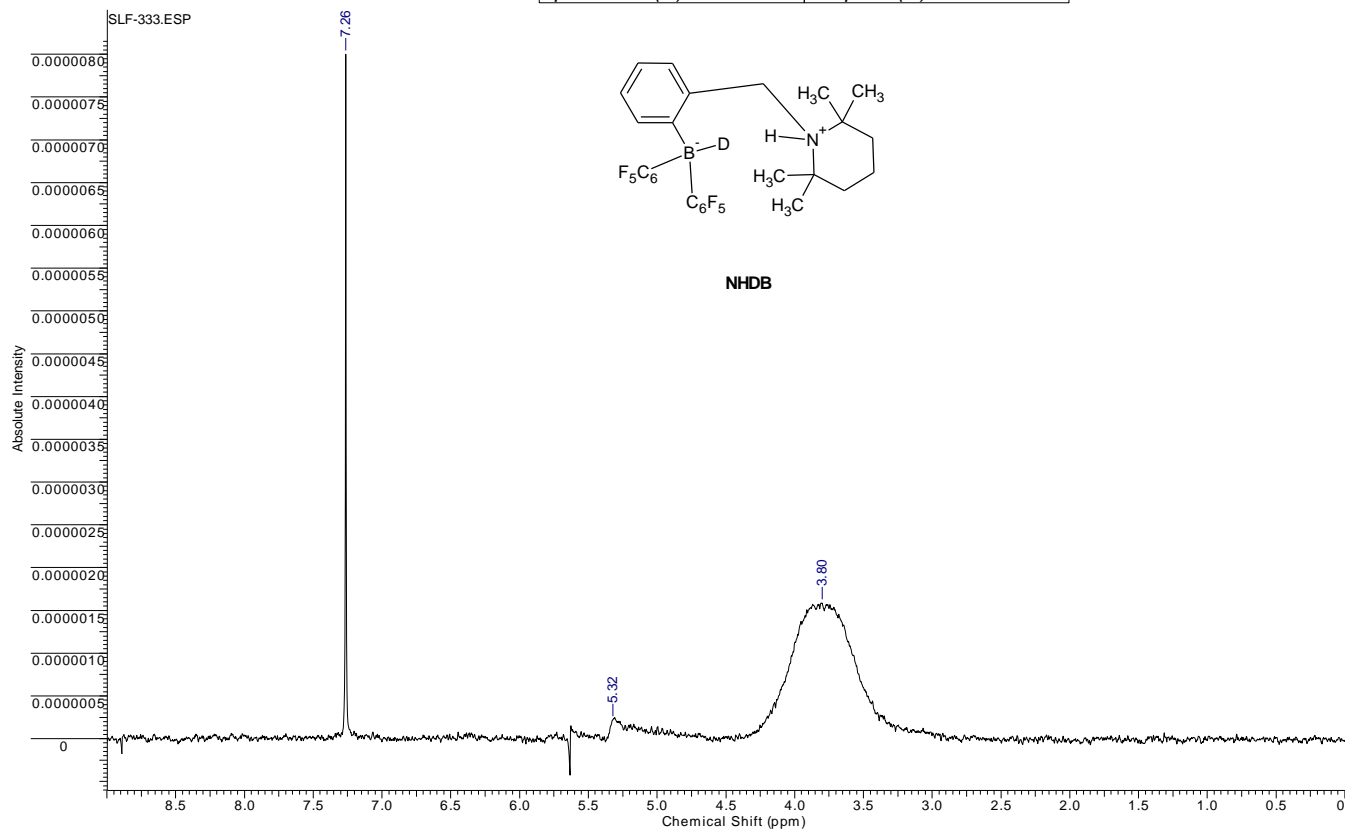


Figure S16.  $^2\text{H}$  NMR spectrum of NHDB in  $\text{CH}_2\text{Cl}_2$  at RT.



Acquisition Time (sec) 5.2429		Comment 5 mm QNP 1H/13C/31P/19F							
Frequency (MHz) 300.13		Nucleus 1H		Number of Transients 128		Origin arx300		Original Points Count 32768	
Owner root		Points Count 32768		Pulse Sequence zg30		Receiver Gain 1430.00		SW(cyclical) (Hz) 6250.00	
				Spectrum Offset (Hz) 1842.4535		Sweep Width (Hz) 6249.81			

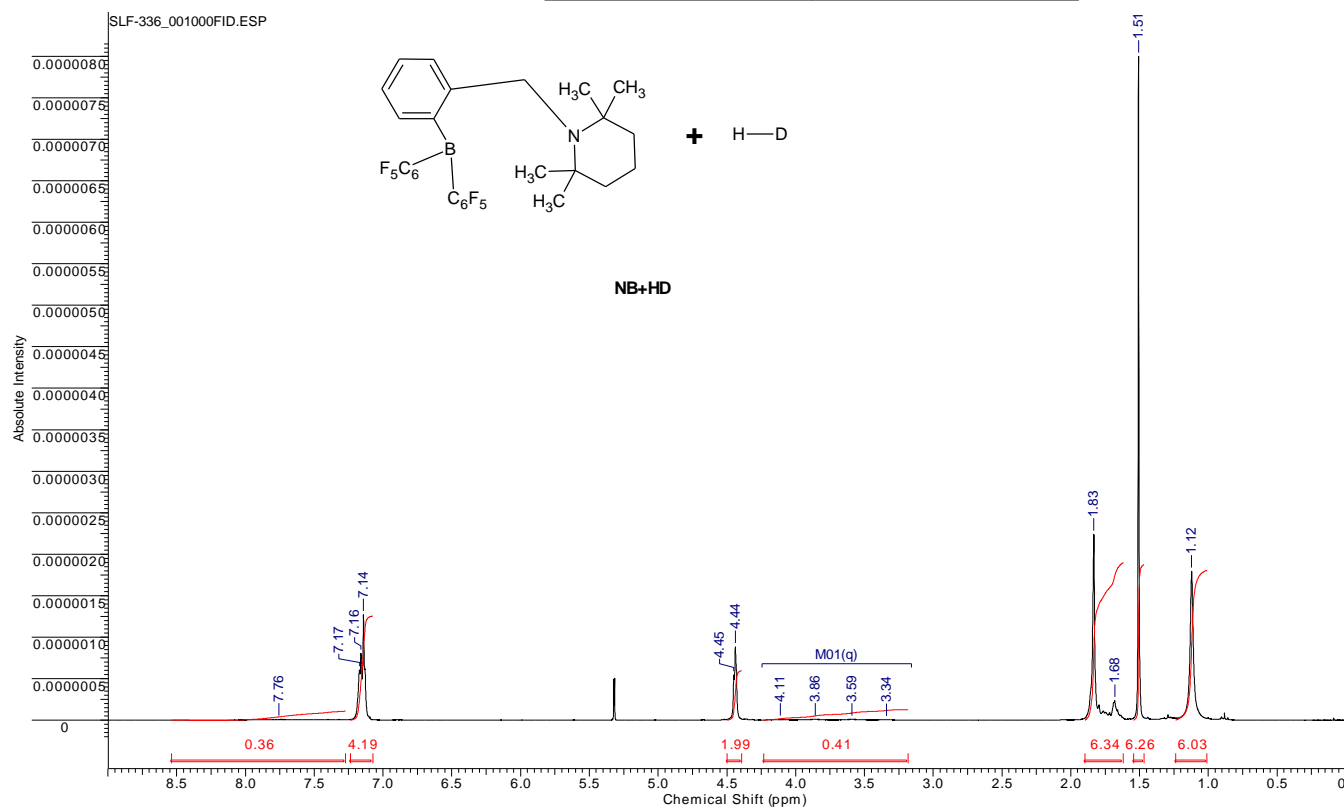


Figure S19.  $^1\text{H}$  NMR spectrum of the reaction products of the reaction **NHNB** + HD in  $\text{CD}_2\text{Cl}_2$  at RT.

Acquisition Time (sec)	5.3477	Comment			Imported from WinNmr		
					Frequency (MHz)	61.42	
Nucleus	2H	Number of Transients	134	Original Points Count	16384	Points Count	16384
Receiver Gain	1149.40	SW(cyclical) (Hz)	3063.73				
Spectrum Offset (Hz)	31.4086	Sweep Width (Hz)	3063.54				

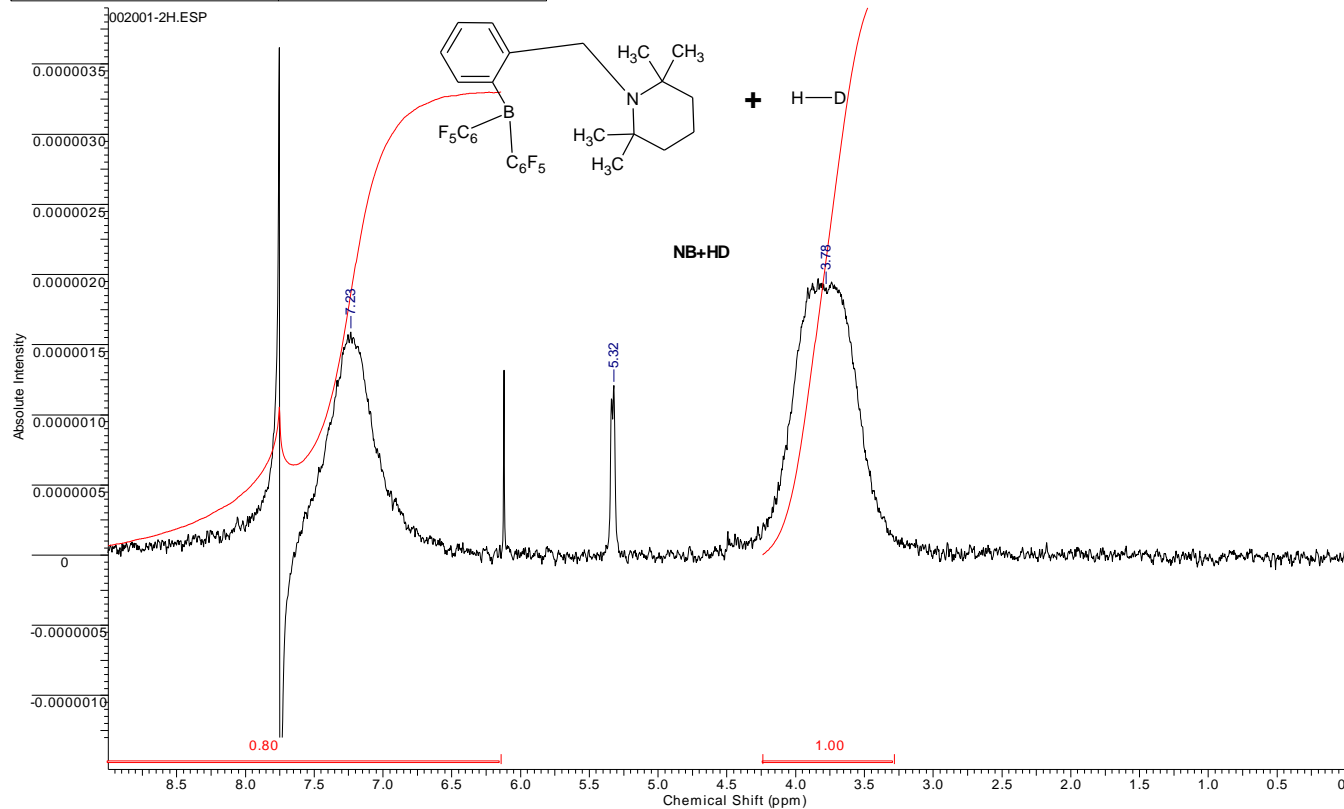
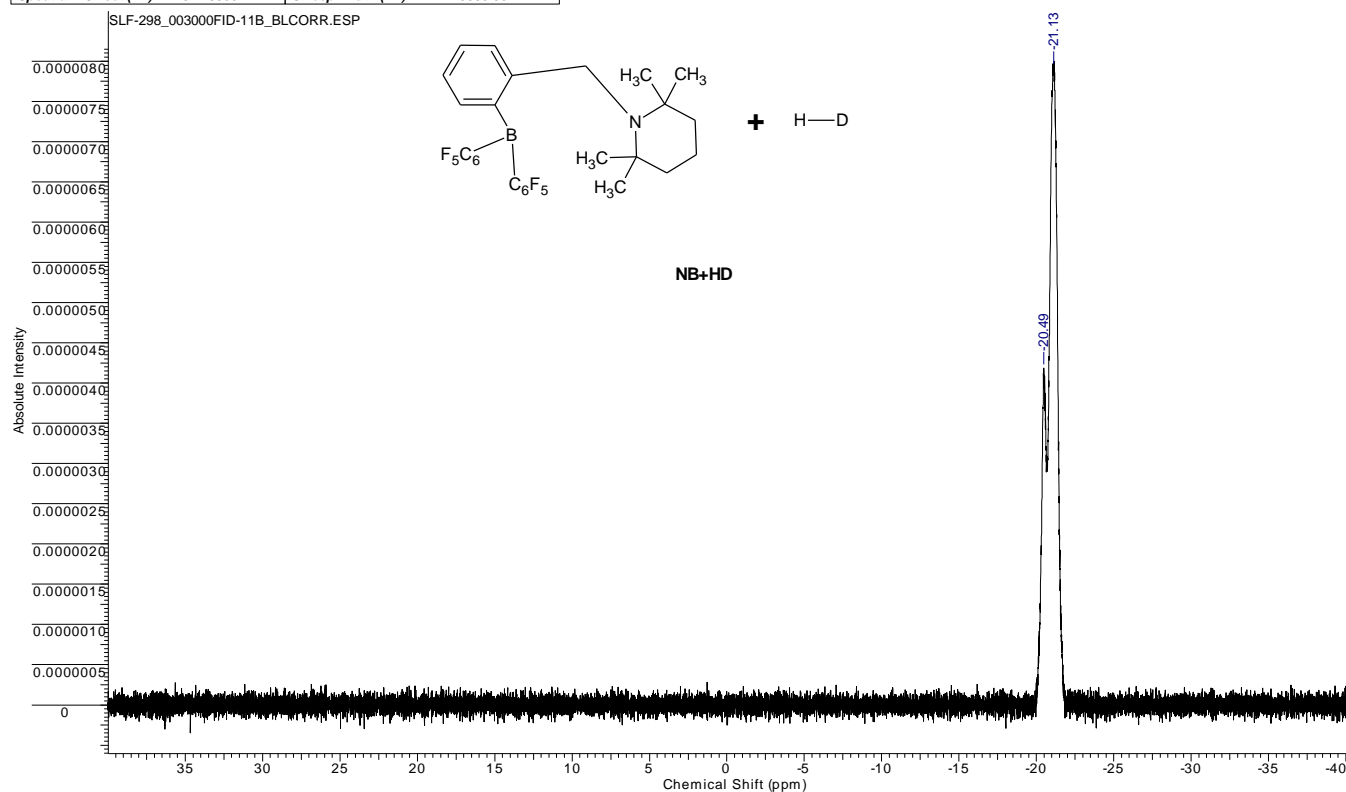


Figure S20.  $^2\text{H}$  NMR spectrum of the reaction products of **NHNB** + HD in  $\text{CH}_2\text{Cl}_2$  at RT.

Acquisition Time (sec)	1.6384	Comment	5 mm BBO BB-1H-19F-D-05
------------------------	--------	---------	-------------------------

Frequency (MHz)	96.29	Nucleus	11B	Number of Transients	64	Origin	arx300
Original Points Count	32768	Owner	psm	Points Count	32768	Pulse Sequence	zg
Receiver Gain	2048.00	SW(cyclical) (Hz)	20000.00	Solvent	DICHLOROMETHANE-d2		
Spectrum Offset (Hz)	-321.6909	Sweep Width (Hz)	19999.39				



**Figure S21.**  $^{11}\text{B}$  NMR spectrum of the reaction products of **NBHB** + HD in  $\text{CD}_2\text{Cl}_2$  at RT.

Acquisition Time (sec)	1.0486	Comment	5 mm QNP 1H/13C/31P/19F
------------------------	--------	---------	-------------------------

Frequency (MHz)	282.40	Nucleus	19F	Number of Transients	128	Origin	arx300
Original Points Count	131072	Owner	nmr3	Points Count	131072	Pulse Sequence	zg
Receiver Gain	1024.00	SW(cyclical) (Hz)	124999.99	Solvent	DICHLOROMETHANE-d2		
Spectrum Offset (Hz)	-20004.1992	Sweep Width (Hz)	124999.04				

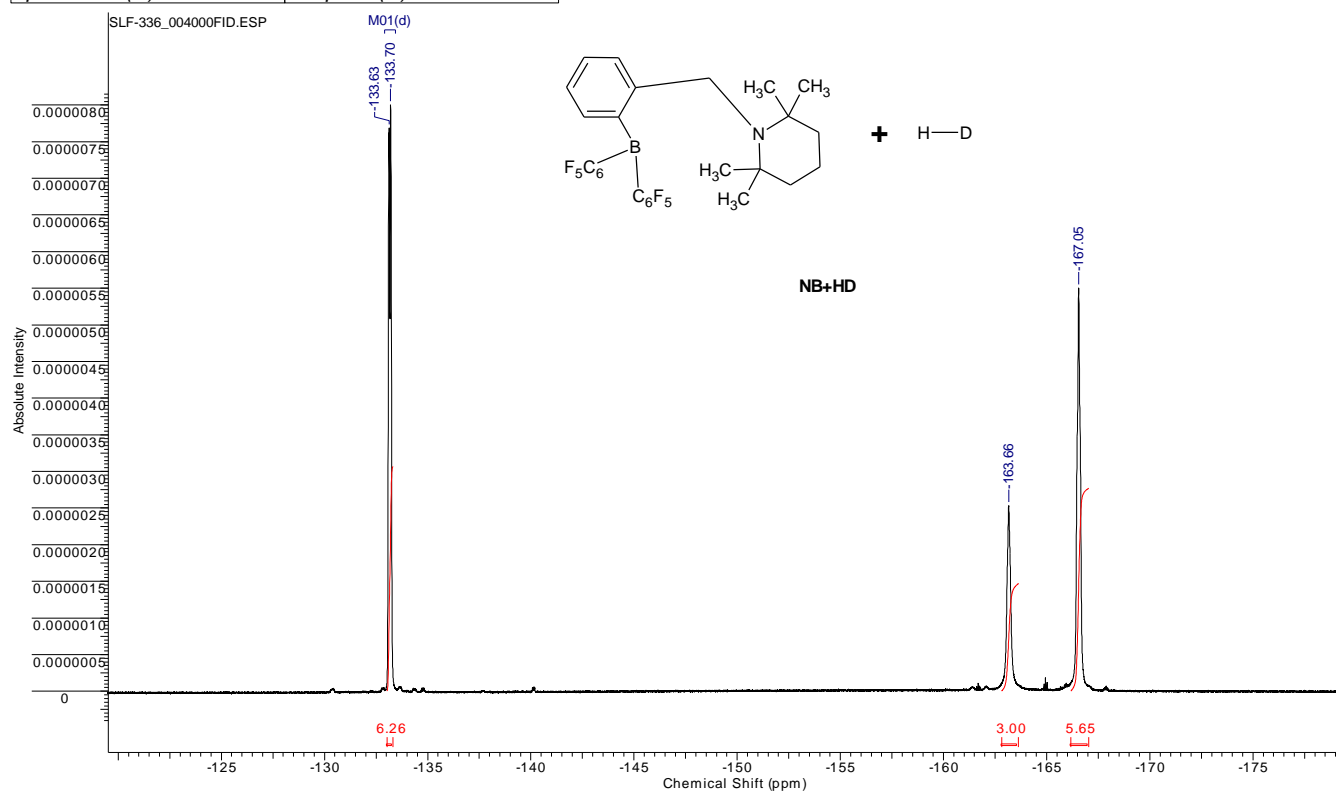


**Figure S22.**  $^{19}\text{F}$  NMR spectrum of the reaction products of **NBHB** + HD in  $\text{CD}_2\text{Cl}_2$  at RT.

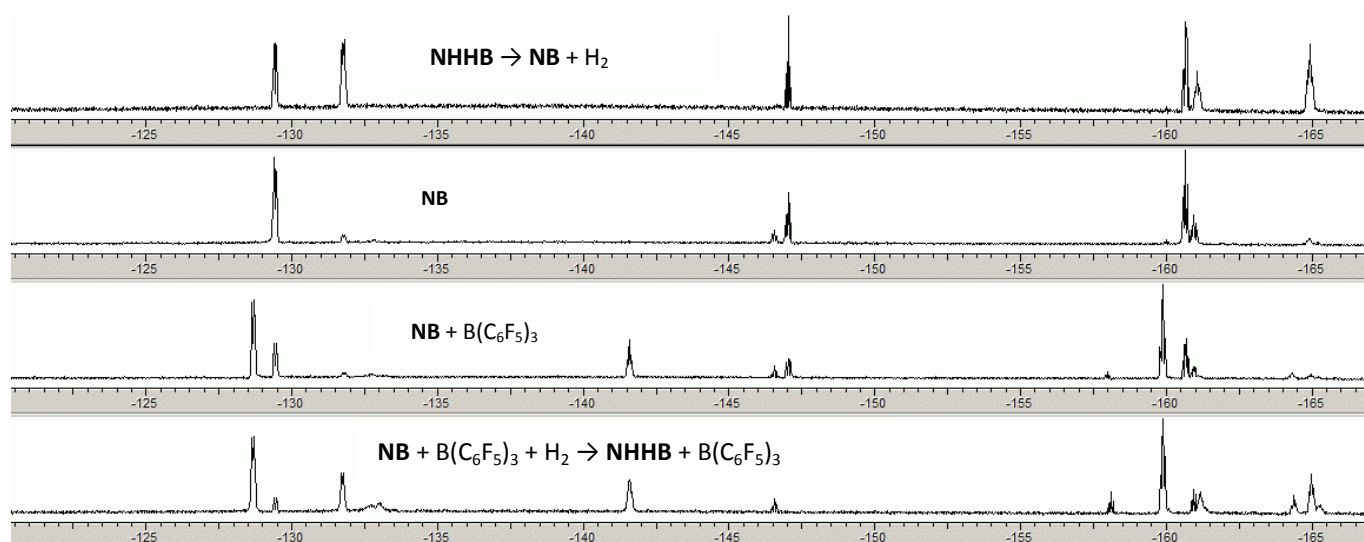


**Figure S23.**  $^{19}\text{F}$  NMR spectra at RT in  $\text{CD}_2\text{Cl}_2$ : The top spectrum shows the reaction products during the liberation process of  $\text{H}_2$  from NHHB at elevated temperatures in solution. The second spectrum shows pure **NB** (traces of water activation by **NB** visible). The third spectrum shows that no interaction is taking place between  $\text{B}(\text{C}_6\text{F}_5)_3$  and **NB** (traces of water activation visible). The bottom spectrum shows that  $\text{B}(\text{C}_6\text{F}_5)_3$  remains unchanged when present during the activation of  $\text{H}_2$  by **NB** (traces of water activation visible). The dissolved  $\text{B}(\text{C}_6\text{F}_5)_3$  does not seem to take part in the reaction  $\text{NB} + \text{H}_2 \rightarrow \text{NHHB}$  even though the B atom of  $\text{B}(\text{C}_6\text{F}_5)_3$  exhibits a much higher Lewis acidity than the B atom in **NB**.<sup>5</sup>

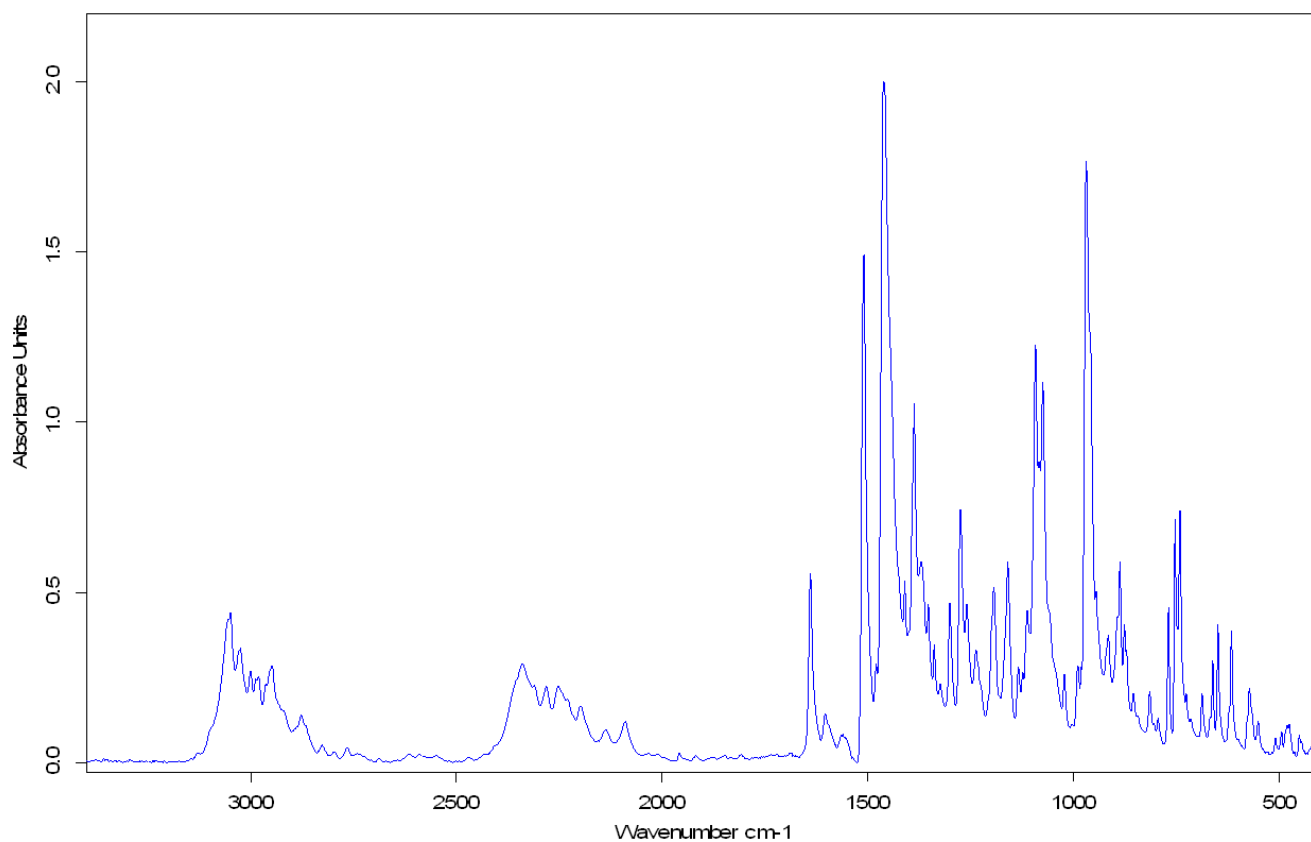


**Figure S24.** DRAFT-spectrum of **NHHB** without solvent.

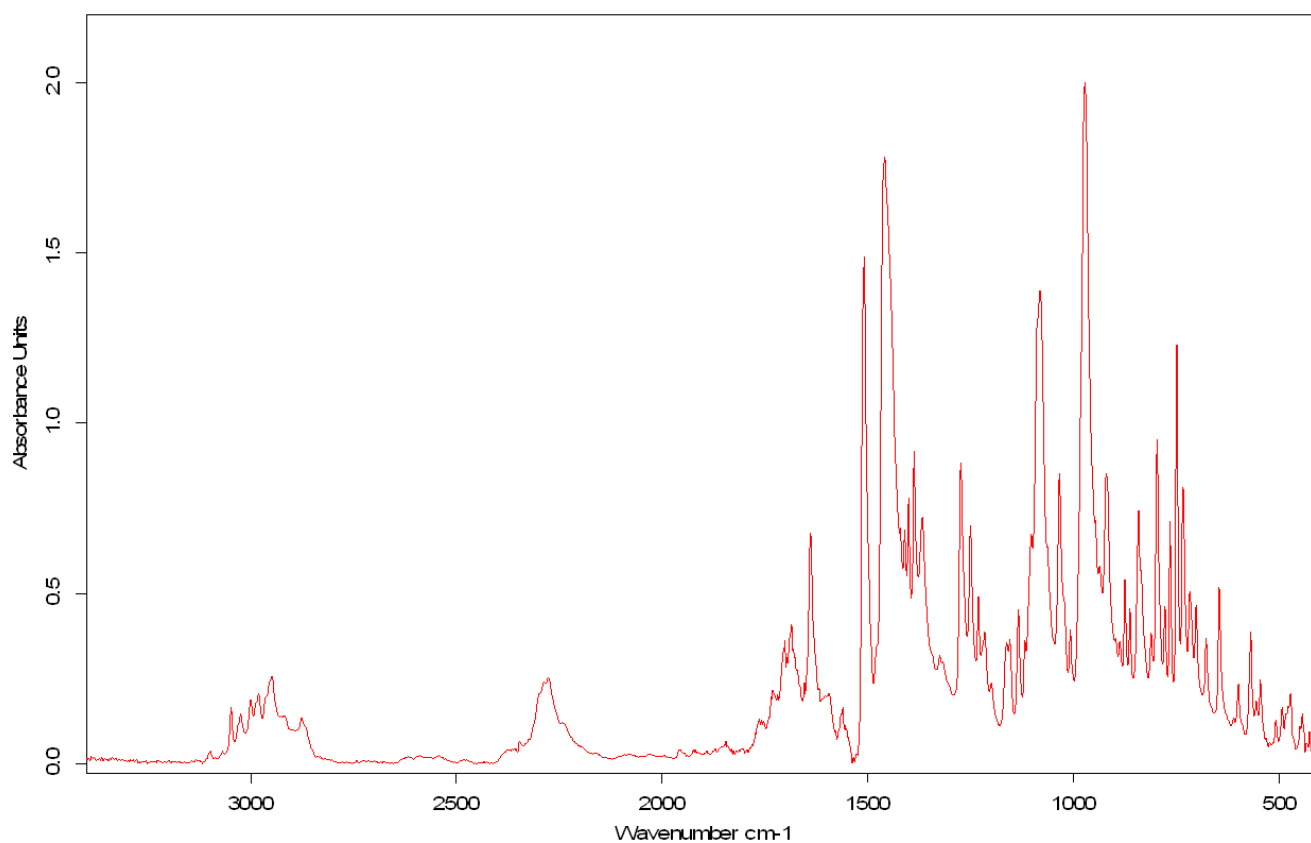


Figure S25. DRAFT-spectrum of **NDDB** without solvent.

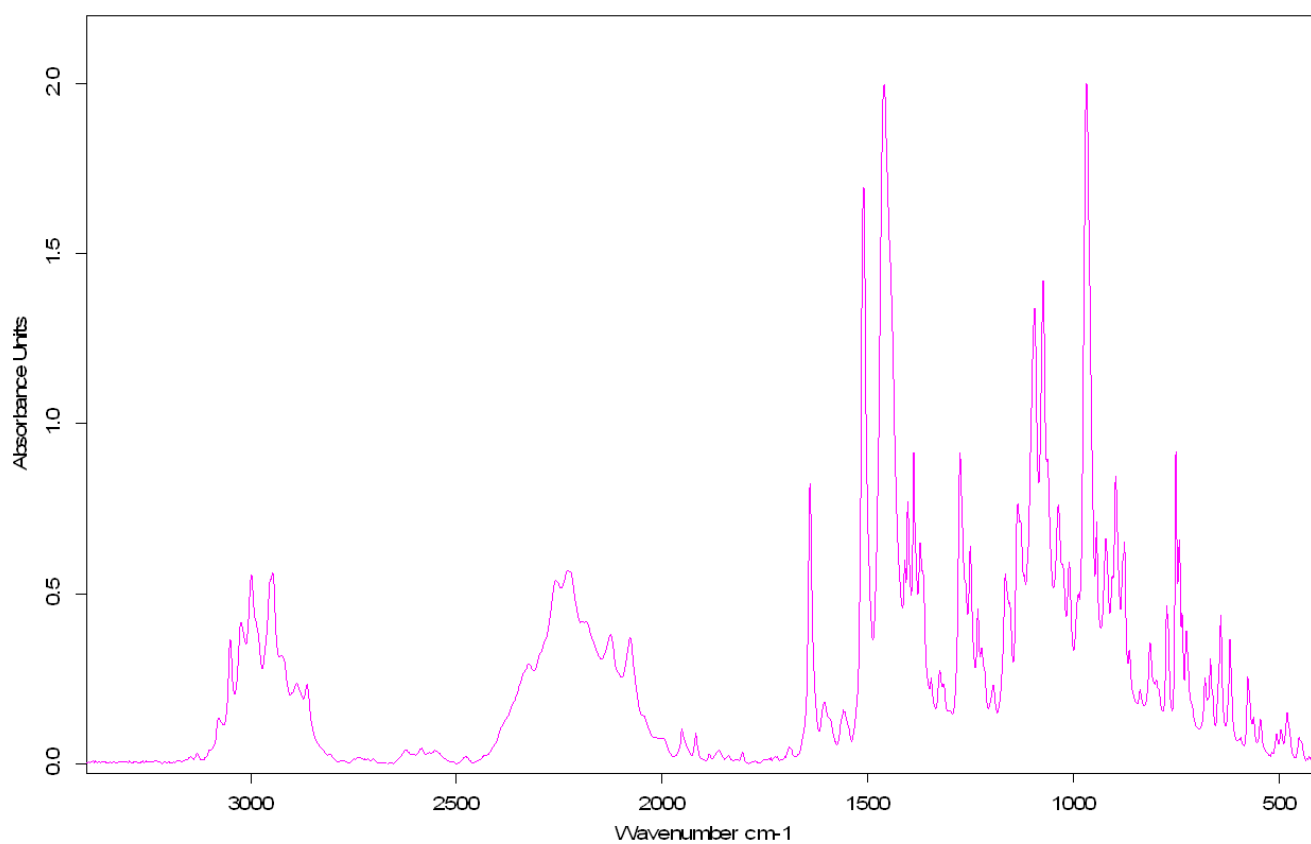
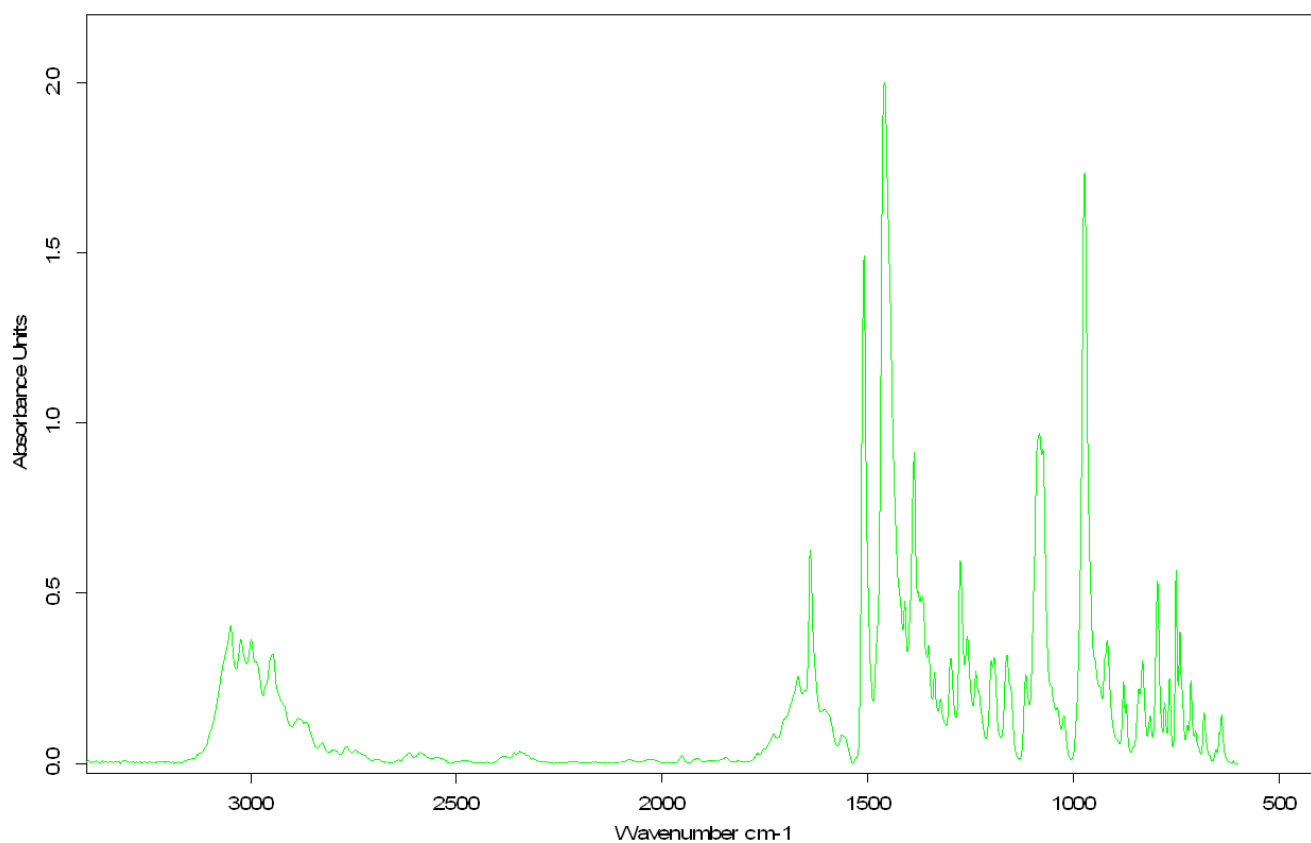
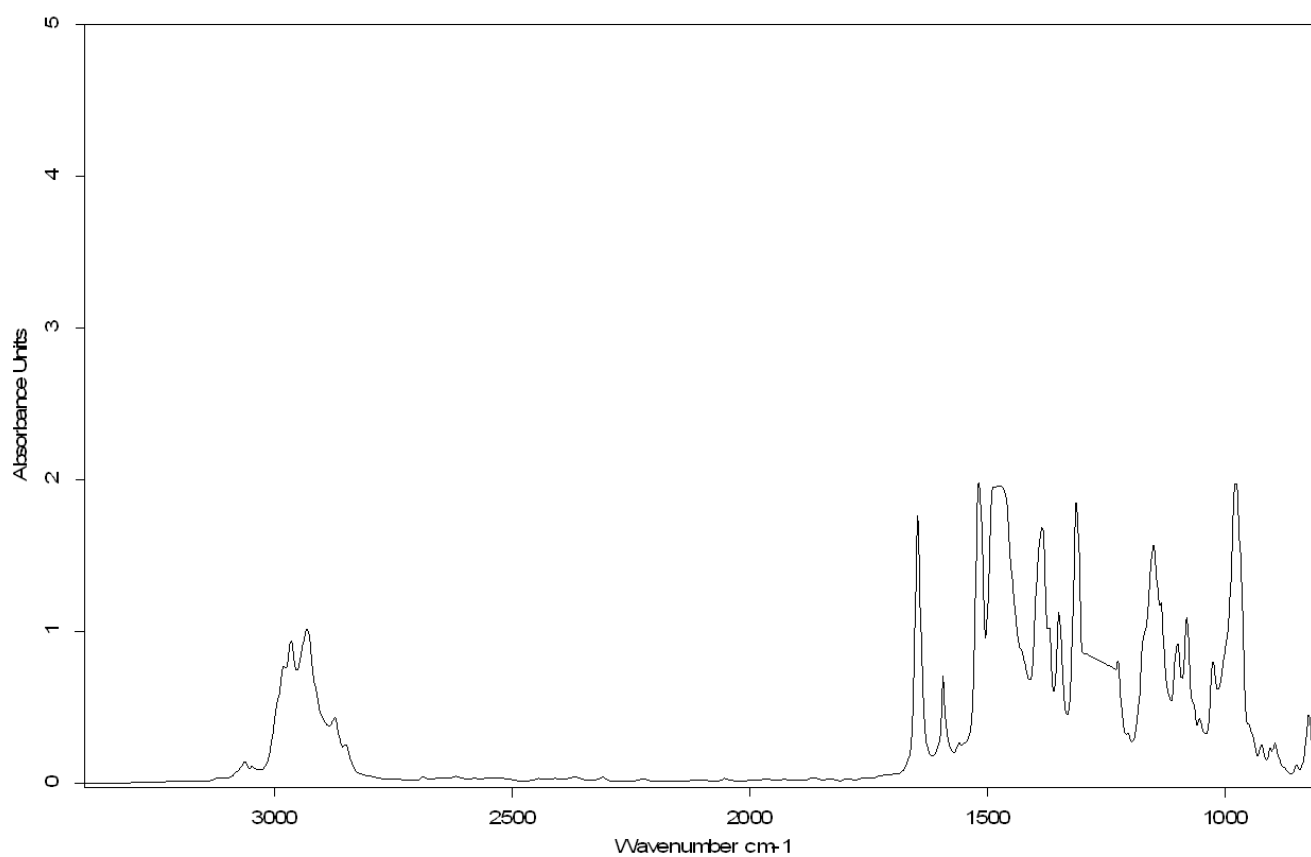


Figure S26. DRAFT-spectrum of **NDHB** without solvent.





**Figure S27.** DRAFT-spectrum of **NHDB** without solvent.



**Figure S28.** Absorption IR spectrum of **NB** solvated in  $\text{CH}_2\text{Cl}_2$  at 300 K. The spectrum of the solvent has been subtracted and the region from  $1300 - 1220 \text{ cm}^{-1}$  has been replaced by a straight line due to very strong solvent absorption bands.

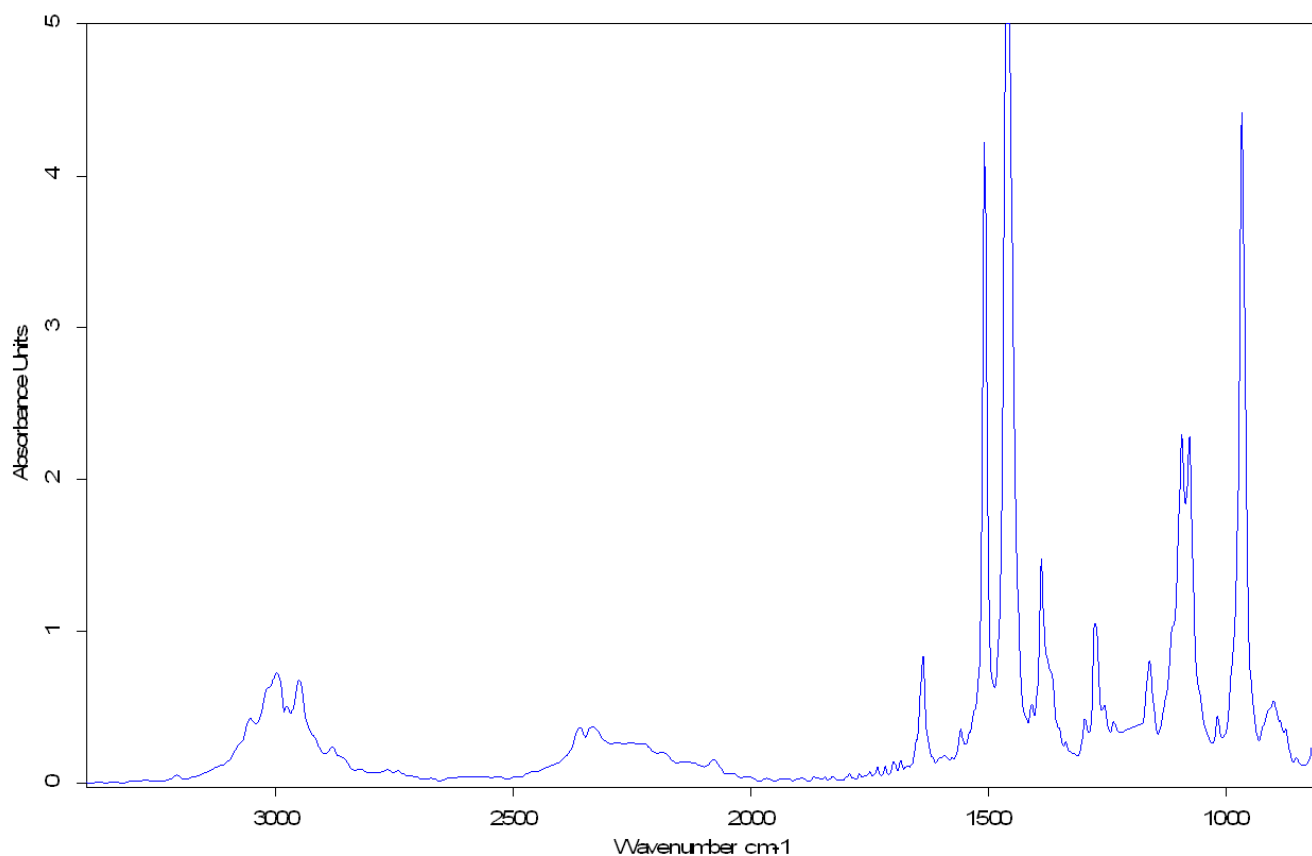


**Figure S29.** Absorption IR spectrum of **NHHB** solvated in  $\text{C}_2\text{H}_2\text{Cl}_4$  at 380 K. The spectrum of the solvent has been subtracted and the region from  $1220 - 1180 \text{ cm}^{-1}$  has been replaced by a straight line due to very strong solvent absorption bands.

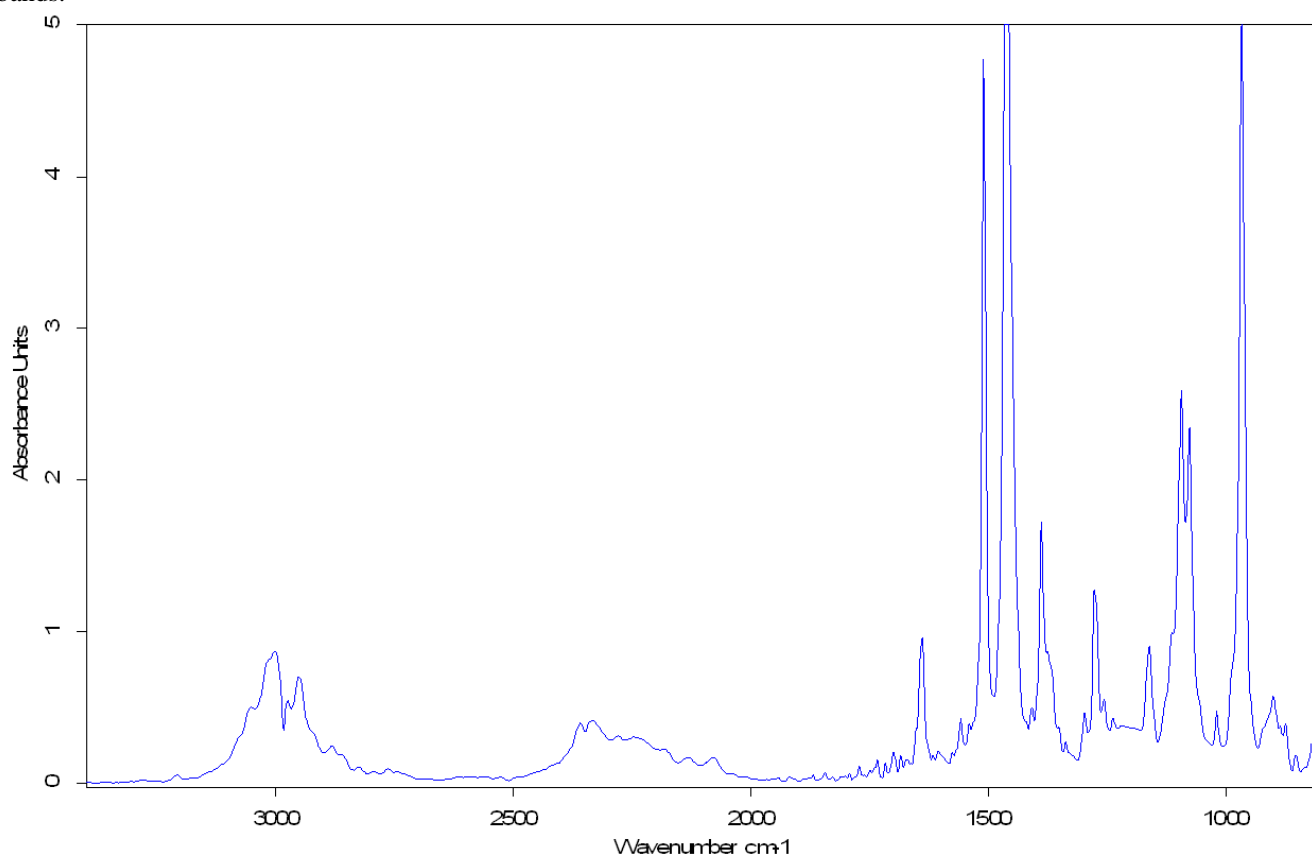


**Figure S30.** Absorption IR spectrum of **NHHB** solvated in  $\text{C}_2\text{H}_2\text{Cl}_4$  at 300 K. The spectrum of the solvent has been subtracted and the region from  $1220 - 1180 \text{ cm}^{-1}$  has been replaced by a straight line due to very strong solvent absorption bands.

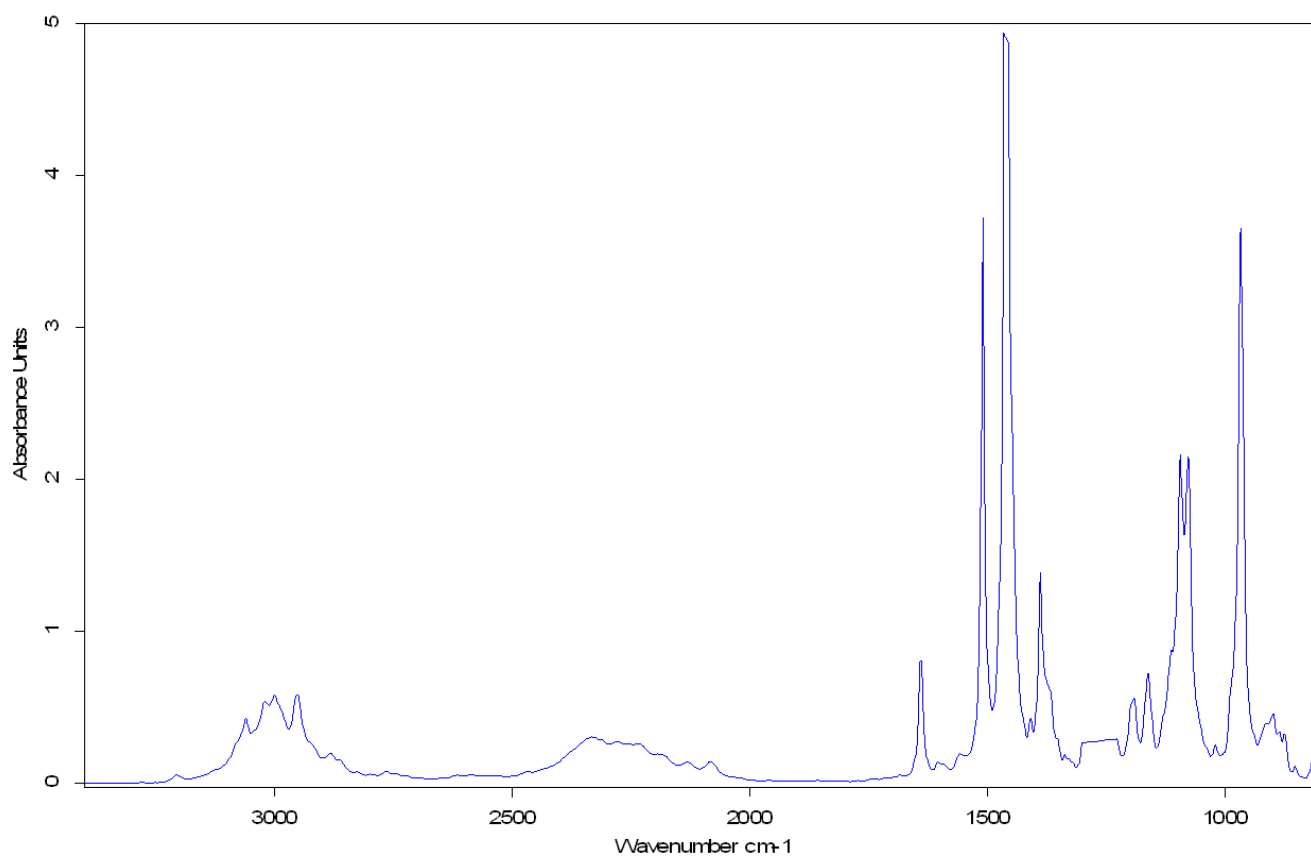


**Figure S31.** Absorption IR spectrum of **NHHB** solvated in  $\text{CH}_2\text{Cl}_2$  at 300 K. The spectrum of the solvent has been subtracted and the region from  $1300 - 1220 \text{ cm}^{-1}$  has been replaced by a straight line due to very strong solvent absorption bands.

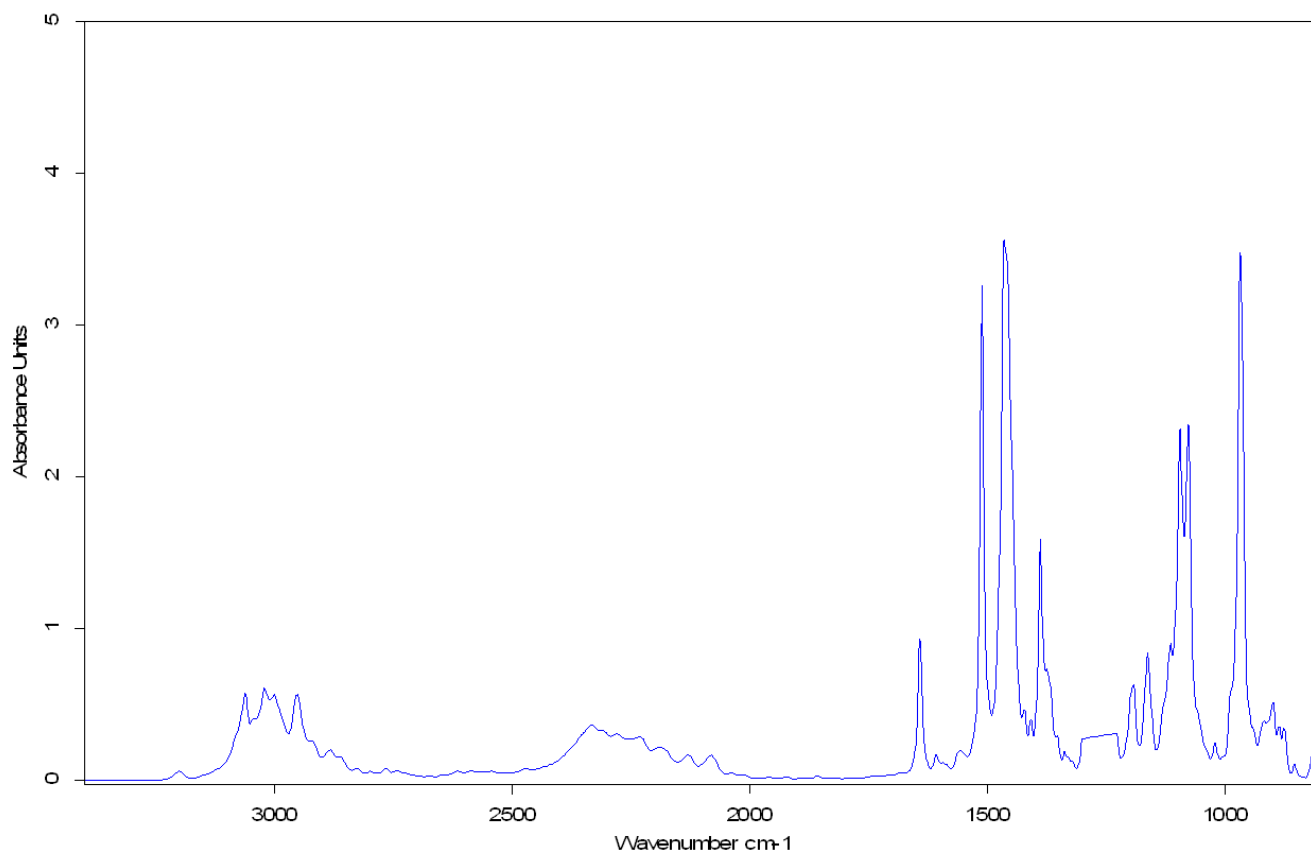


**Figure S32.** Absorption IR spectrum of **NHHB** solvated in  $\text{CH}_2\text{Cl}_2$  at 240 K. The spectrum of the solvent has been subtracted and the region from  $1300 - 1220 \text{ cm}^{-1}$  has been replaced by a straight line due to very strong solvent absorption bands.

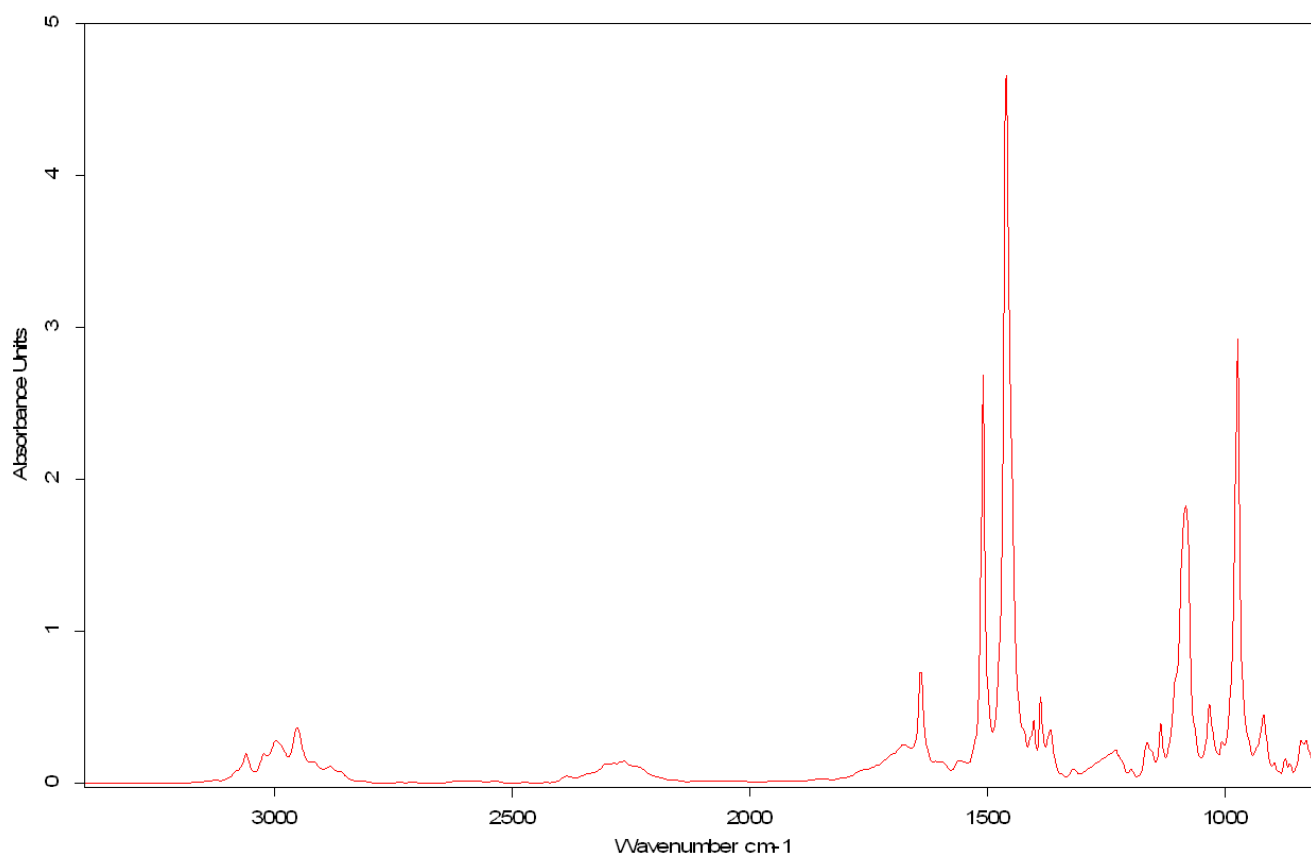


**Figure S33.** Absorption IR spectrum of **NDDB** solvated in  $\text{CH}_2\text{Cl}_2$  at 300 K. The spectrum of the solvent has been subtracted and the region from  $1300 - 1220 \text{ cm}^{-1}$  has been replaced by a straight line due to very strong solvent absorption bands.

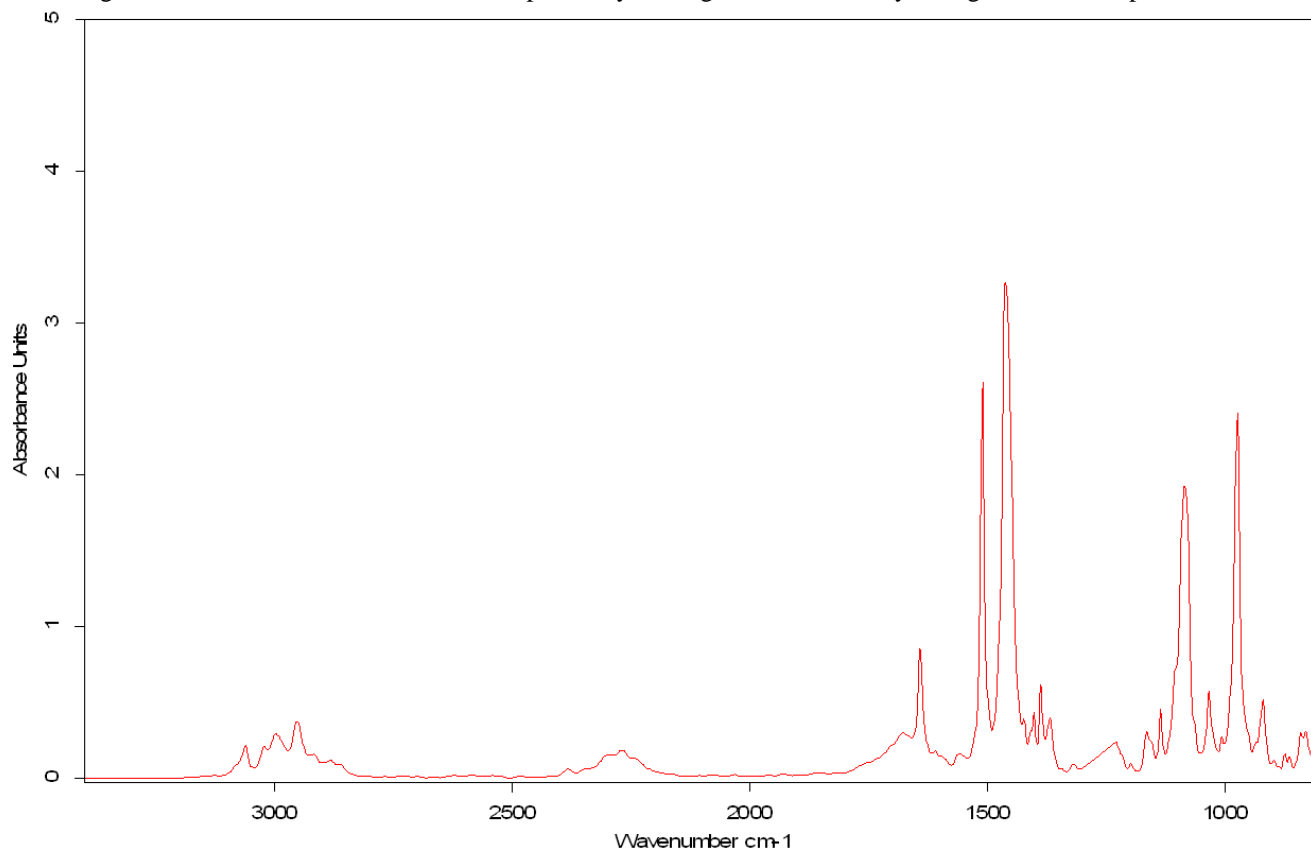


**Figure S34.** Absorption IR spectrum of **NDDB** solvated in  $\text{CH}_2\text{Cl}_2$  at 240 K. The spectrum of the solvent has been subtracted and the region from  $1300 - 1220 \text{ cm}^{-1}$  has been replaced by a straight line due to very strong solvent absorption bands.

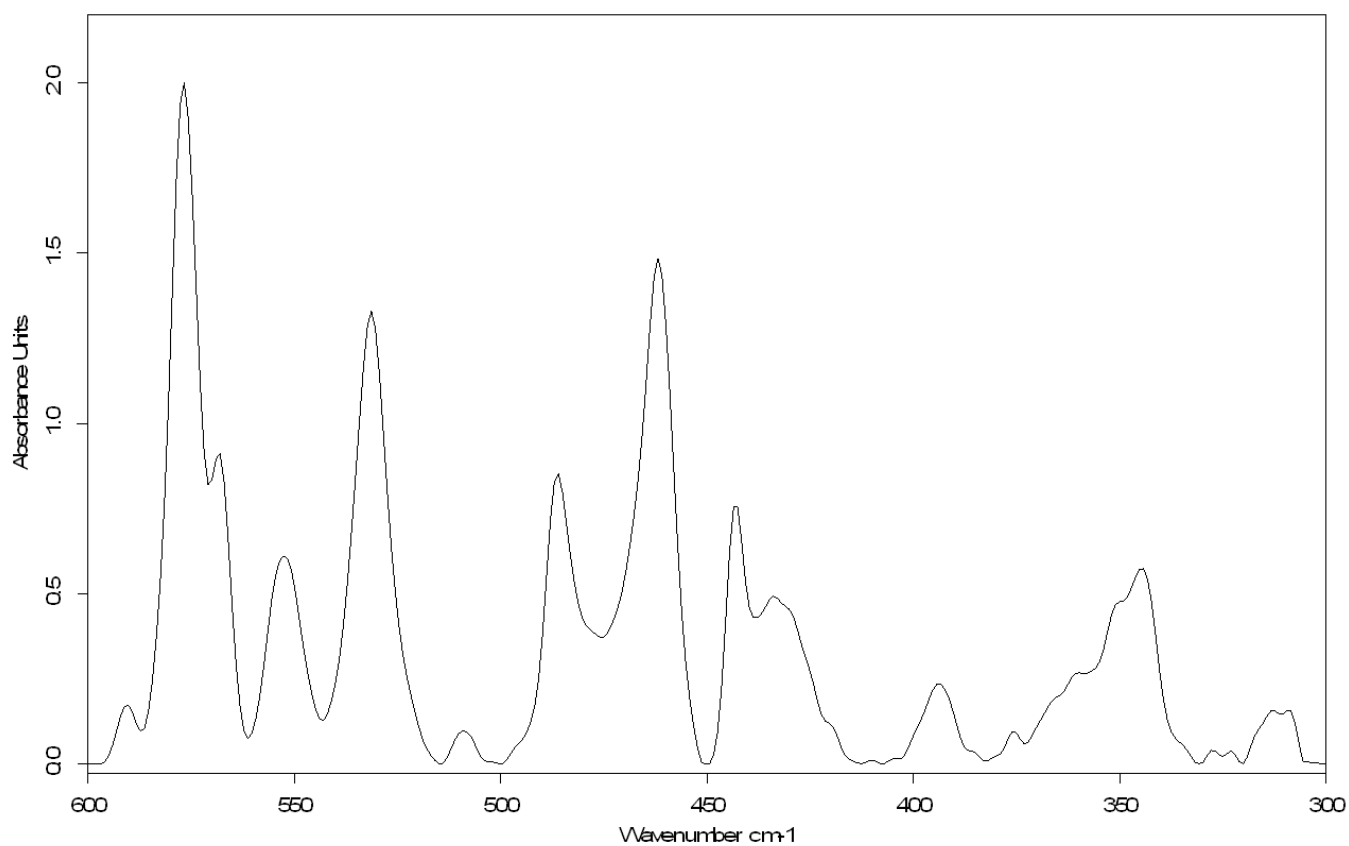


**Figure S35.** Absorption low wavenumber MIR spectrum of **NB** solvated in  $\text{CH}_2\text{Cl}_2$  at 300 K. The spectrum of the solvent has been subtracted.

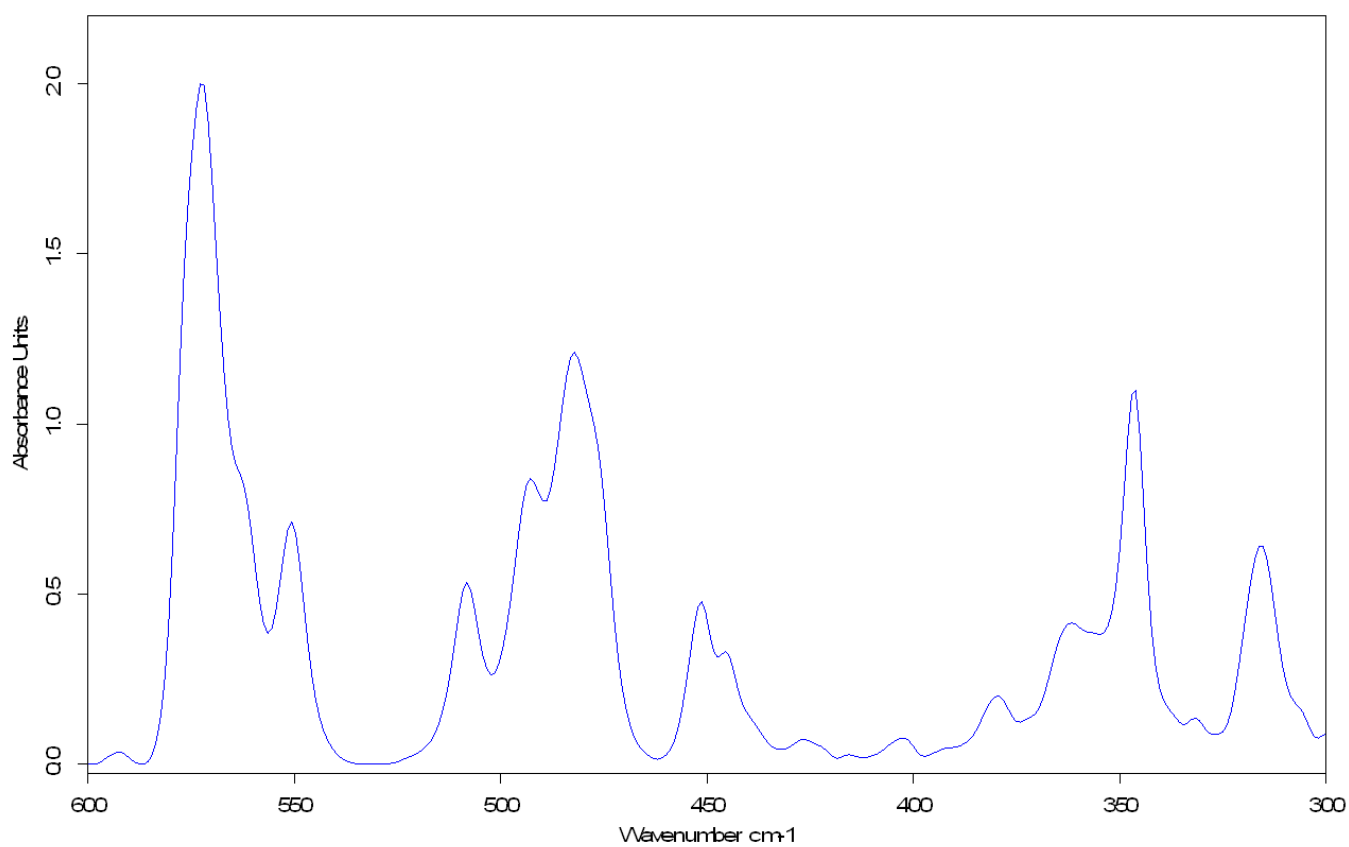


**Figure S36.** Absorption low wavenumber MIR spectrum of **NHHB** solvated in  $\text{C}_6\text{H}_6$  at 350 K. The spectrum of the solvent has been subtracted.

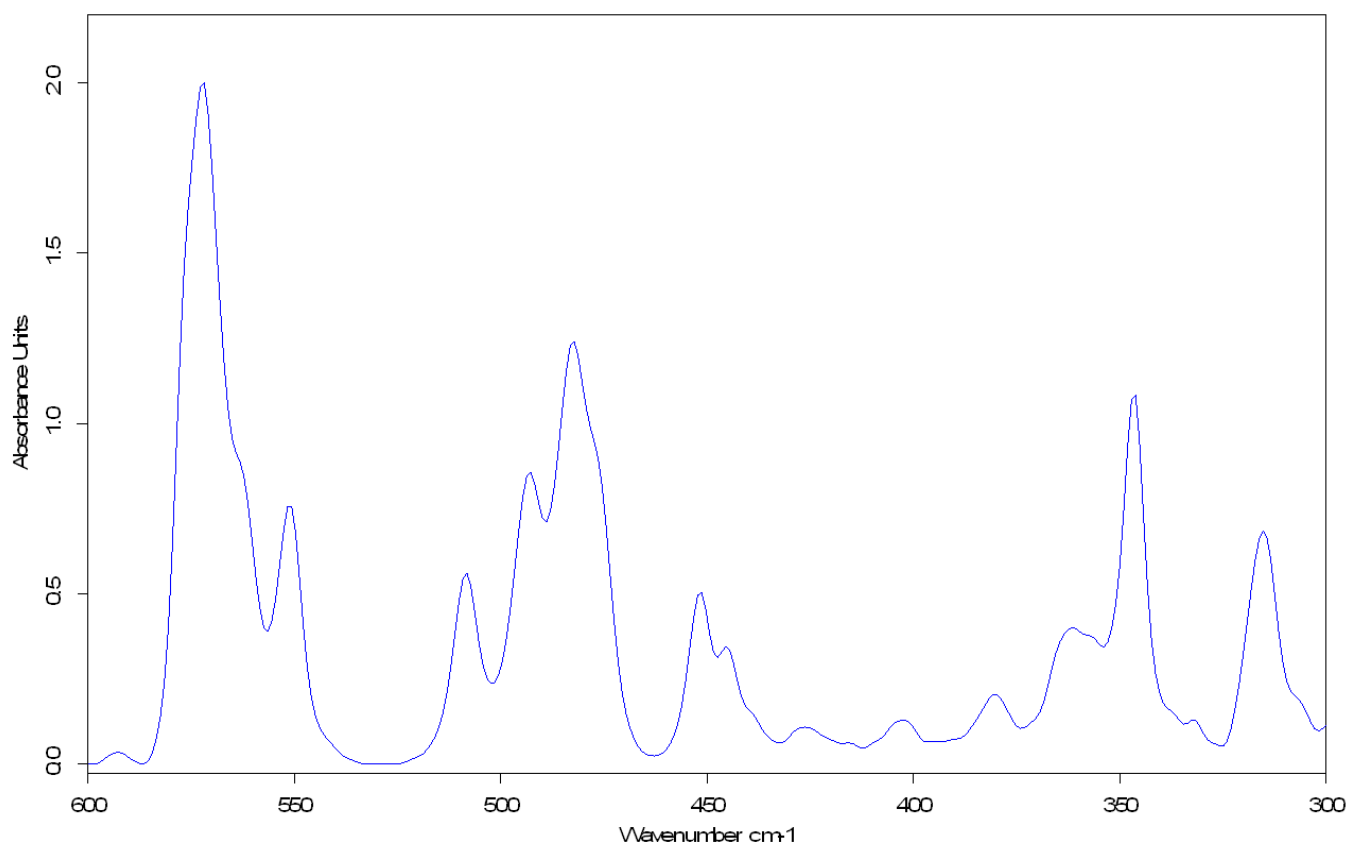


**Figure S37.** Absorption low wavenumber MIR spectrum of **NHHB** solvated in C<sub>6</sub>H<sub>6</sub> at 300 K. The spectrum of the solvent has been subtracted.

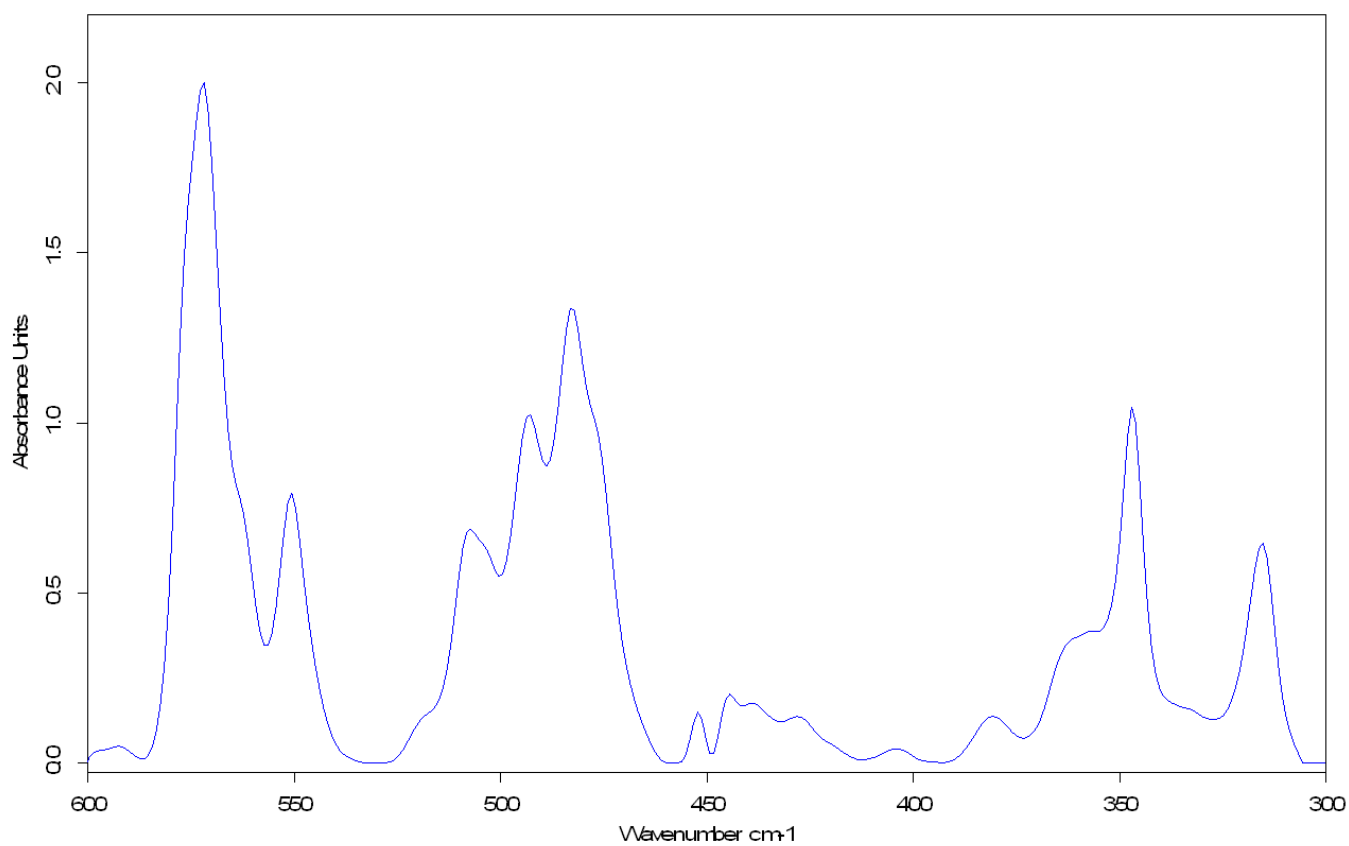


**Figure S38.** Absorption low wavenumber MIR spectrum of **NHHB** solvated in CH<sub>2</sub>Cl<sub>2</sub> at 300 K. The spectrum of the solvent has been subtracted.

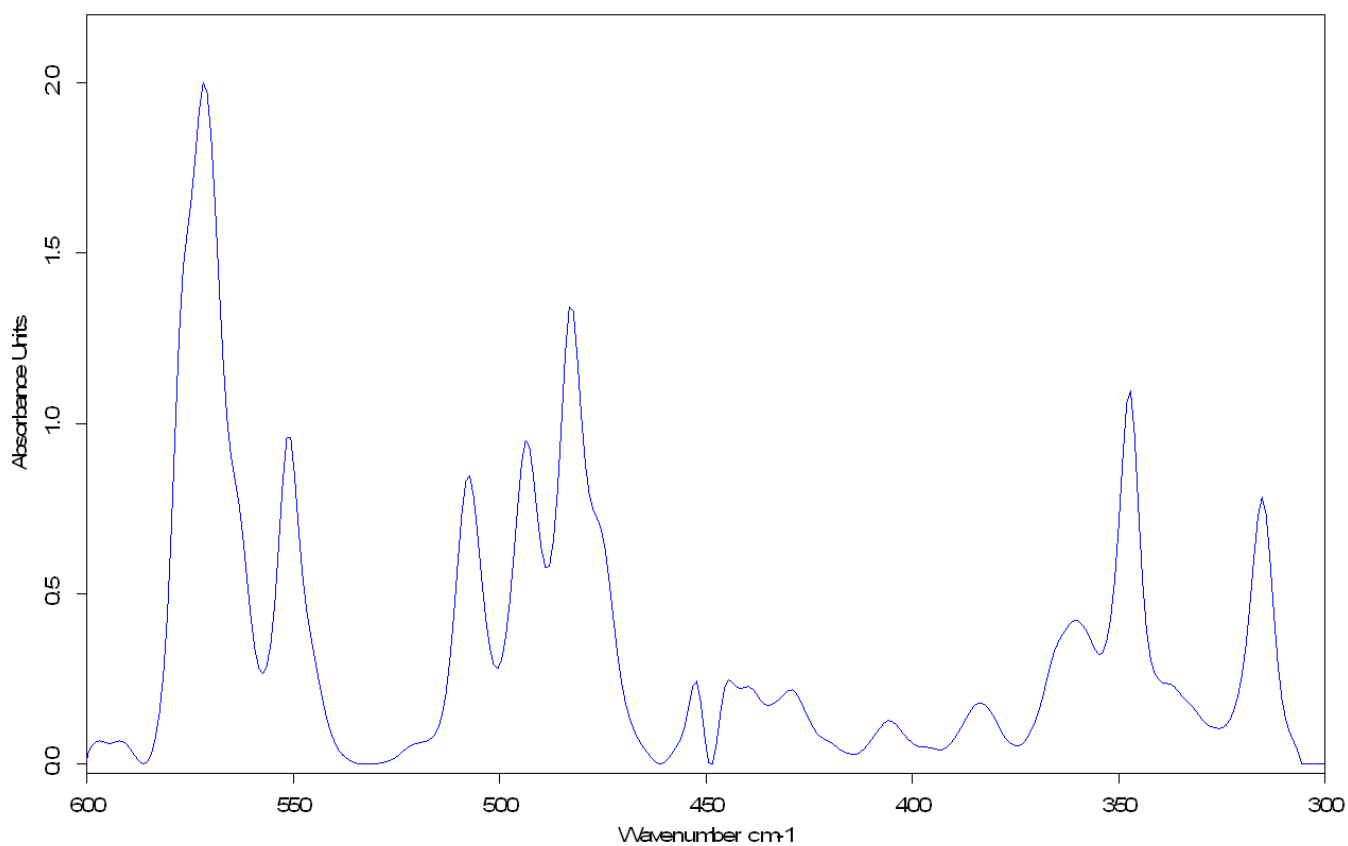


**Figure S39.** Absorption low wavenumber MIR spectrum of **NHHB** solvated in  $\text{CH}_2\text{Cl}_2$  at 200 K. The spectrum of the solvent has been subtracted.

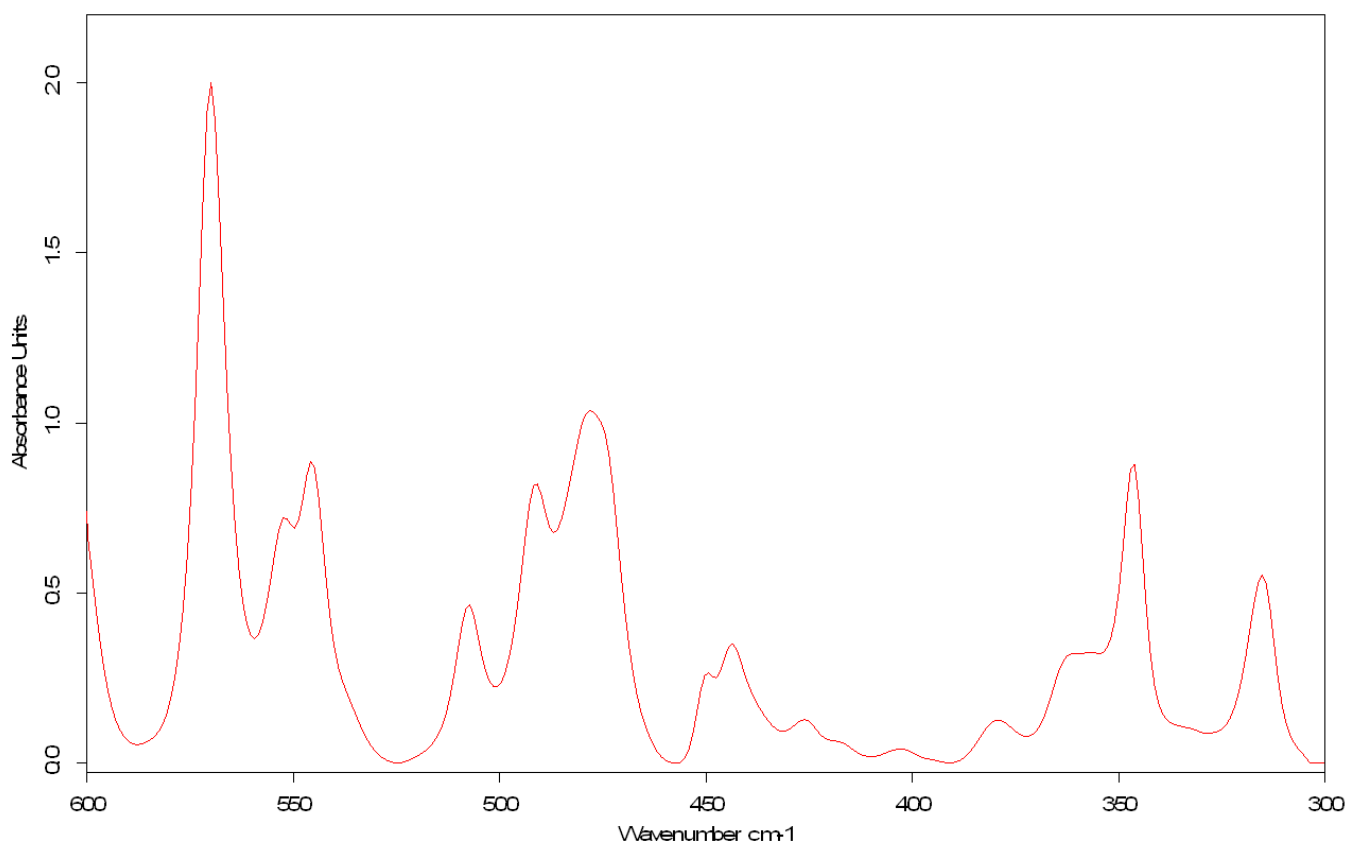


**Figure S40.** Absorption low wavenumber MIR spectrum of **NDDb** solvated in  $\text{CH}_2\text{Cl}_2$  at 300 K. The spectrum of the solvent has been subtracted.

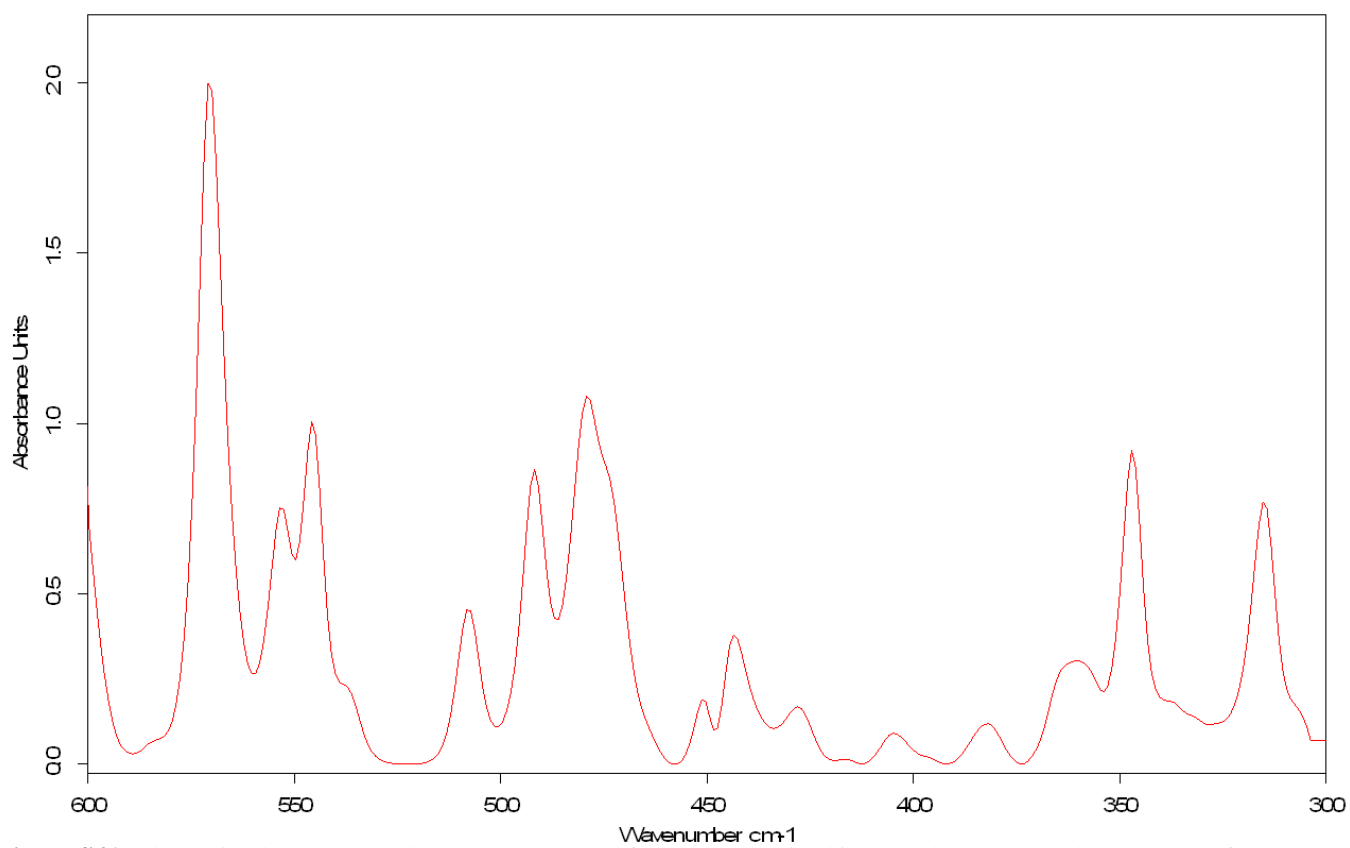


**Figure S41.** Absorption low wavenumber MIR spectrum of **NDDB** solvated in  $\text{CH}_2\text{Cl}_2$  at 200 K. The spectrum of the solvent has been subtracted.



## HRESI-TOF mass spectra

HRESI-TOF mass spectra are widely used to characterize organic compounds. In order to see whether the zwitterions of the type **NXYB** can really be detected as synthesized by this method the different H/D-isomers were analyzed. As expected HRESI-TOF MS measurements of **NHHB**, **NDDB**, **NHDB** and **NDHB** resulted in spectra with the highest mass peak corresponding to structures in which the positively charged hydron on the nitrogen is lost (Figure S42).

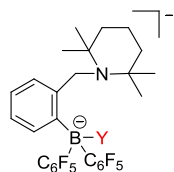


**Figure S42.** Molecular structure of the anions detected by HRESI<sup>−</sup>-TOF MS measurements of **NHHB** (Y = H), **NDDB** (Y = D), **NHDB** (Y = D) and **NDHB** (Y = H).

The fact that exactly this hydron is lost can be seen, because the recorded spectra of **NHHB** and **NDHB** are essentially the same, and this is also true for the spectra of **NDDB** and **NHDB**. Each pair of compounds only differs in the substitution of H<sup>+</sup> or D<sup>+</sup> on the N-atom. It does make sense that exactly these hydrons are lost during ESI<sup>−</sup> measurements, because these are by far the most acidic ones within each molecule.

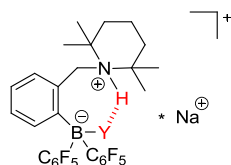


**Figure S43.** Molecular structure of the cationic Na-complexes detected by HRESI<sup>+</sup>-TOF MS measurements of acrylonitrile solutions of **NHHB** (Y = H), **NDDB** (Y = D), **NHDB** (Y = D) and **NDHB** (Y = H).

The recorded HRESI<sup>+</sup>-TOF mass spectra of **NHHB** and **NHDB** showed nicely the cationic sodium complexes of the intact molecules (Figure S43). During measurements of **NDDB** and **NDHB** acrylonitrile solutions ( $c = 10^{-6}$  mol/L) the acidic deuteriums positioned on the N-atoms were exchanged quantitatively with protons. Because protons are ubiquitous under these conditions (for example from water traces or glass walls) this H-D exchange could not be suppressed. Therefore the originally employed zwitterion of the type **NXYB** cannot be detected by this analysis method, but only the H<sup>+</sup>-exchanged isomer.

**$^1\text{H}$ - $T_1$  relaxation measurement data**

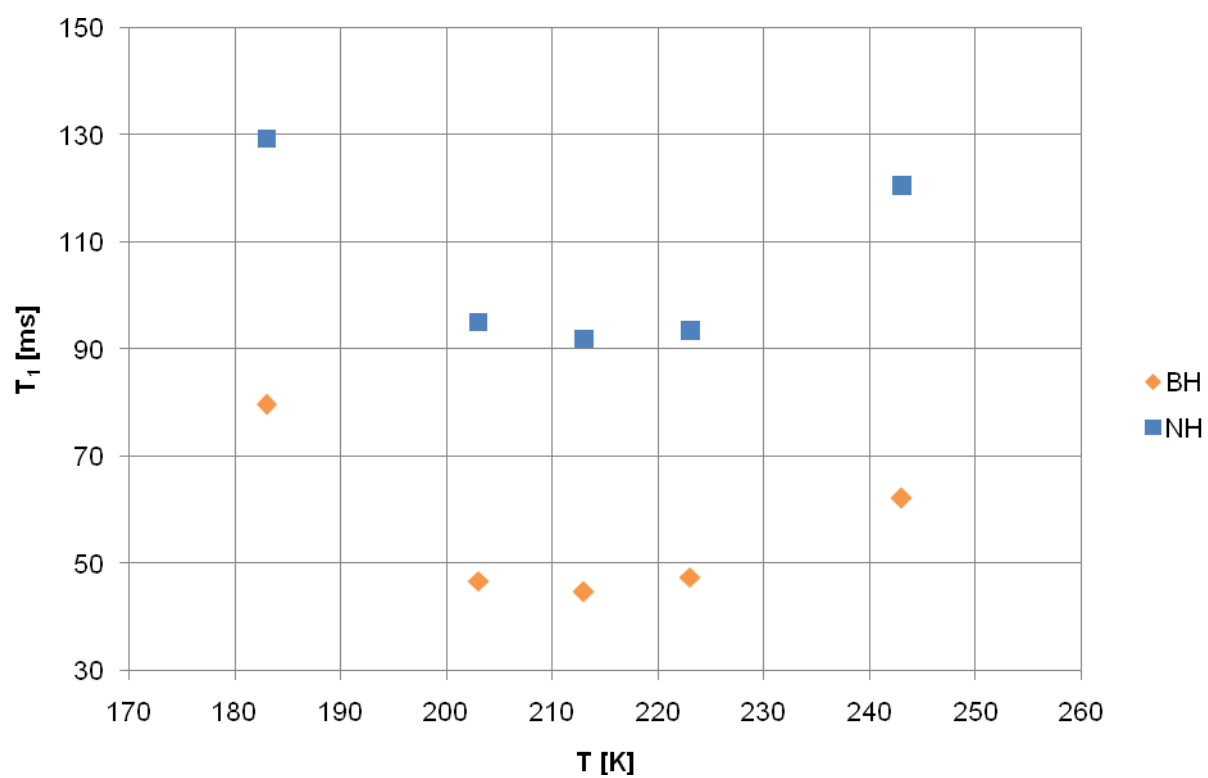


**Figure S44.** Plot of  $^1\text{H}$ - $T_1$  measurements of BH and NH as a function of temperature to determine  $T_1(\text{min})$ .

The relaxation rates  $1/T_1$  of the hydrons H1 and H8 via dipole-dipole mechanism can be described by Equations (1) and (2):

$$1/T_1(\text{H1}) = 1/T_1(\text{H1} \cdots \text{H8}) + 1/T_1(\text{H1} \cdots \text{H14a}) + 1/T_1(\text{H1} \cdots \text{H17a}) + 1/T_1(\text{H1} \cdots \text{B1}) + 1/T_1(\text{H1} \cdots \text{N8}) + 1/T_1(\text{H1} \cdots \text{F19}) + 1/T_1(\text{H1} \cdots \text{F23}) + 1/T_1(\text{H1} \cdots \text{F25}) + 1/T_1(\text{H1} \cdots \text{F29}) \quad (1)$$

$$1/T_1(\text{H8}) = 1/T_1(\text{H1} \cdots \text{H8}) + 1/T_1(\text{H8} \cdots \text{H7a}) + 1/T_1(\text{H1} \cdots \text{H10a}) + 1/T_1(\text{H1} \cdots \text{H12b}) + 1/T_1(\text{H1} \cdots \text{H14a}) + 1/T_1(\text{H1} \cdots \text{H17a}) + 1/T_1(\text{H1} \cdots \text{B1}) + 1/T_1(\text{H1} \cdots \text{N8}) + 1/T_1(\text{H1} \cdots \text{F19}) + 1/T_1(\text{H1} \cdots \text{F29}) \quad (2)$$

In Equations (1) and (2) homonuclear proton-proton and proton-heteronucleus dipole-dipole interactions can be written according to Equations (3) and (4):<sup>6</sup>

$$1/T_1(\text{H} \cdots \text{H}) = 3\gamma_{\text{H}}^4 \hbar^2 (r_{\text{HH}})^{-6} / 10 \times [ \tau_c / (1 + \omega_{\text{H}}^2 \tau_c^2) + 4\tau_c / (1 + 4\omega_{\text{H}}^2 \tau_c^2) ] \quad (3)$$

$$1/T_1(\text{H} \cdots \text{X}) = 2\gamma_{\text{H}}^2 \gamma_{\text{X}}^2 \hbar^2 I(I+1) (r_{\text{HX}})^{-6} / 15 \times [ 3\tau_c / (1 + \omega_{\text{H}}^2 \tau_c^2) + 6\tau_c / (1 + (\omega_{\text{H}} + \omega_{\text{X}})^2 \tau_c^2) + \tau_c / (1 + (\omega_{\text{H}} - \omega_{\text{X}})^2 \tau_c^2) ] \quad (4)$$

In Equations (3) and (4) the symbols  $\gamma$ ,  $\hbar$ ,  $I$  and  $\omega$  represent gyromagnetic ratio, Planck's constant/ $2\pi$ , nuclear spin, and Larmor frequency, respectively. To fit the theoretical  $T_1$ -curve to the measured  $T_1$ -values as a function of temperature, the correlation time in Equations (3) and (4) is replaced by  $\tau_c = \tau_0 \exp(E_a/RT)$ , where  $\tau_0$  is correlation constant,  $E_a$  is activation energy for molecular rotation,  $R$  is universal gas constant and  $T$  is temperature. In the  $T_1(\text{min})$  approach to calculate  $r_{\text{H1-H8}}$ , the correlation time at temperature resulting in  $T_1(\text{min})$ -value was calculated from:<sup>7</sup>

$$\tau_c = 0.6158/\omega \quad (5)$$

Equations (1) and (2) were modified to take the natural abundances of the interacting nuclei into account.

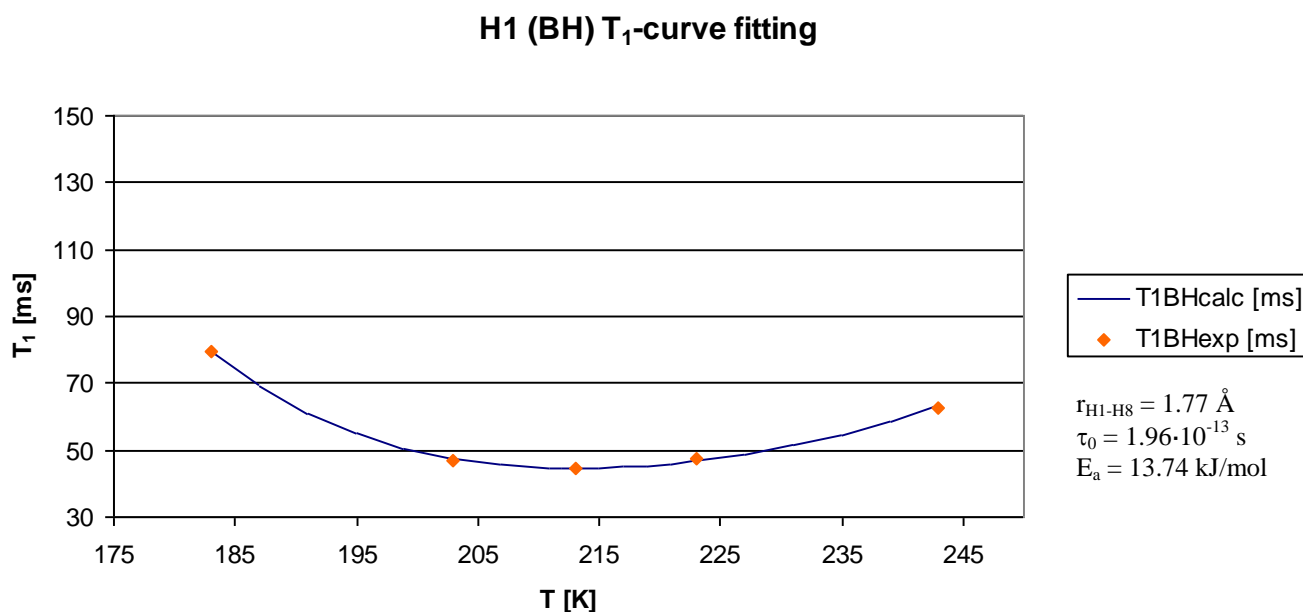


**Figure S45.** 300 MHz  $T_1$ -values of H1 (BH) as a function of temperature and fitted  $T_1$ -curve. The calculated  $T_1$ -curve includes contributions from nuclei H8, H14a, H17a, B1, N8, F19, F23, F25 and F29 (see Table S1). Natural abundances of  $^1\text{H}$ ,  $^2\text{H}$ ,  $^{10}\text{B}$ ,  $^{11}\text{B}$ ,  $^{14}\text{N}$  and  $^{15}\text{N}$  were taken into account. The distances to nuclei other than H8 were obtained from the neutron diffraction study. The fitted parameters were H1  $\cdots$  H8 distance ( $r_{\text{H1-H8}}$ ), correlation time constant ( $\tau_0$ ) and activation energy for molecular reorientation ( $E_a$ ). Correlation time  $\tau_c$  at  $T_1(\text{min})$  temperature 213 K was  $4.59 \cdot 10^{-10} \text{ s}$  (calculated from  $\tau_0$  and  $E_a$ ).

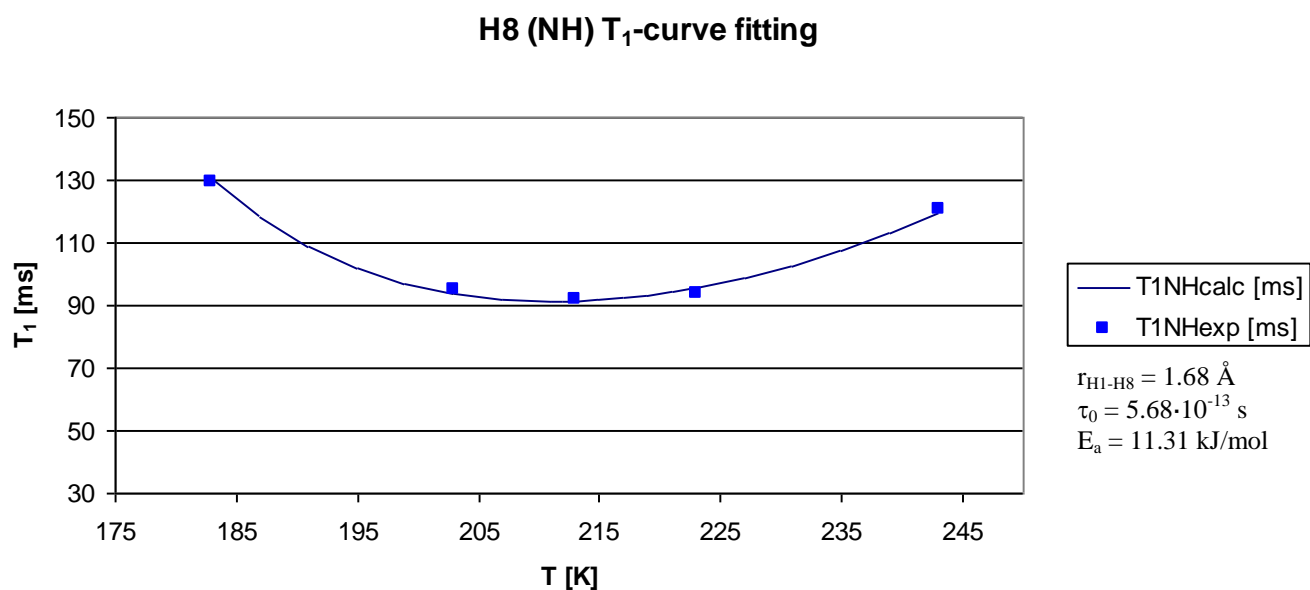


**Figure S46.** 300 MHz T<sub>1</sub>-values of H8 (NH) at 300 MHz as a function of temperature and fitted T<sub>1</sub>-curve. The calculated T<sub>1</sub>-curve includes contributions from nuclei H1, H7a, H10a, H12b, H14a, H17a, B1, N8, F19, and F29 (see Table S1). Natural abundances of <sup>1</sup>H, <sup>2</sup>H, <sup>10</sup>B, <sup>11</sup>B, <sup>14</sup>N and <sup>15</sup>N were taken into account. The distances to nuclei other than H1 were obtained from the neutron diffraction study. The fitted parameters were H1···H8 distance ( $r_{\text{H1-H8}}$ ), correlation time constant ( $\tau_0$ ) and activation energy for molecular reorientation ( $E_a$ ). Correlation time  $\tau_c$  at T<sub>1</sub>(min) temperature 213 K was  $3.37 \cdot 10^{-10}$  s (calculated from  $\tau_0$  and  $E_a$ ).

**Table S1.** Calculation of the interatomic H-H distance of **NHHB** in a CD<sub>2</sub>Cl<sub>2</sub> solution at 213 K.

X	$r_{H1-X}$ [pm] <sup>a</sup>	$R_{H1-X}$ [1/s]	Y	$r_{H8-Y}$ [pm] <sup>a</sup>	$R_{H8-Y}$ [1/s]
B1	123,5	15,7047	N8	103,3	1,5143
N8	264,6	0,0054	B1	256,6	0,1952
F19	258,0	0,3153	F19	369,9	0,0363
F25	398,2	0,0233	F29	372,8	0,0346
F29	262,1	0,2869	H7a	237,4	0,7213
H17a	244,3	0,6074	H14a	225,0	0,9952
H14a	269,5	0,3370	H12b	263,7	0,3840
F23	401,2	0,0223	H10a	260,0	0,4180
			H17a	226,6	0,9538
$R_{\text{sum H1-X}}$ [1/s]:		17,3023	$R_{\text{sum H8-Y}}$ [1/s]:		5,2527
$T_1(\text{min})_{H1}$ [s] <sup>b</sup> :		0,0448	$T_1(\text{min})_{H8}$ [s] <sup>b</sup> :		0,0921
$R_{\text{obs H1}}$ [1/s]:		22,3214	$R_{\text{obs H8}}$ [1/s]:		10,8578
$R_{\text{obs H1}} - R_{\text{sum H1-X}}$ [1/s]:		5,0191	$R_{\text{obs H8}} - R_{\text{sum H8-Y}}$ [1/s]:		5,6050
$r_{H1-H8}$ [pm]:		171,8	$r_{H8-H1}$ [pm]:		168,7
$r_{H-H}$ [pm] <sup>c</sup> :		170			

<sup>a</sup> determined by single crystal neutron scattering; <sup>b</sup> determined by <sup>1</sup>H- $T_1$  relaxation measurements in a CD<sub>2</sub>Cl<sub>2</sub> solution at 213 K; <sup>c</sup> mean value of  $r_{H1-H8}$  and  $r_{H8-H1}$ .

### Selective 1D NOE and 2D NOESY data for $r_{\text{H1-H8}}$ determination

Selective 1D NOE measurements were conducted using 1D DPGSE-NOE pulse sequence utilizing two *gradient-sel. 180°-gradient-elements*:<sup>8</sup>

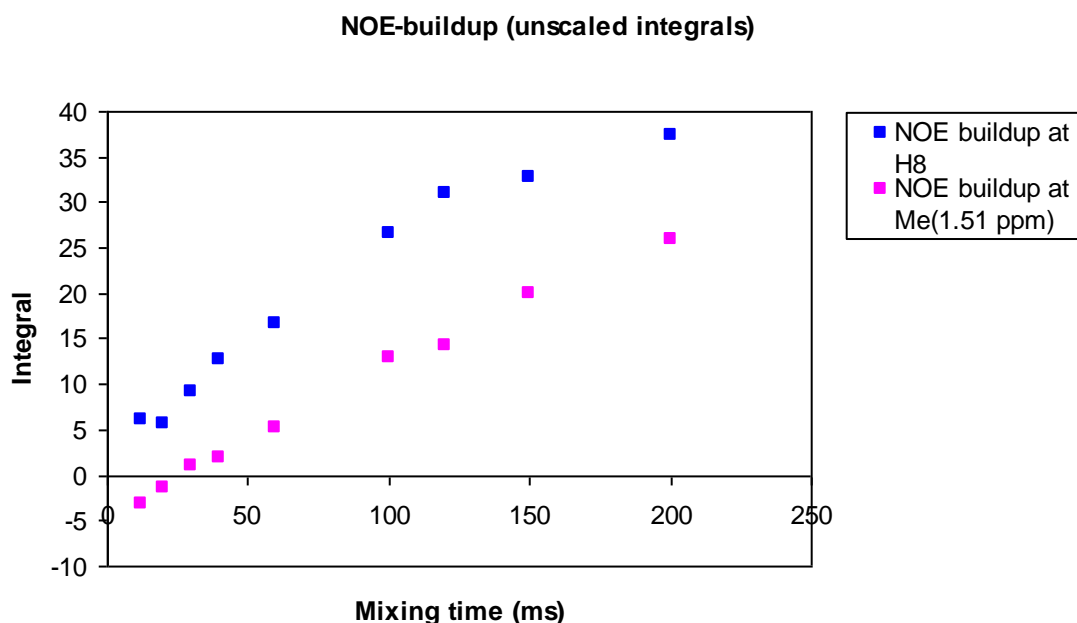
Two sets of experiments were recorded, each with 9 mixing times (12, 20, 30, 40, 60, 100, 120, 150, 200 ms):

- Selective-180° pulses applied at resonance H1 (*H1-selective 1D NOE*). The development of NOE signal at H8 (NH) frequency monitored
- Selective pulses applied at target methyl resonance 1.12 ppm (*Me(1.12 ppm)-selective 1D NOE*). The development of the NOE-signal at the methyl frequency 1.51 ppm was monitored.

The effective distance between the protons in the methyl groups ( $\text{Me}_{14}\cdots\text{Me}_{15}$  and  $\text{Me}_{17}\cdots\text{Me}_{16}$ ) was calculated from neutron diffraction coordinates using the  $r^{-3}$  averaging method.<sup>9,10</sup> This distance, 3.16 Å, was used as a reference.

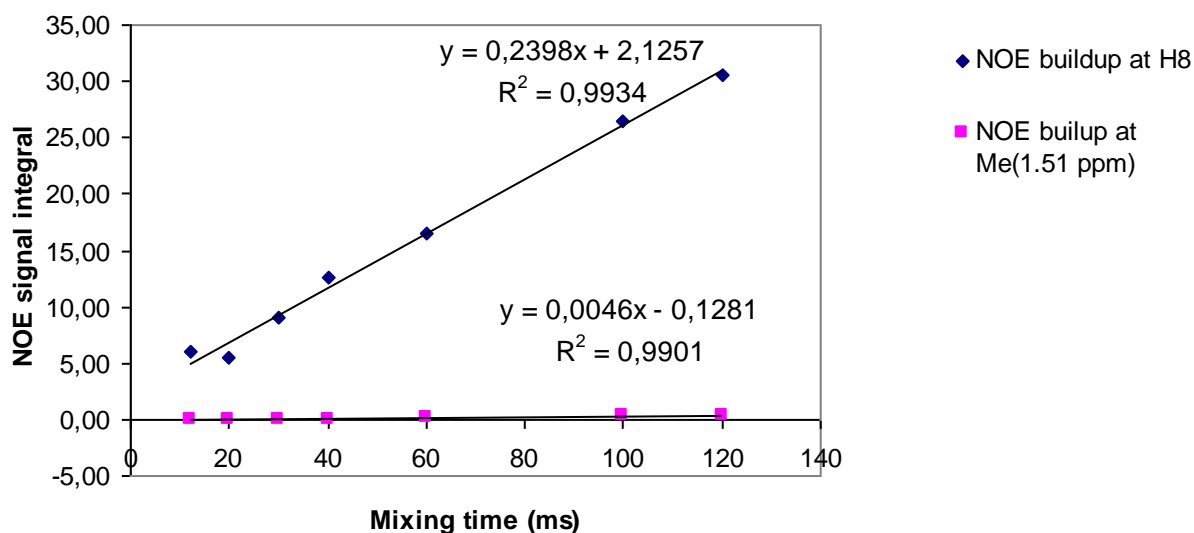
NOE-signal intensities were scaled according to  $n_A n_B$ , where  $n_A$  and  $n_B$  are the number of chemically equivalent spins contributing to the observed NOE signal i.e. H1 and Me(1.51 ppm) integrals were divided by 1 and 36 (6 protons at 1.12 ppm and 6 protons at 1.51 ppm), respectively.<sup>10,11</sup> Also, the NOE-signal intensity data was corrected for different degree of inversion due to selective pulse and relaxation effects during the two *gradient-sel. 180°-gradient* elements.<sup>12</sup> This was determined by comparing the H1-integral in *H1-selective 1D NOE* to Me(1.12 ppm) integral from *Me(1.12 ppm)-selective 1D NOE*, both recorded using the shortest mixing time of 12 ms. The *H1-selective 1D NOE* data had to be multiplied by factor of 0.99 to retain 1:6 integral ratio for H1 and Me(1.12 ppm) observed in normal  $^1\text{H}$  spectrum.

Figure S44 shows the unscaled NOE intensities at H8 and Me(1.51 ppm) as a function of mixing time. Figure S45 presents the linear regions of the appropriately scaled NOE intensity data. Figure S46 shows the expansion of Figure S45 to display Me(1.51 ppm) buildup data. The cross relaxation rates (NOE buildup rates) were determined by linear regression, where the slope represents buildup rate (0.2398  $\text{ms}^{-1}$  for NOE signal at H8 and 0.0046  $\text{ms}^{-1}$  for NOE signal at Me(1.51 ppm)). There was no attempt to force the linear regression line to go through zero since there is a clear indication in NOE buildup curves of some baseline offset in both NOE-intensities. The distance  $r_{\text{H1-H8}}$  was calculated using Me-Me reference distance (3.16 Å) and cross relaxation rates. This resulted in a value of 1.63 Å.



**Figure S47.** The unscaled NOE intensities (integrals) at frequencies H8 (from *H1-selective 1D NOE*) and Me(1.51 ppm) (*Me(1.12 ppm)-selective 1D NOE*) as a function of mixing time.

### NOE buildup at H8 and Me (1.51 ppm), scaled integrals



**Figure S48.** The initial linear regions of NOE signal buildup at H8 and Me(1.51 ppm). The intensities are scaled for a different number of protons and degree of inversion of the selective pulse. The cross relaxation rates (NOE buildup rates) are represented by the slope obtained from linear regression.

### NOE buildup at Me (1.51 ppm), scaled integrals

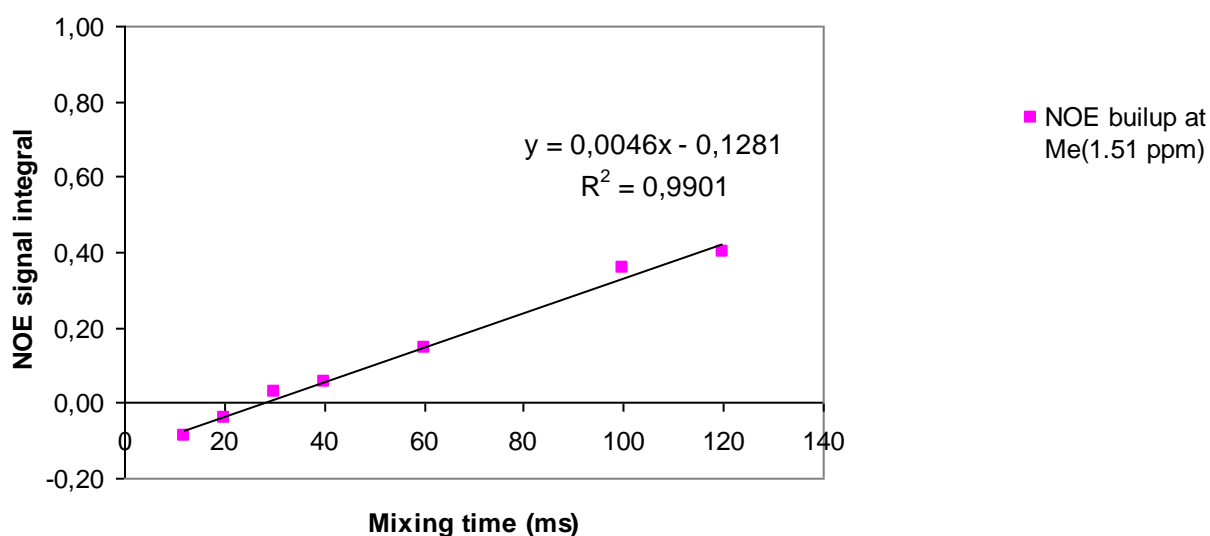


**Figure S49.** Vertical expansion of Figure 45 to show the initial linear region of NOE-buildup at Me(1.51 ppm). The intensities are scaled for different number of protons and degree of inversion of the selective pulse. The cross relaxation rate (NOE buildup rate) is represented by the slope obtained from linear regression.

In addition a series of 2D NOESY experiments was performed to verify the result obtained with 1D DPGSE-NOE. Nine 2D spectra were recorded using mixing times of 25, 50, 2x100, 125, 150, 200, 250, 300, 400, 600 and 700 ms. Spectral width was 5497.53 Hz in both dimensions. Relaxation delay was 2.5 s and acquisition time was 0.2 s. Spectra were recorded using 16 transients and 200 increments. The number of acquired complex data points was 1100. Receiver gain was kept constant in NOESY measurements. Time domain data was apodized using squared cosine function and zero-filled to 2048 complex points in both dimensions, prior to Fourier transformation. Polynomial baseline correction (5<sup>th</sup> order) was applied in  $f_2$ -dimension before 2D integration. Correlation peak volumes were corrected for number of protons as described for 1D NOE experiments.

NOE-buildup rates were extracted using linear regression. Again, there was no attempt to force the regression line to go through zero. Two correlation peak volumes per proton-pair (H1-H8 and Me-Me) were measured (correlation peaks on both sides of the diagonal). According to NOE-buildup rates and reference distance of 3.16 Å between methyls (Me<sub>14</sub>···Me<sub>15</sub> and Me<sub>17</sub>···Me<sub>16</sub>), the H1···H8 distance was calculated using correlation peaks both above and below the diagonal. The average value was then calculated resulting in an H1···H8 distance of 1.65 Å (above- and below-diagonal H1-H8 and Me-Me peaks resulted in H1···H8 distances of 1.56 Å and 1.74 Å, respectively). Figures S50 and S51 show the above- and below-diagonal correlation peak volumes for H1-H8 and Me-Me. Please note, that it is easier to control the baseline quality as well as apply baseline correction in 1D NOE experiments. In 2D NOESY integration is more cumbersome and the obtained data quality depends on the success of the 2D baseline correction as well as overlap of possible 2D artifacts (like t<sub>1</sub>-noise) with correlation peaks. This leads to assumption that the distance obtained with selective 1D NOE could be considered more reliable in this study.

The selective 1D NOE and 2D NOESY experiments suggest a short H1-H8 distance around 1.65 Å at RT.

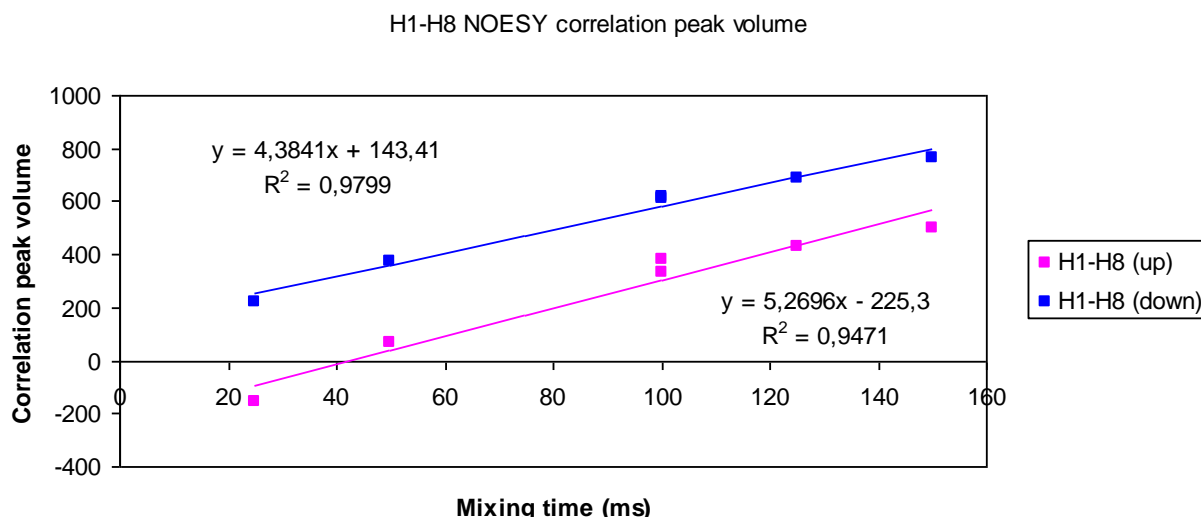


**Figure S50.** Scaled H1-H8 NOESY correlation peak at 7.77 ppm (f<sub>2</sub>), 3.76 ppm (f<sub>1</sub>) volume as a function of mixing time. H1-H8 (up) and H1-H8 (down) refer to volumes of above-diagonal and below-diagonal correlation peaks, respectively. Also linear regression line is shown.

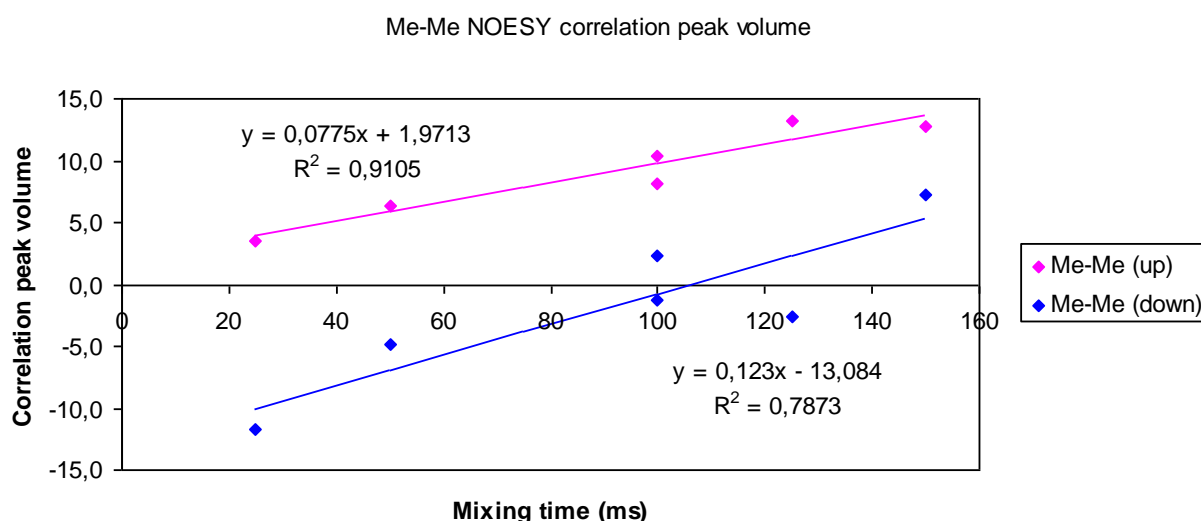


**Figure S51.** Scaled Me-Me NOESY correlation peak volume as a function of mixing time at 1.51 ppm (f<sub>2</sub>), 1.12 ppm (f<sub>1</sub>). Me-Me (up) and Me-Me (down) refer to volumes of above-diagonal and below-diagonal correlation peaks, respectively. Also linear regression line is shown.



**Table S2.** Crystal data and details of the structure determination for: **NHHB** P-1 R = 0.06

Crystal Data			
Formula	C28 H26 B F10 N, 0.5(C6 D6)		
Formula Weight [g/mol]	619.37		
Crystal System	Triclinic		
Space group	P-1	(No. 2)	
a, b, c [Å]	10.587(10)	12.183(10)	12.52(1)
α, β, γ[deg]	86.77(5)	70.73(5)	64.83(5)
V [Å³]	1373(2)		
Z	2		
ρ(calc) [g/cm³]	1.498		
μ(neut) [1/mm ]	0.07		
F(000)	400		
Crystal Size [mm]	fragment, approx. 2.00 x 2.00 x 2.00		
Data Collection			
Temperature (K)	10 K		
Radiation [Å]	neutrons	1.03000	
Theta Min-Max [deg]	0.0, 55.0		
Tot. Data	9015		
Observed data [I > 2.5 σ(I)]	5332		
Refinement			
Nref, Npar	5332, 295		
R, wR2, S	0.0659, 0.0645, 1.42		
w = 1/σ²(F) + 0.0001F²			
Min. and Max. Resd. Dens. [barns/Å³]	1.56, -1.40		

**Table S3.** Final coordinates and equivalent isotropic displacement parameters of the non-hydrogen atoms.

Atom	x	y	z	U(iso) [Å <sup>2</sup> ]
F19	0.9138(3)	0.7588(3)	0.7121(2)	0.0090(5)
F20	0.9602(3)	0.9439(3)	0.6154(2)	0.0091(5)
F21	0.7465(3)	1.1235(3)	0.5500(2)	0.0056(5)
F22	0.4818(3)	1.1154(3)	0.5917(2)	0.0091(5)
F23	0.4295(3)	0.9363(3)	0.6945(2)	0.0078(5)
F25	0.3651(3)	0.6974(3)	0.8964(2)	0.0050(5)
F26	0.1896(3)	0.6584(3)	0.8081(2)	0.0089(5)
F27	0.2595(3)	0.6248(3)	0.5805(2)	0.0089(5)
F28	0.5133(3)	0.6335(3)	0.4389(2)	0.0056(5)
F29	0.6905(3)	0.6729(3)	0.5248(2)	0.0067(5)
N8	0.84169(18)	0.41953(16)	0.79382(13)	0.0033(3)
C1	0.6333(2)	0.7094(2)	0.89126(18)	0.0025(4)
C2	0.5894(3)	0.8164(2)	0.9579(2)	0.0053(4)
C3	0.5680(3)	0.8209(2)	1.0742(2)	0.0061(4)
C4	0.5905(3)	0.7158(2)	1.12842(19)	0.0040(4)
C5	0.6368(3)	0.6064(2)	1.06537(19)	0.0038(4)
C6	0.6588(2)	0.6026(2)	0.94903(18)	0.0021(4)
C7	0.6978(3)	0.4800(2)	0.89278(19)	0.0038(4)
C9	0.9854(2)	0.3859(2)	0.82417(18)	0.0024(4)
C10	1.1198(3)	0.3167(2)	0.71866(19)	0.0054(4)
C11	1.1173(3)	0.2072(2)	0.66764(19)	0.0056(4)
C12	0.9825(3)	0.2528(2)	0.63018(19)	0.0058(4)
C13	0.8352(2)	0.3175(2)	0.72819(18)	0.0020(4)
C14	0.7164(3)	0.3787(3)	0.6723(2)	0.0070(4)
C15	0.7989(3)	0.2268(3)	0.8065(2)	0.0066(4)
C16	0.9857(3)	0.3135(2)	0.9264(2)	0.0061(4)
C17	0.9939(3)	0.5041(2)	0.8473(2)	0.0057(4)
C18	0.6716(3)	0.8342(2)	0.70630(19)	0.0032(4)
C19	0.8041(3)	0.8444(2)	0.68418(19)	0.0044(4)
C20	0.8308(3)	0.9400(2)	0.63378(19)	0.0053(4)
C21	0.7219(3)	1.0321(2)	0.60055(19)	0.0039(4)
C22	0.5874(3)	1.0278(2)	0.62165(19)	0.0048(4)
C23	0.5650(3)	0.9306(2)	0.67511(19)	0.0041(4)
C24	0.5374(2)	0.6892(2)	0.71545(18)	0.0022(4)
C25	0.4071(3)	0.6840(2)	0.78201(18)	0.0035(4)
C26	0.3132(3)	0.6628(2)	0.73866(19)	0.0052(4)
C27	0.3474(3)	0.6469(2)	0.62287(19)	0.0045(4)
C28	0.4762(3)	0.6509(2)	0.55151(19)	0.0040(4)
C29	0.5666(3)	0.6715(2)	0.59836(18)	0.0034(4)
B1	0.6568(3)	0.7112(3)	0.7561(2)	0.0019(5)
*C1B	0.1050(6)	0.9640(4)	0.9190(4)	0.0077(5)
*C2B	0.0207(5)	0.9316(4)	0.8704(4)	0.0115(10)
*C3B	-0.1227(6)	0.9519(4)	0.9339(4)	0.0132(19)
*C4B	-0.1862(4)	1.0035(4)	1.0445(3)	0.0062(9)
*C5B	-0.1023(5)	1.0366(4)	1.0945(5)	0.0077(5)
*C6B	0.0387(5)	1.0160(5)	1.0307(4)	0.0103(9)

**Table S4.** Hydrogen atom positions and isotropic displacement parameters.

Atom	x	y	z	U(iso) [Å <sup>2</sup> ]
H1	0.7783(6)	0.6288(5)	0.7019(4)	0.0144(9)
H2	0.5712(7)	0.8995(6)	0.9186(5)	0.0225(11)
H3	0.5320(7)	0.9077(7)	1.1211(5)	0.0253(12)
H4	0.5721(6)	0.7179(6)	1.2190(5)	0.0212(11)
H5	0.6555(6)	0.5244(6)	1.1058(5)	0.0214(11)
H7A	0.6114(6)	0.4898(5)	0.8598(4)	0.0176(10)
H7B	0.6972(5)	0.4169(5)	0.9554(4)	0.0127(9)
H8	0.8396(5)	0.4862(5)	0.7388(4)	0.0124(9)
H10A	1.1276(6)	0.3782(6)	0.6545(4)	0.0185(10)
H10B	1.2182(7)	0.2891(6)	0.7434(5)	0.0220(11)
H11A	1.1172(6)	0.1387(6)	0.7287(5)	0.0221(11)
H11B	1.2185(6)	0.1633(6)	0.5938(5)	0.0198(10)
H12A	0.9746(6)	0.1787(6)	0.5908(5)	0.0206(11)
H12B	0.9913(6)	0.3164(6)	0.5653(5)	0.0200(11)
H14A	0.7326(7)	0.4519(6)	0.6241(5)	0.0262(12)
H14B	0.6041(7)	0.4150(7)	0.7326(5)	0.0267(12)
H14C	0.7270(7)	0.3114(7)	0.6135(5)	0.0281(13)
H15A	0.6947(6)	0.2682(6)	0.8746(5)	0.0219(11)
H15B	0.8841(7)	0.1732(7)	0.8435(5)	0.0288(13)
H15C	0.7877(7)	0.1642(6)	0.7554(5)	0.0246(12)
H16A	0.8948(7)	0.3616(6)	1.0017(5)	0.0258(12)
H16B	1.0866(7)	0.2968(6)	0.9432(5)	0.0259(12)
H16C	0.9908(7)	0.2249(6)	0.9150(5)	0.0263(12)
H17A	0.9785(7)	0.5652(6)	0.7808(5)	0.0251(12)
H17B	1.1040(7)	0.4791(6)	0.8498(5)	0.0226(11)
H17C	0.9147(6)	0.5523(6)	0.9298(5)	0.0212(11)
*D1B	0.21944	0.94849	0.86962	0.0312(16)
*D2B	0.06961	0.89024	0.78201	0.0281(14)
*D3B	-0.18719	0.92641	0.8954	0.0271(14)
*D4B	-0.30066	1.01919	1.09411	0.0198(12)
*D5B	-0.15087	1.07791	1.18289	0.0235(13)
*D6B	0.10306	1.04156	1.06927	0.027(3)

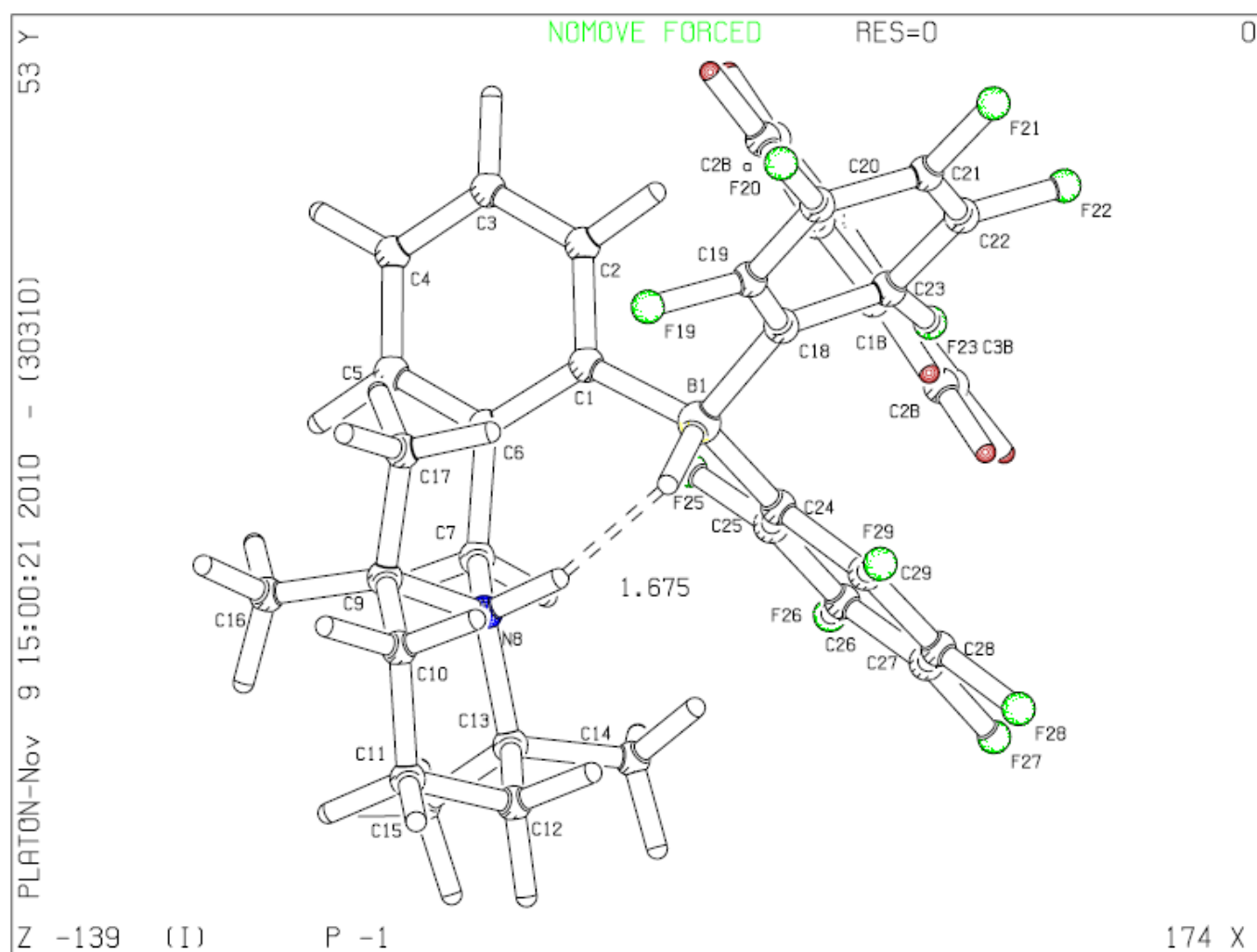


**Figure S52.** ORTEP-plot of the crystal structure of **NHHB** as determined by neutron diffraction.

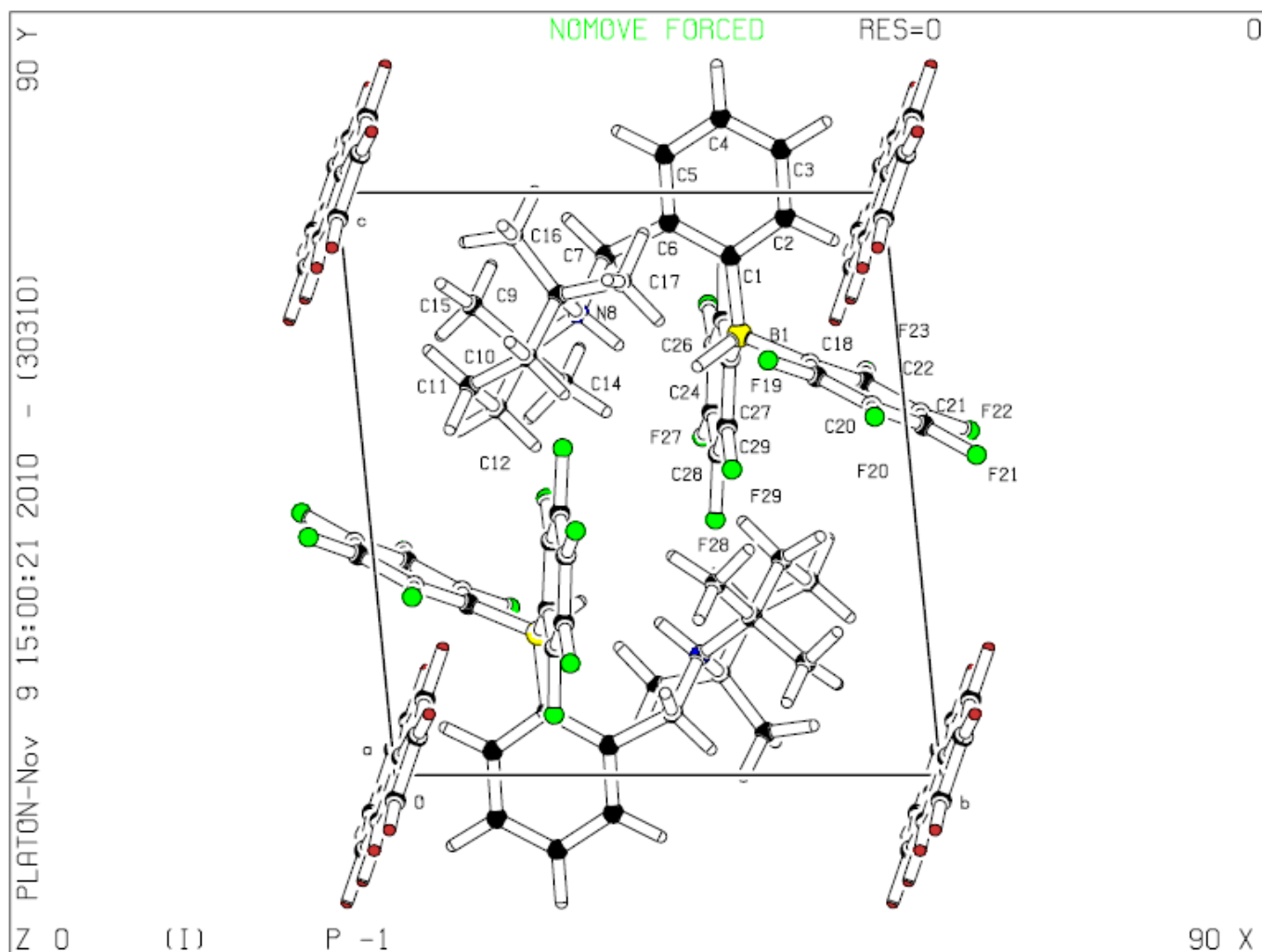


**Figure S53.** ORTEP-plot of the unit cell of the crystal structure of **NHHB** as determined by neutron diffraction.

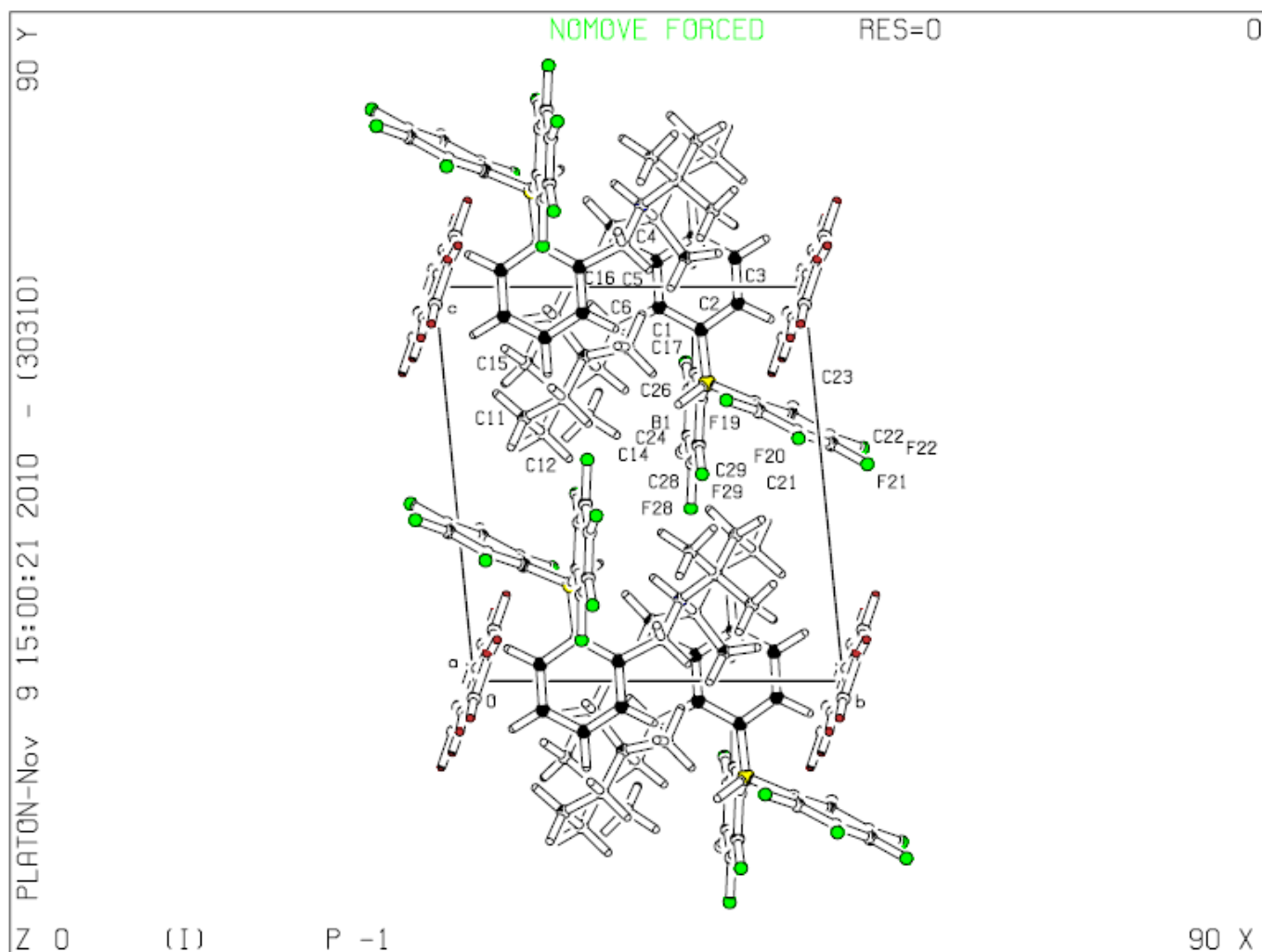


**Figure S54.** ORTEP-plot of the double unit cell of the crystal structure of **NHHB** as determined by neutron diffraction.

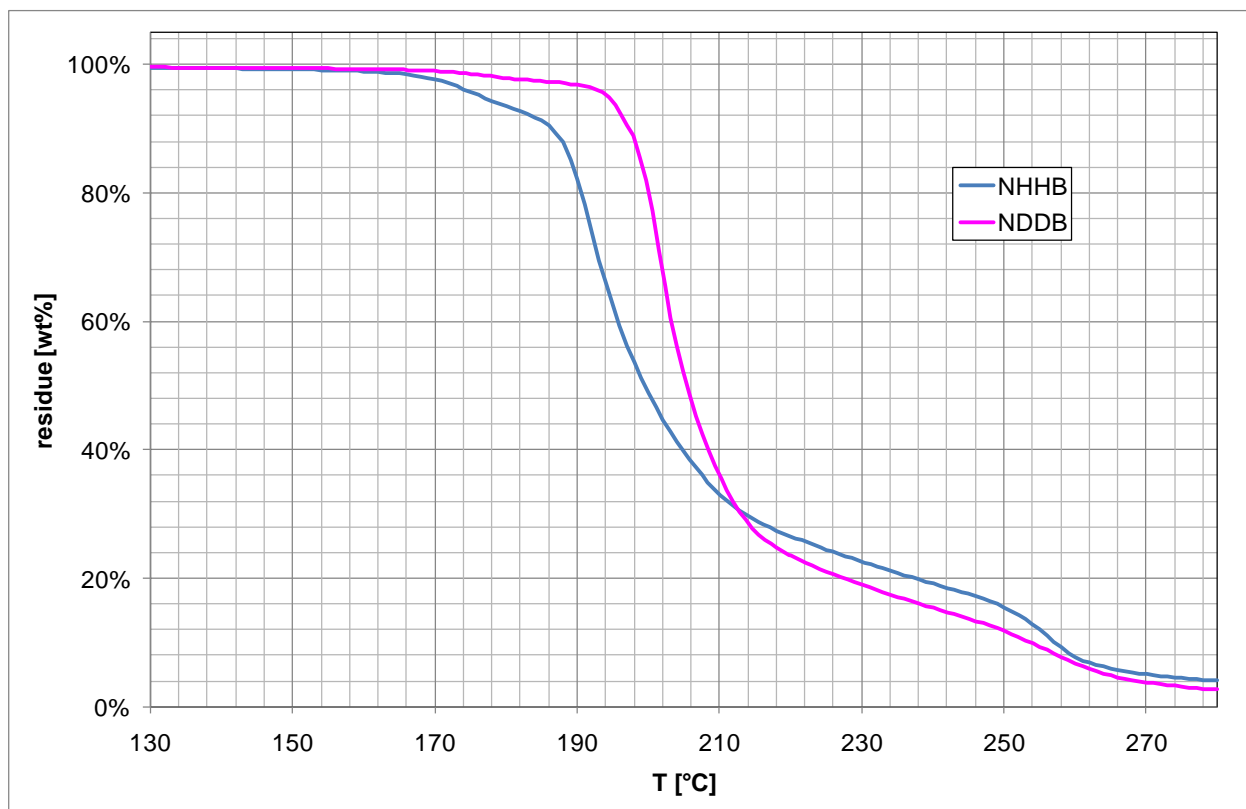


**Figure S55.** TG curves of **NHHB** and **NDDB** at heating rates of 5 °C/min.

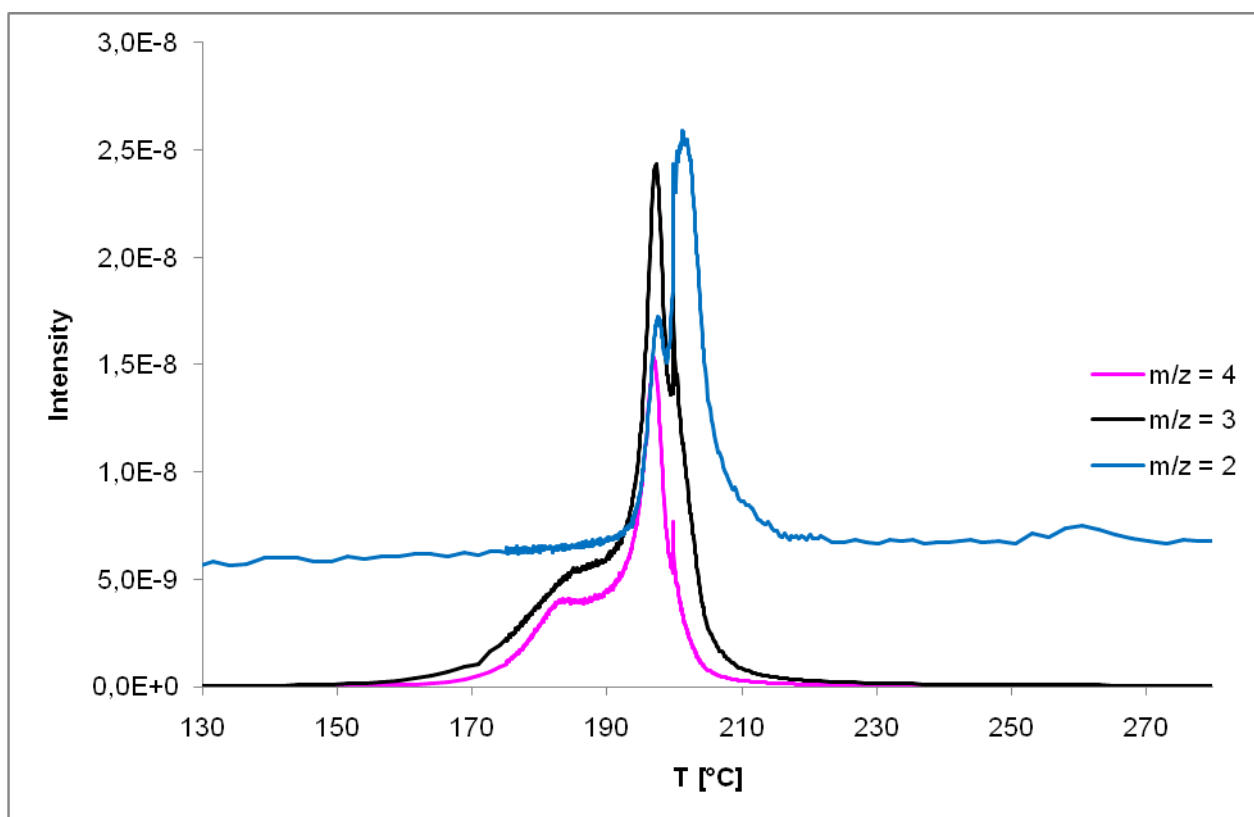


**Figure S56.** Selected MS signals of a TG-MS measurement of **NDDB** at a heating rate of 5 °C/min.

## TG-MS measurements of **NDDB** at isothermal conditions

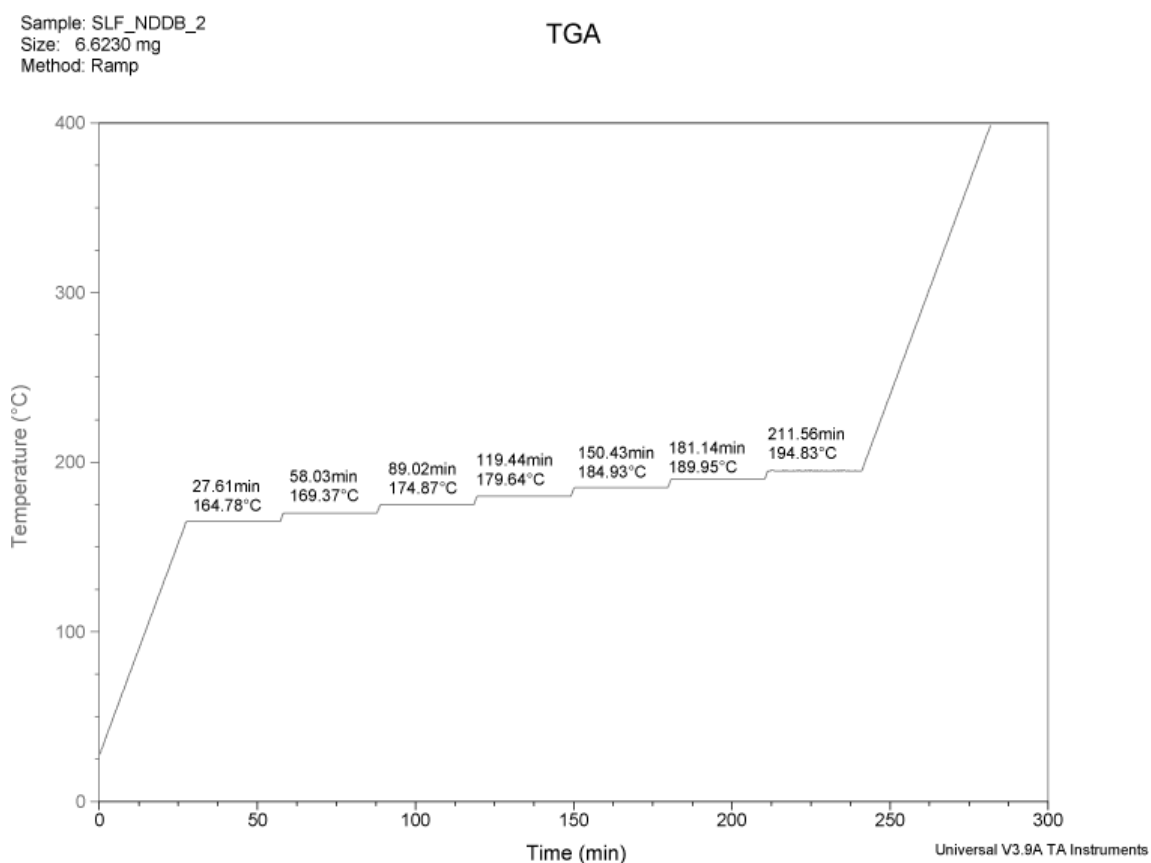


**Figure S57.** Applied measuring sequence for testing of isothermal decomposition of **NDDB** at various temperatures.

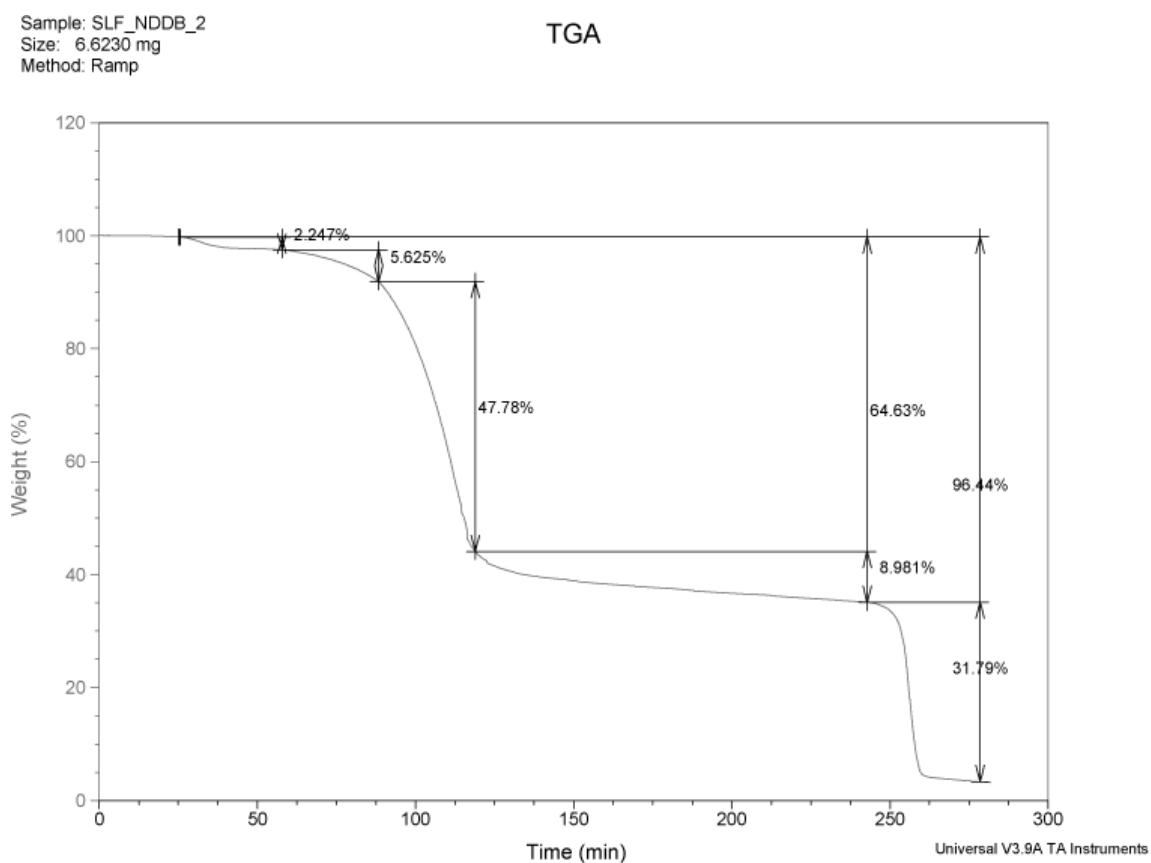


**Figure S58.** TG curves of **NDDB** under isothermal conditions at various temperatures.



User: WACKER-Lehrstuhl TUM

Company: Uni

File: c:\data files\slf\nddb\_2.exp

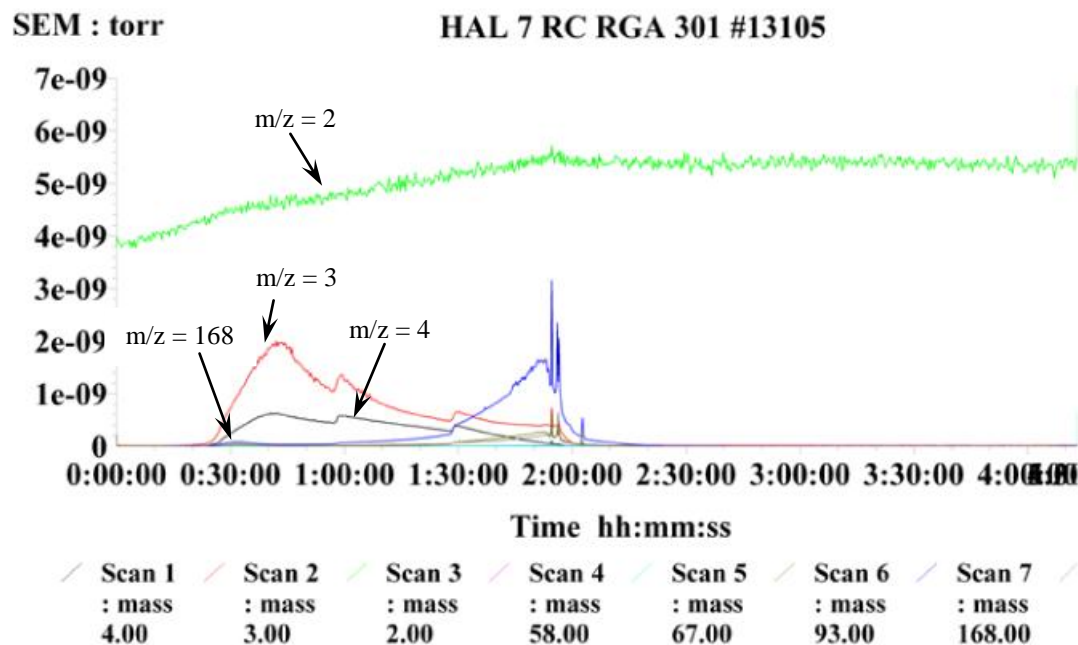


**Figure S59.** Selected MS signals of decomposition products of **NDDB** under isothermal conditions at various temperatures.

Keeping the temperature stable at 165 °C already leads to decomposition of **NDDB**. Even though the largest signals are caused by  $D_2^+$  ( $m/z = 4$  amu) and  $HD^+$  ( $m/z = 3$  amu) which could be interpreted as  $D_2$ -release, traces of  $C_6DF_5^+$  ( $m/z = 169$  amu) are also detected (Figure S59). This clearly indicates decomposition of **NDDB**. In addition the loss in mass at 165 °C sums up to 2.2% of the total mass which is a multiple of the total bound  $D_2$  (0.69%) which gives further evidence for minor decomposition of the molecular tweezers (Figure S58).

Sample: SLF\_NHHB\_2  
Size: 8.4300 mg  
Method: Ramp

## TGA

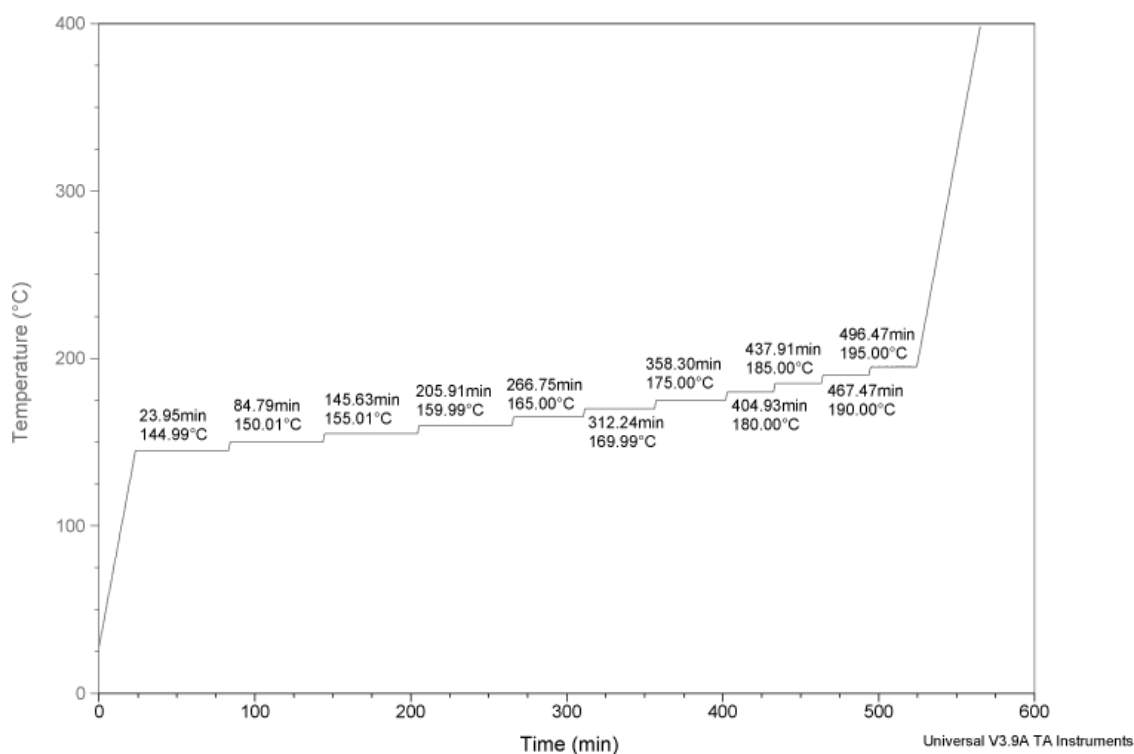


**Figure S60.** Applied measuring sequence for testing of isothermal decomposition of **NHHB** at various temperatures.

Sample: SLF\_NHHB\_2  
Size: 8.4300 mg  
Method: Ramp

## TGA

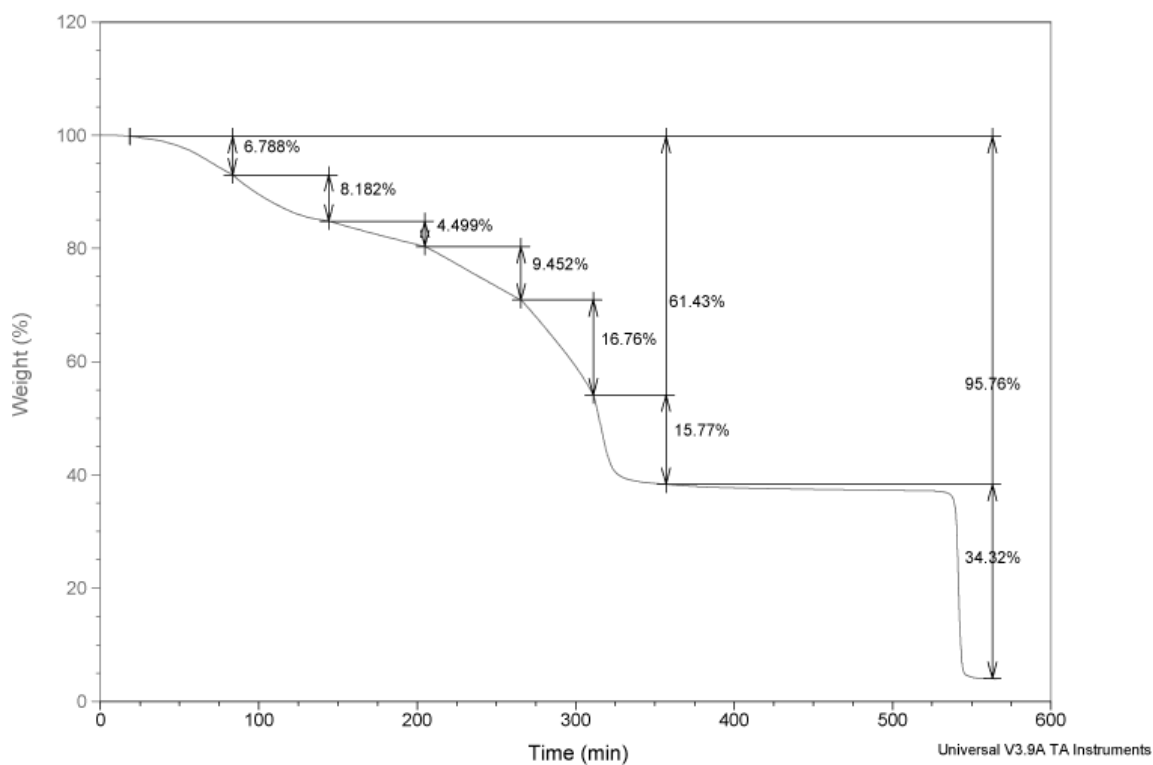


**Figure S61.** TG curves of **NHHB** under isothermal conditions at various temperatures. **NHHB** clearly decomposes already at temperatures as low as 145 °C as indicated by the large loss in weight (6.8%) in comparison with the total split up  $H_2$  (0.35%).

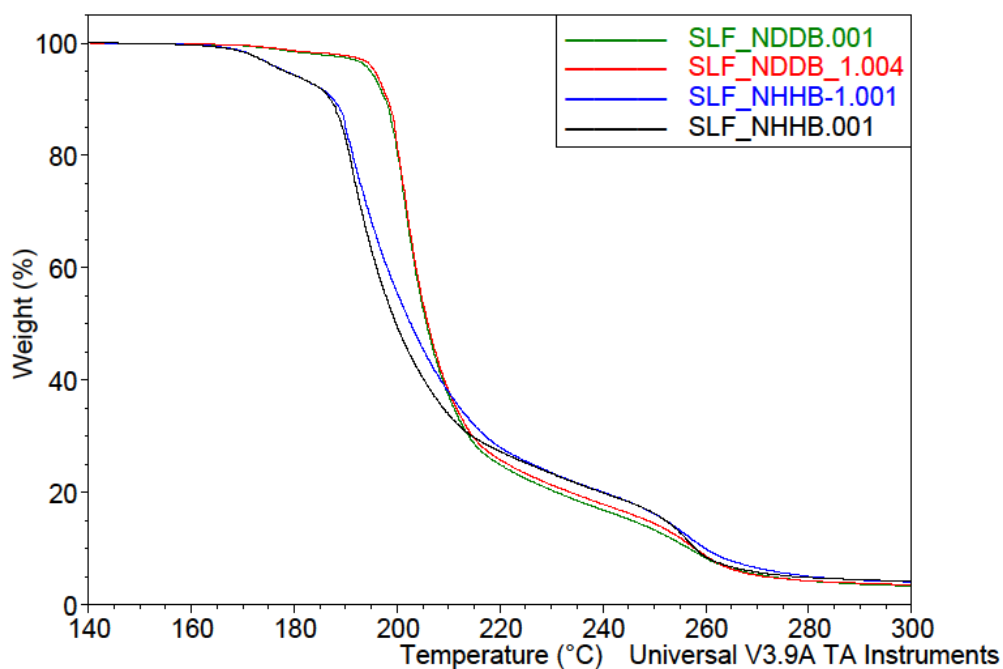


**Figure S62.** TG curves from 140 °C to 300 °C of **NHHB** (black & blue) and **NDDB** (red & green) at heating rates of 5 K/min.

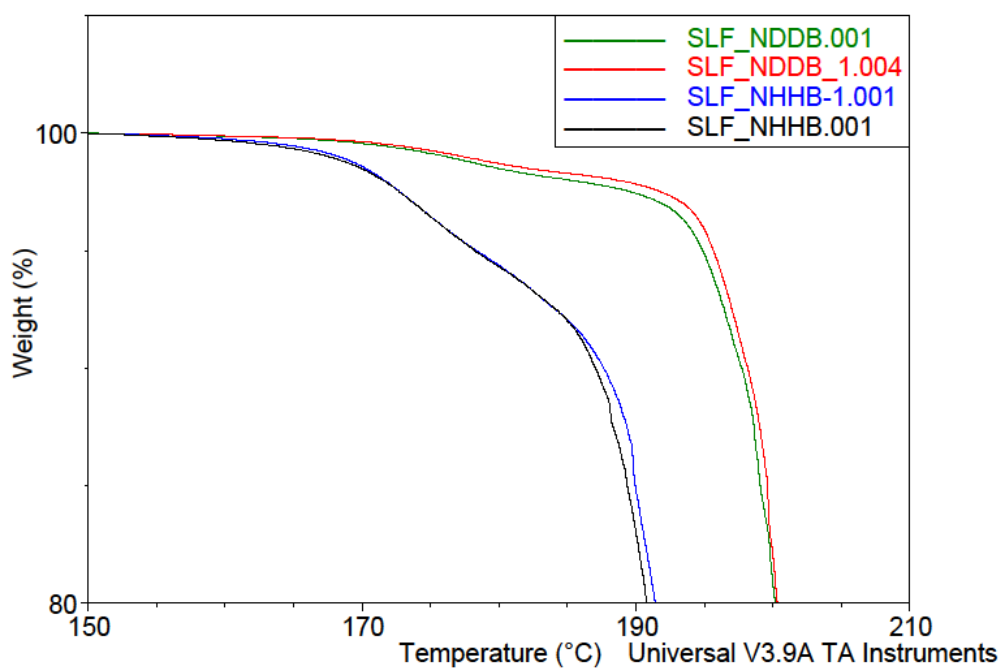


**Figure S63.** Zoom from 150 °C to 210 °C of the TG curves of **NHHB** (pink & green), **NDDB** (red & blue) and the product of the activation of HD by **NB** (black) at heating rates of 5 K/min.

The overlay of the TG curves of different samples of **NHHB** and **NDDB** clearly shows that the different behavior of the two substances is reproducible (Figures S62 & S63).

**Table S5.** Zero-Point Energies (ZPEs) from CAM-B3LYP/6-31G\*\* level calculations based on a harmonic vibration approximation. Atomic units are used.

	ZPE
H <sub>2</sub>	0.0102
D <sub>2</sub>	0.0072
NHHB	0.5062
N-H stretching	0.0075
B-H stretching	0.0058
NDDB	0.4993
N-D stretching	0.0055
B-D stretching	0.0043

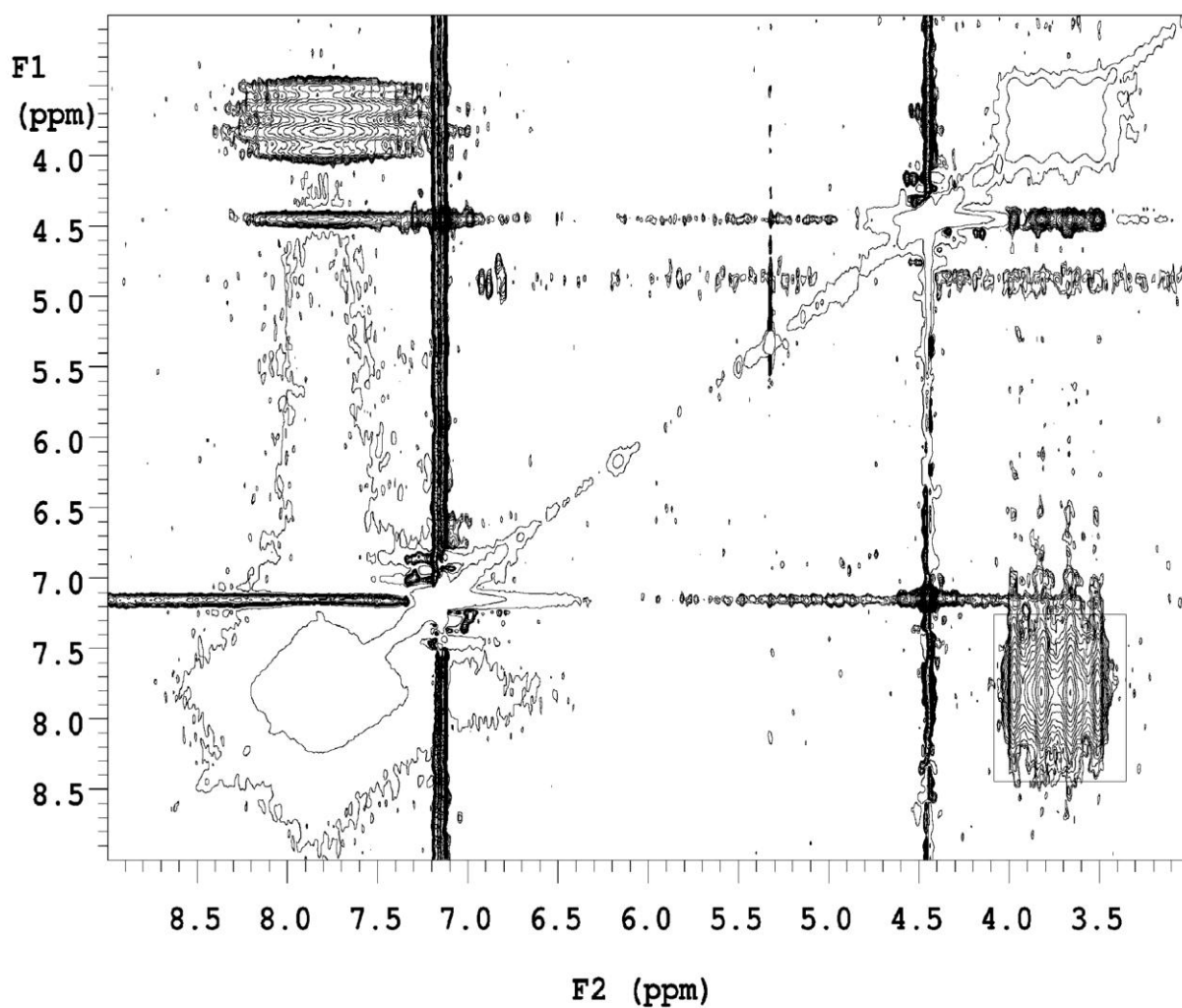


**Figure S64.** Expansion of NOESY spectrum recorded from a  $\text{CD}_2\text{Cl}_2$  sample of **NHHB**. Negative peaks (diagonal) are presented by two sparsely placed contours whereas positive signals are identified by several densely spaced contours. The rectangle centered at 3.75 ppm, 7.75 ppm ( $f_2$ ,  $f_1$ ) shows the limits for 2D integration to determine the *NH-HB* correlation peak volume. NOESY spectra presented in Figures S64-S69 are plotted using the same vertical scaling.

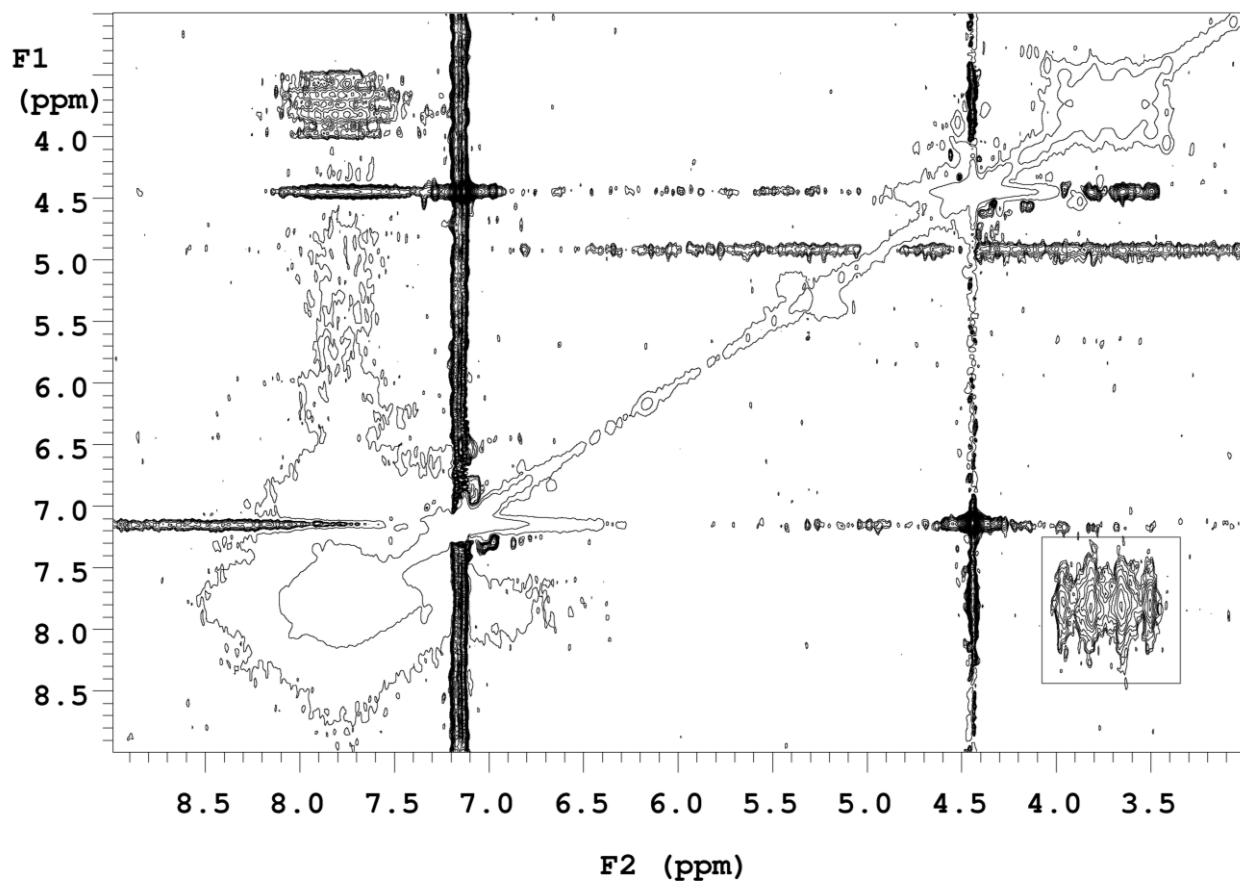


**Figure S65.** Expansion of NOESY spectrum recorded from a  $\text{CD}_2\text{Cl}_2$  sample of an equimolar mixture of **NHDB** and **NDHB**. Negative peaks (diagonal) are presented by two sparsely placed contours whereas positive signals are identified by several densely spaced contours. The rectangle centered at 3.75 ppm, 7.75 ppm ( $f_2$ ,  $f_1$ ) shows the limits for 2D integration to determine the *NH-HB* correlation peak volume. NOESY spectra presented in Figures S64-S69 are plotted using the same vertical scaling.

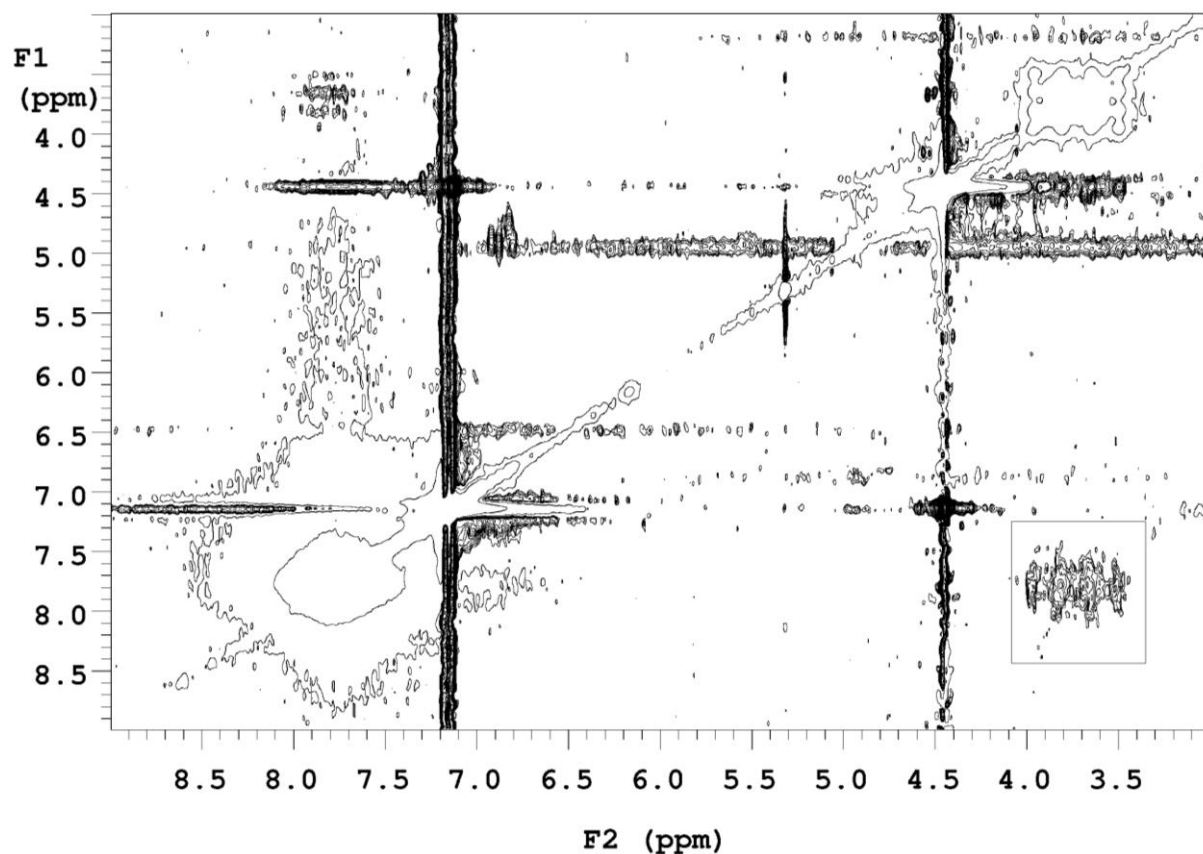


**Figure S66.** Expansion of NOESY spectrum recorded from a  $\text{CD}_2\text{Cl}_2$  sample of **NB** reacted with HD. Negative peaks (diagonal) are presented by two sparsely placed contours whereas positive signals are identified by several densely spaced contours. The rectangle centered at 3.75 ppm, 7.75 ppm ( $f_2$ ,  $f_1$ ) shows the limits for 2D integration to determine the *NH-HB* correlation peak volume. NOESY spectra presented in Figures S64-S69 are plotted using the same vertical scaling.

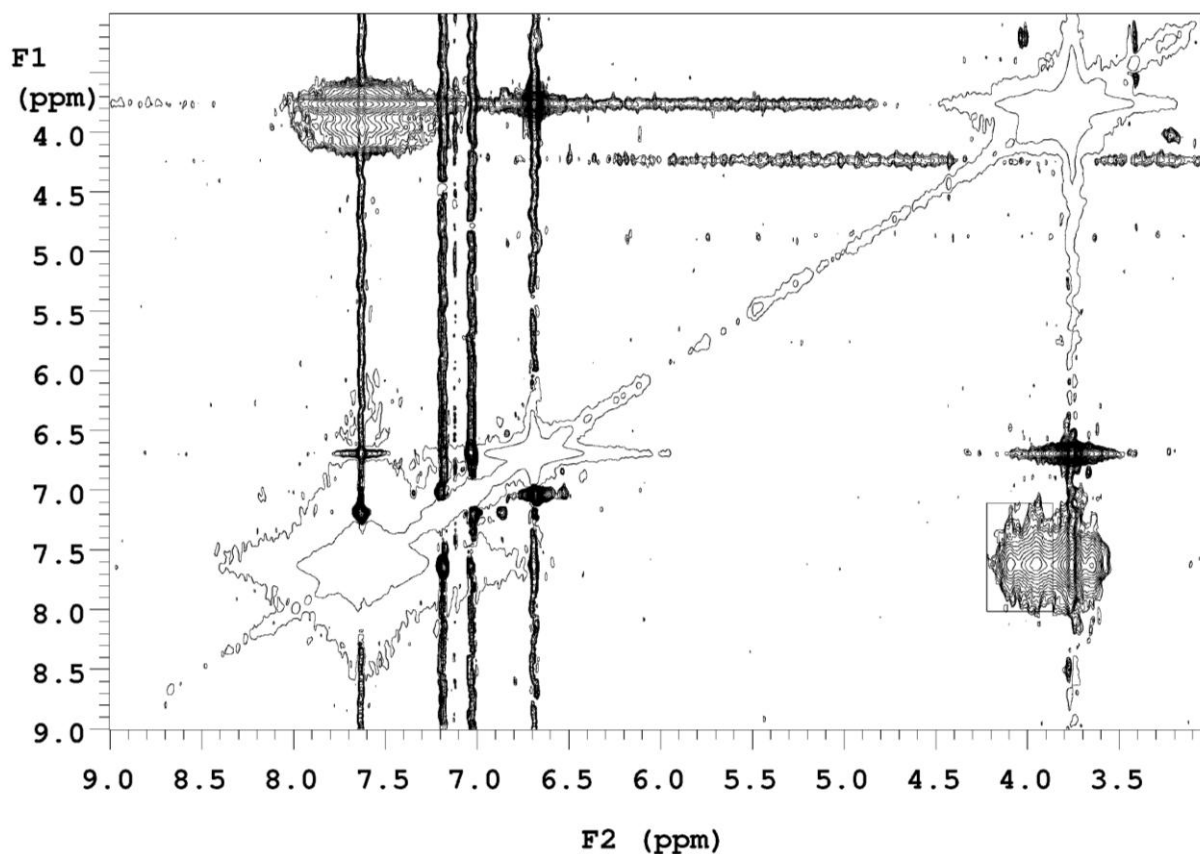


**Figure S67.** Expansion of NOESY spectrum recorded from a  $C_6D_6$  sample of **NHHB**. Negative peaks (diagonal) are presented by two sparsely placed contours whereas positive signals are identified by several densely spaced contours. The rectangle centered at 4.00 ppm, 7.70 ppm ( $f_2$ ,  $f_1$ ) shows the limits for 2D integration to determine the *NH-HB* correlation peak volume. Effectively, only half of the cross peak volume is captured and the data has to be multiplied by 2 to estimate the actual *NH-HB* NOESY cross peak volume. NOESY spectra presented in Figures S64-S69 are plotted using the same vertical scaling.



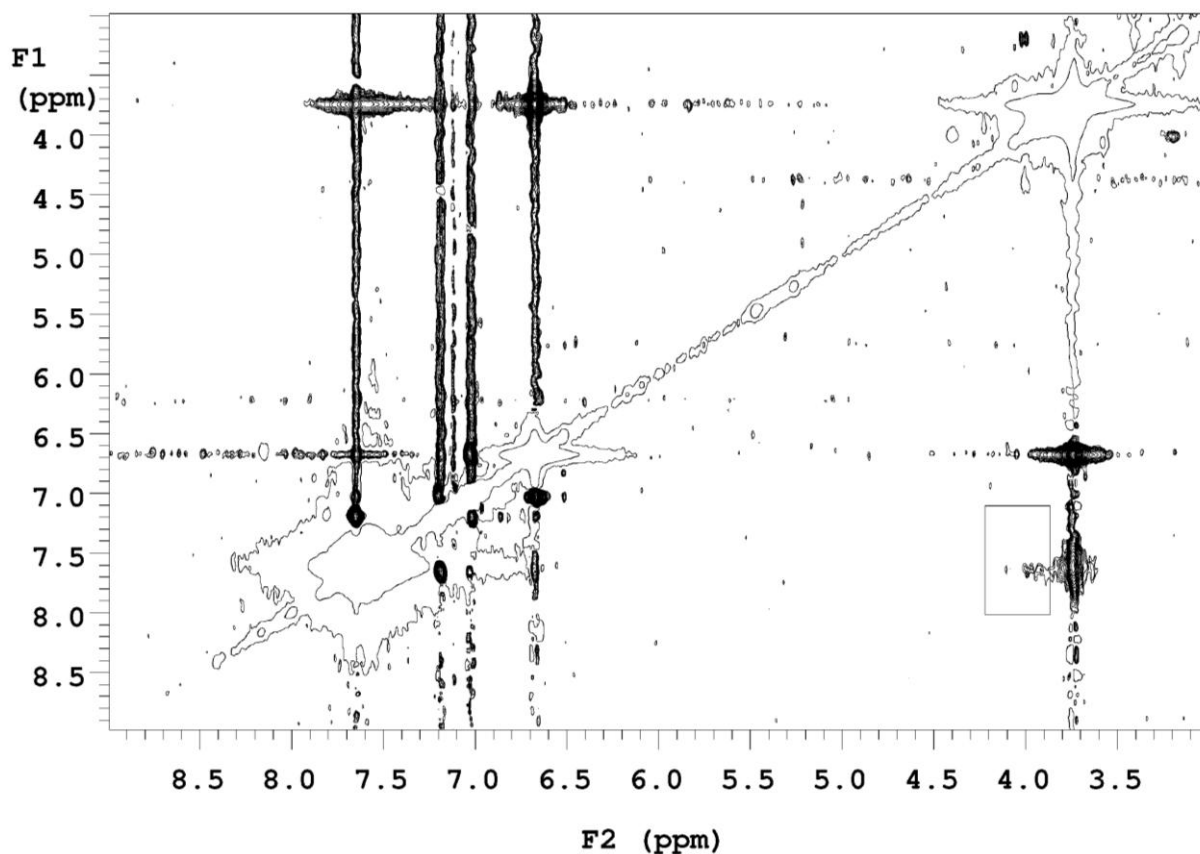


**Figure S68.** Expansion of NOESY spectrum recorded from a C<sub>6</sub>D<sub>6</sub> sample of an equimolar mixture of **NHDB** and **NDHB**. Negative peaks (diagonal) are presented by two sparsely placed contours whereas positive signals are identified by several densely spaced contours. The rectangle centered at 4.00 ppm, 7.70 ppm ( $f_2$ ,  $f_1$ ) shows the limits for 2D integration to determine the *NH-HB* correlation peak volume. Effectively, only half of the cross peak volume is captured and the data has to be multiplied by 2 to estimate the actual *NH-HB* NOESY cross peak volume. NOESY spectra presented in Figures S64-S69 are plotted using the same vertical scaling.

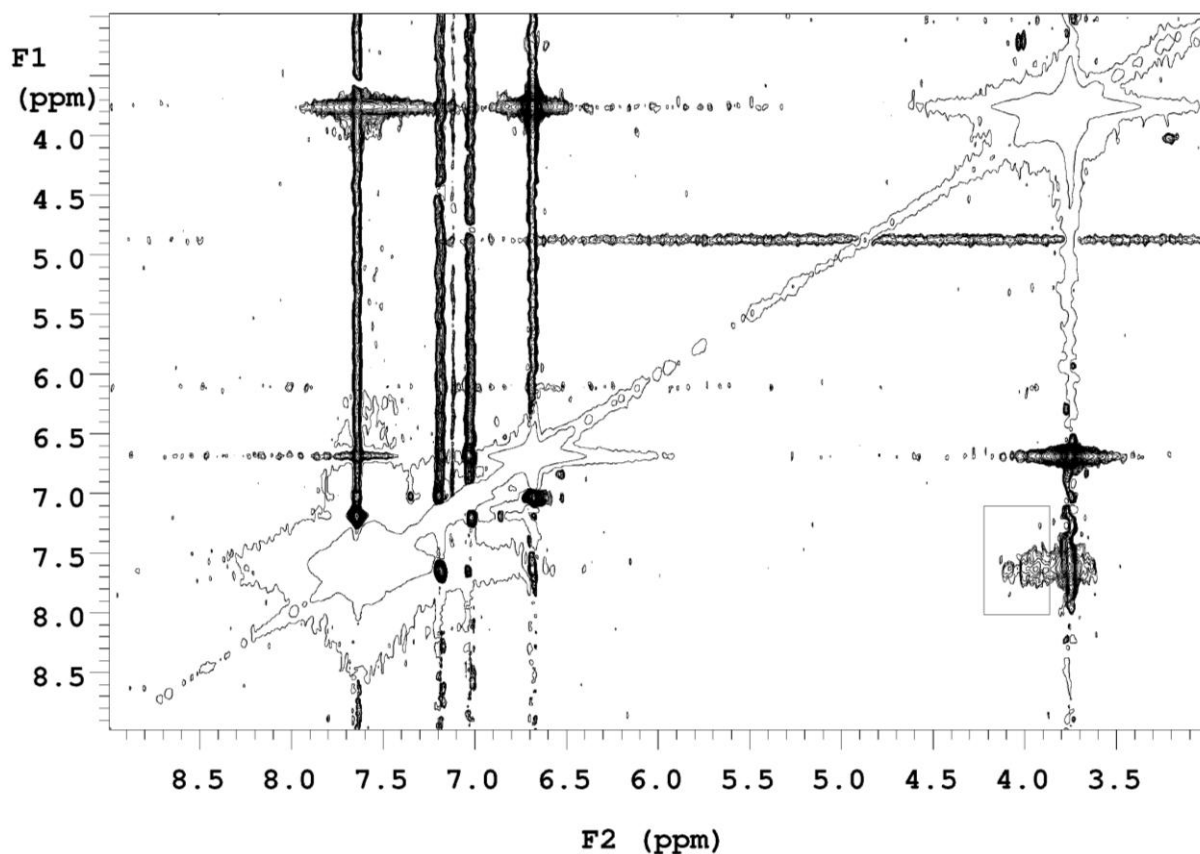


**Figure S69.** Expansion of NOESY spectrum recorded from a  $C_6D_6$  sample of **NB** reacted with HD. Negative peaks (diagonal) are presented by two sparsely placed contours whereas positive signals are identified by several densely spaced contours. The rectangle centered at 4.00 ppm, 7.70 ppm ( $f_2$ ,  $f_1$ ) shows the limits for 2D integration to determine the *NH-HB* correlation peak volume. Effectively, only half of the cross peak volume is captured and the data has to be multiplied by 2 to estimate the actual *NH-HB* NOESY cross peak volume. NOESY spectra presented in Figures S64-S69 are plotted using the same vertical scaling.

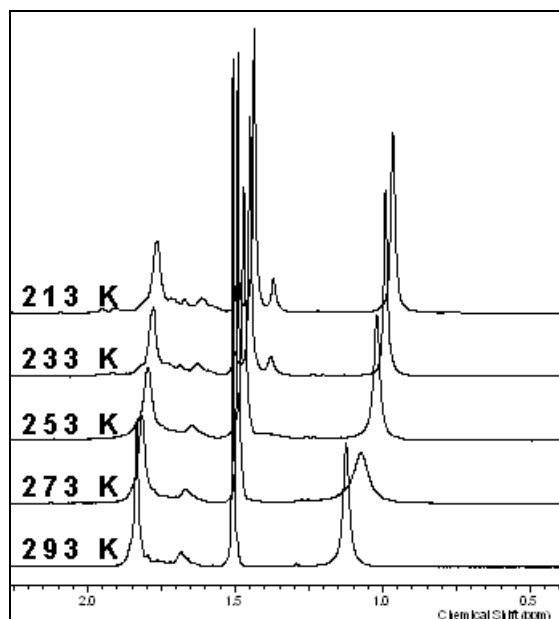


**Figure S70.** Low temperature  $^1\text{H}$ -NMR spectra of **NHHB** dissolved in  $\text{CH}_2\text{Cl}_2$ . Displayed is the zoomed region of the aliphatic protons of the TMP. Upon lowering the temperature the appearance of new signals which correspond to the piperidine ring is observed (2.0 ppm to 1.3 ppm).

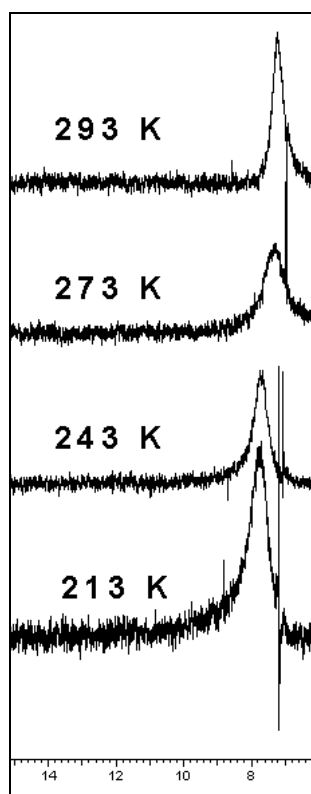


**Figure S71.** Low temperature  $^2\text{H}$ -NMR spectra of a  $\text{CH}_2\text{Cl}_2$  solution of the combined products of the splittage of HD by **NB**. Displayed is the zoomed region of the ND peak in the spectra. Upon lowering the temperature a clear downfield shift of the ND signal from 7.23 ppm at 293 K to 7.74 ppm at 213 K is observed.

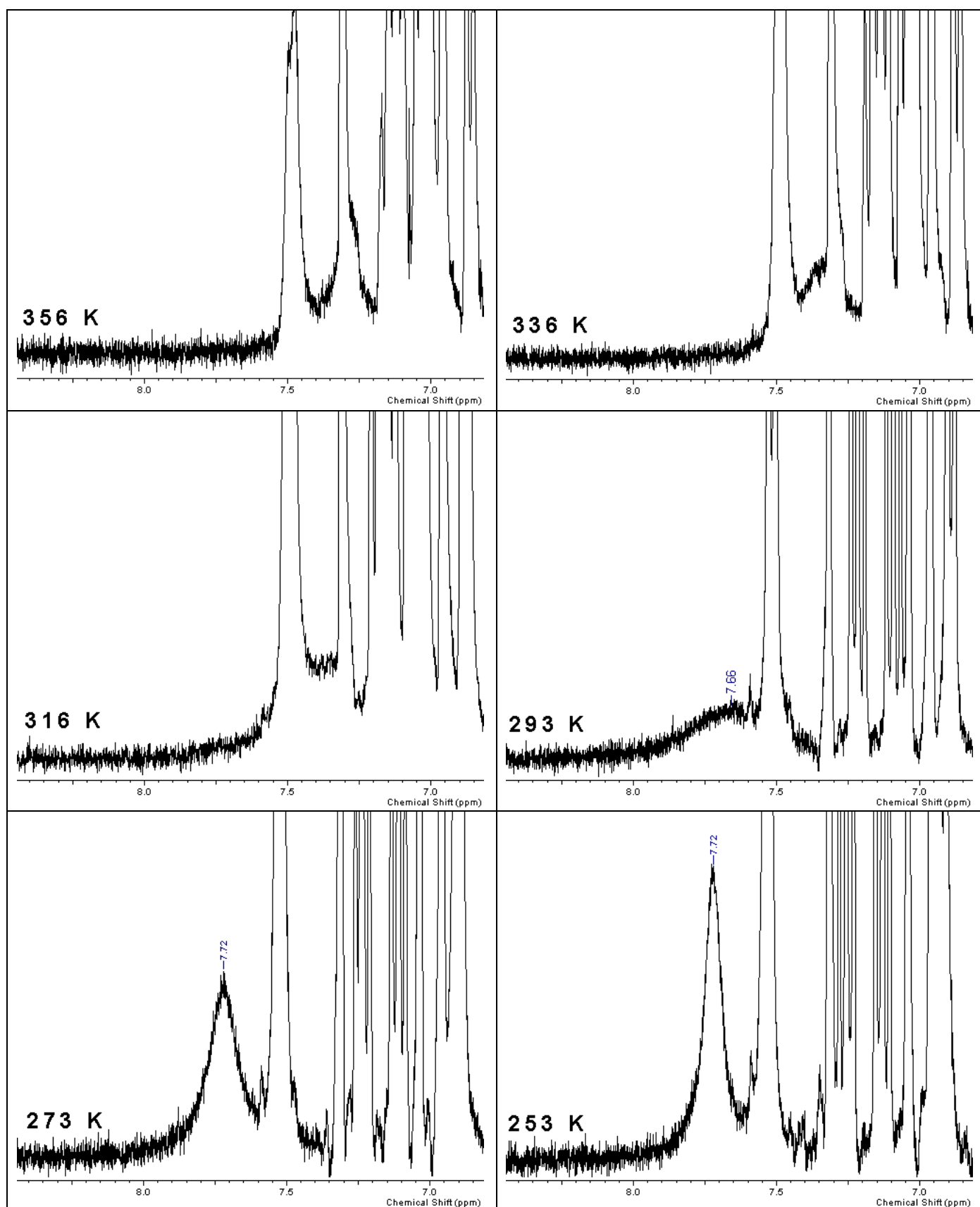


**Figure S72.** VT  $^1\text{H}$ -NMR spectra of **NHHB** dissolved in  $\text{C}_6\text{D}_5\text{Br}$ . Displayed is the zoomed region of the *NH* peak in the spectra. Upon lowering the temperature a clear downfield shift of the *NH* signal from 7.27 ppm at 356 K to 7.72 ppm at 253 K is observed. The sample starts to decompose at 356 K ( $\text{H}_2$  evolution and simultaneous **NB** formation).

## Complete reference 71

Frisch, M. J.; Trucks, G. W.; Schlegel, H. B.; Scuseria, G. E.; Robb, M. A.; Cheeseman, J. R.; Scalmani, G.; Barone, V.; Mennucci, B.; Petersson, G. A.; Nakatsuji, H.; Caricato, M.; Li, X.; Hratchian, H. P.; Izmaylov, A. F.; Bloino, J.; Zheng, G.; Sonnenberg, J. L.; Hada, M.; Ehara, M.; Toyota, K.; Fukuda, R.; Hasegawa, J.; Ishida, M.; Nakajima, T.; Honda, Y.; Kitao, O.; Nakai, H.; Vreven, T.; Montgomery, Jr., J. A.; Peralta, J. E.; Ogliaro, F.; Bearpark, M.; Heyd, J. J.; Brothers, E.; Kudin, K. N.; Staroverov, V. N.; Kobayashi, R.; Normand, J.; Raghavachari, K.; Rendell, A.; Burant, J. C.; Iyengar, S. S.; Tomasi, J.; Cossi, M.; Rega, N.; Millam, N. J.; Klene, M.; Knox, J. E.; Cross, J. B.; Bakken, V.; Adamo, C.; Jaramillo, J.; Gomperts, R.; Stratmann, R. E.; Yazyev, O.; Austin, A. J.; Cammi, R.; Pomelli, C.; Ochterski, J. W.; Martin, R. L.; Morokuma, K.; Zakrzewski, V. G.; Voth, G. A.; Salvador, P.; Dannenberg, J. J.; Dapprich, S.; Daniels, A. D.; Farkas, Ö.; Foresman, J. B.; Ortiz, J. V.; Cioslowski, J.; Fox, D. J. *Gaussian 09, Rev. A.01*, Gaussian Inc., Wallingford, CT, 2009.

## References

- (1) (a) Günther, H. *NMR Spectroscopy*, 2nd ed.; John Wiley & Sons: New York, 2001. (b) Friebolin, H. *Basic One- and Two-Dimensional NMR Spectroscopy*, 3rd ed.; Wiley-VCH: Weinheim, 1998.
- (2) Kintzinger, J. P.; Lehn, M. *Mol. Phys.* **1968**, *14*, 133-145.
- (3) ) Shepperd, C. M.; Schaefer, T.; Goodwin, B. W.; t'Raa, J. *Can. J. Chem.* **1971**, *49*, 3158-3164.
- (4) The small signal in between the NH peak and the peaks of the aromatic protons can be ascribed to  $^{13}\text{C}$  satellites of the aromatic signals (7.47 – 7.37 and 6.95 – 6.85 ppm).
- (5) Rokob, T. A.; Hamza, A.; Pápai, I. *J. Am. Chem. Soc.* **2009**, *131*, 10701-10710.
- (6) Bakhmutov, V. I. *Practical NMR Relaxation for Chemists*; John Wiley & Sons: Chichester, 2004.
- (7) Desrosiers, P. J.; Cai, L. H.; Lin, Z. R.; Richards, R.; Halpern, J. *J. Am. Chem. Soc.* **1991**, *113*, 4173-4184.
- (8) Stott, K.; Stonehouse, J.; Keeler, J.; Hwang, T.-L.; Shaka, A. J. *J. Am. Chem. Soc.* **1995**, *117*, 4199-4200.
- (9) Montelione, G. T.; Rios, C. B.; Swapna, G. V. T.; Zimmerman, D. E. NMR Pulse Sequences and Computational Approaches for Automated Analysis of Sequence-Specific Backbone Resonance Assignments of Proteins. In *Biological Magnetic Resonance 17. Structure Computation and Dynamics in Protein NMR*; Krishna, N. R.; Berliner, L. J., Eds.; Kluwer Academic / Plenum Publishers: New York, 1999.
- (10) (a) Fletcher, C. M.; Jones, D. N. M.; Diamond, R.; Neuhaus, D. *J. Biomol. NMR* **1996**, *8*, 292-310. (b) Cronin, L.; Higgitt, C. L.; Perutz, R. N. *Organometallics* **2000**, *19*, 672-683. (c) Zagrovic, B.; van Gunsteren, W. F. *Proteins: Structure, Function, and Bioinformatics* **2006**, *63*, 210-218.
- (11) (a) Ping F, Y. *J. Magn. Reson.* **1990**, *90*, 382-383. (b) Jones, C. R.; Butts, C. P.; Harvey, J. N. *Beilstein J. Org. Chem.* **2011**, *7*, 145-150.
- (12) (a) Stott, K.; Keeler, J.; Van, Q. N.; Shaka, A. J. *J. Magn. Reson.* **1997**, *125*, 302-324. (b) Hu, H.; Krishnamurthy, K. *J. Magn. Reson.* **2006**, *182*, 173-177.